

2013

## **Cumulative Single-cell Laser Ablation of Functionally or Genetically Defined Respiratory Neurons Interrogates Network Properties of Mammalian Breathing-related Neural Circuits in vitro**

Xueying Wang  
*College of William & Mary - Arts & Sciences*

Follow this and additional works at: <https://scholarworks.wm.edu/etd>

 Part of the [Neurosciences Commons](#)

---

### **Recommended Citation**

Wang, Xueying, "Cumulative Single-cell Laser Ablation of Functionally or Genetically Defined Respiratory Neurons Interrogates Network Properties of Mammalian Breathing-related Neural Circuits in vitro" (2013). *Dissertations, Theses, and Masters Projects*. Paper 1539623609.  
<https://dx.doi.org/doi:10.21220/s2-s4nt-1m46>

This Dissertation is brought to you for free and open access by the Theses, Dissertations, & Master Projects at W&M ScholarWorks. It has been accepted for inclusion in Dissertations, Theses, and Masters Projects by an authorized administrator of W&M ScholarWorks. For more information, please contact [scholarworks@wm.edu](mailto:scholarworks@wm.edu).

Cumulative Single-cell Laser Ablation of Functionally or Genetically Defined  
Respiratory Neurons Interrogates Network Properties of Mammalian  
Breathing-related Neural Circuits in vitro

Xueying Wang

Xi'an, Shaanxi, China

M.A. The College of William and Mary, 2010  
B.A. Huazhong University of Science & Technology, 2008

A Dissertation presented to the Graduate Faculty  
of the College of William and Mary in Candidacy for the Degree of  
Doctor of Philosophy

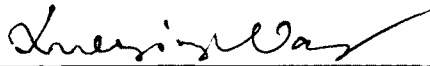
Department of Applied Science

The College of William and Mary  
January, 2013

## APPROVAL PAGE

This Dissertation is submitted in partial fulfillment of  
the requirements for the degree of

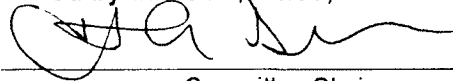
Doctor of Philosophy



---

Xueying Wang

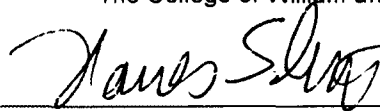
Approved by the Committee, November, 2012



---

Committee Chair

Associate Professor and Chair Christopher A. Del Negro, Applied Science  
The College of William and Mary



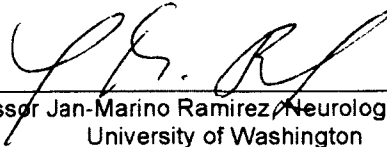
---

Assistant Professor Hannes C. Schniepp, Applied Science  
The College of William and Mary



---

Assistant Professor Michael Drew LaMar, Biology  
The College of William and Mary



---

Professor Jan-Marino Ramirez, Neurological Surgery  
University of Washington

## COMPLIANCE PAGE

Research approved by

Institutional Animal Care and Use Committee

Protocol number(s): IACUC-2007-07-26-6795-cadeln

IACUC-2010-07-12-6795-cadeln

Date(s) of approval: July 26, 2008

July 26, 2009

July 30, 2010

July 30, 2011

July 30, 2012

## ABSTRACT

A key feature of many neurodegenerative diseases is the pathological loss of neurons that participate in generating behavior. To mimic the neuronal degeneration procedure of a functioning neural circuit, we designed a computer-automated system that algorithmically detects and sequentially laser-ablates constituent neurons from a neural network with single-cell precision while monitoring the progressive change of the network function in real time. We applied this cell-specific cumulative lesion technique to an advantageous experimental model, the preBötzinger Complex (preBötC), the mammalian respiratory central pattern generator (CPG) that can be retained in thin slice preparations and spontaneously generates breathing-related motor activity *in vitro*. As a consequence, we sought to investigate the issue: how many neurons are necessary for generating respiratory behavior *in vitro*? This question pertains to whether and how progressive cell destruction will impair, and possibly preclude, behaviorally relevant network function. Our ablation system identifies rhythm-generating interneurons in the preBötC based on genetically encoded fluorescent protein markers or imaged  $Ca^{2+}$  activity patterns, stores their physical locations in memory, and then randomly laser-ablates the neuron targets one at a time in sequence, while continuously measuring changes to respiratory motor output via hypoglossal (XII) nerve electrophysiologically *in vitro*. A critical feature of the system is custom software package dubbed Ablator (in Python code) that detects cell targets, controls stage translation, focuses the laser, and implements the spot-lesion protocol automatically. Experiments are typically carried out in three steps: 1) define the domain of lesion and initialize the system, 2) perform image acquisition and target detection algorithms and maps populations of respiratory neurons in the bilateral volumes of the slice, 3) determine the order of lesions and then spot-lesion target neurons sequentially until all the targets are exhausted. Here we show that selectively and cumulatively deleting rhythmically active inspiratory neurons that are detected via  $Ca^{2+}$  imaging in the preBötC, progressively decreases respiratory frequency and the amplitude of motor output. On average, the deletion of  $120 \pm 45$  neurons stopped spontaneous respiratory rhythm, and our data suggest ~82% of the rhythm generating neurons remain un-lesioned. Similarly, destruction of  $85 \pm 45$  homeodomain transcription factor *Dbx1*-derived (*Dbx1*<sup>+</sup>) neurons, which were hypothesized to comprise the rhythmogenic core of the respiratory CPG in the preBötC, precludes the respiratory motor behavior *in vitro* as well. The fact that these two estimates of the size of the critical rhythmogenic core in the preBötC are different can be reconciled considering that the  $Ca^{2+}$  imaging method identifies ~50% inhibitory neurons, which are found in the preBötC but are not rhythmogenic. *Dbx1*<sup>+</sup>, on the other hand, identifies only excitatory rhythmogenic neurons. Serial ablations in other medullary respiratory regions did not affect frequency, but diminished the amplitude of motor output to a lesser degree. These data support the hypothesis that cumulative single-cell ablations caused a critical threshold to be crossed during lesioning, after which rhythm generation in the respiratory network was unsustainable. Furthermore, this study provides a novel measurement that can help quantify network properties of the preBötC and gauge its susceptibility to failure. Our results in turn may help explain respiratory failure in patients with neurodegenerative diseases that cause progressive cell death in the brainstem respiratory networks.

# TABLE OF CONTENTS

Acknowledgements	ii
Dedications	iii
List of Tables	iv
List of Figures	v
Introduction	1
CHAPTER 1. Automated cell-specific laser detection and ablation system <i>in vitro</i>	
1.1. Introduction	19
1.2. Methods	20
1.3. Results	43
1.4. Discussion	46
1.5. References	51
CHAPTER 2. Cumulative lesioning of functionally identified respiratory interneurons disrupts and precludes motor rhythms <i>in vitro</i>	
2.1. Introduction	55
2.2. Methods	56
2.3. Results	60
2.4. Discussion	71
2.5. References	76
CHAPTER 3. Cumulative lesioning of genetically identified respiratory interneurons disrupts and precludes motor rhythms <i>in vitro</i>	
3.1. Introduction	81
3.2. Methods	82
3.3. Results	85
3.4. Discussion	92
3.5. References	97
Conclusions	100
Appendix	104

## ACKNOWLEDGEMENTS

I sincerely thank my advisor, Christopher Del Negro, for his tireless and endless training, guidance, support and encouragement throughout this project. As my first advisor in neuroscience, Christopher led me into this exciting field and trained me to be a serious neuroscientist with great enthusiasm in answering fundamental questions in basic sciences. He has showed me how diligence and perseverance can prove to accomplish any task. I could not have become the person I am today without his tremendous influence on me during the past four years in graduate school. I am grateful for having him in my life, and I hope that my future life's work serves as testament to the considerable time and effort he has put into training me.

I sincerely thank John Hayes, who taught me in every detail of how to run an experiment in the lab, including tons of keyboard shortcuts when I started using my first mac. As my second mentor in graduate school, John showed me how to think creatively and these four years would have been impossible without his support and help. Words cannot begin to describe my appreciation and gratitude for all he has done for me. I am incredibly proud of having him in my life, and I thank him from the bottom of my heart.

I thank my fellow lab member Tina Picardo, for her support as she helped me not only through work, but also through life. We went through those difficult times together, we supported each other no matter what. I cannot tell how appreciative I am of how wonderful, amazing and supportive she has been through graduate school years. "You can do it, Snow." Her words will always sing in my ears today and many years later.

I thank my parents for always believing in me and encouraging me to do my best. They have always inspired and supported me in every decision I have made. Without them, I would have never made it this far. I thank my parents with love forever and always.

I thank Chang Lu, who has been with me through it all, from the chaos and the most distressing times of my life, to now, the happy graduation. I have definitely had my ups and downs, but I have come a far way with her constant and unwavering support and love. I will always remember the songs she sang to me, I will always try my best to not let her down, and I will always keep my promise to her: Be who I am and make difference to the world.

Finally, I sincerely thank my committee members, Dr. Ramirez, Dr. Schniepp, and Dr. LaMar for their warm encouragement and valuable advice on this dissertation work.

This dissertation is dedicated to my beloved parents and dearest maomao.



## LIST OF TABLES

2.1	Number of inspiratory neurons detected per 10- $\mu$ m plane per side in n=5 preBötC-surface slices.	63
2.2	Number of inspiratory neurons detected per 10- $\mu$ m plane per side in n=8 VRC-surface slices.	63

## LIST OF FIGURES

1.1	Schematic diagram of the integrated instrument.	25
1.2	Schematic diagram of the basic three-phase protocol.	26
1.3	Custom circuit to control the motorized xy translation stage.	27
1.4	Planar images pertaining to a Ca <sup>2+</sup> acquisition stack.	32
1.5	Detecting cell targets via fluorescent reporters.	34
1.6	The priority rule in target cell detection.	36
1.7	Detecting cell targets via Ca <sup>2+</sup> imaging.	37
1.8	Whole-cell recording from the preBötC neuron that was first identified as ROI 106 in <b>Figure 1.7</b> (see panels <b>A<sub>1</sub></b> , <b>B<sub>3</sub></b> , <b>C<sub>3</sub></b> , <b>D<sub>3</sub></b> ).	39
1.9	Laser ablation and confirmation.	41
1.10	Automated cell target detection and ablation in the preBötC.	44
2.1	Anatomy of slices that retain the preBötC.	57
2.2	Inspiratory neurons in the preBötC.	61
2.3	Average number of inspiratory neurons detected at each acquisition depth in both VRC-surface slices and preBötC-surface slices.	63
2.4	Cumulative deletion of inspiratory neurons.	66
2.5	Ablation effects on respiratory rhythm and XII amplitude.	67
2.6	SP injections in preBötC-surface slices.	69
3.1	Dbx1 <sup>+</sup> neurons in the preBötC.	84
3.2	Cumulative deletion of Dbx1 <sup>+</sup> neurons.	87
3.3	Ablation effects on respiratory rhythm and XII amplitude.	88
3.4	SP injections in preBötC-surface slices.	90
A.1	Screenshot of the GUI launched by XYTranslator_Control.py routine.	105

# INTRODUCTION

## ***Background and Significance***

**INSPIRATION IS THE CORE OF BREATHING.** Breathing behavior in mammals is due to the pumping movements of the diaphragm and external intercostal muscles that drive inspiratory airflow alternating with passive expiration resulting from the contraction of the abdominal and internal intercostal muscles. Muscles related to respiration are controlled by cranial and upper spinal motor nerves that receive motor commands from respiratory networks in the medulla oblongata. The pattern of motor commands during breathing consist of inspiratory and expiratory phases, which are generated periodically to produce ventilation. At rest, and under most physiological conditions, expiration is mainly passive in mammals (Janczewski & Feldman 2006; Richter 1982), thus breathing is dominated by inspiratory efforts. It is advantageous to study the respiratory behavior from an experimental perspective because reduced preparations from the neonatal rodent brain stem are able to preserve the essential rhythm-generating neural circuits *in vitro* (Smith & Feldman 1987; Smith et al. 1990; Smith et al. 1991; Suzue 1984).

**THE PREBÖTZINGER COMPLEX CONTAINS THE INSPIRATORY RHYTHMOGENIC KERNEL.** Neural networks in the brainstem and spinal cord spontaneously generate rhythm and pattern for breathing (Bianchi et al. 1995; Feldman & McCrimmon 2002; Feldman et al. 1986; Feldman et al. 2003; Onimaru et al. 1997; Rekling & Feldman 1998; Richter & Spyer 2001). These networks include neurons of the dorsal respiratory group (DRG) that participate in afferent feedback and autonomic regulation, and neurons of a contiguous ventrolateral respiratory column (VRC),

which is bilaterally distributed, extending from the caudal pole of the facial (VII) motor nucleus of the hindbrain (Smith & Feldman 1987) to the phrenic (C3-C5) motor nucleus of the cervical spinal cord. The entire VRC contributes to the coordinated motor pattern in living animals, but there are functionally significant distinctions among the constituent respiratory neurons and nuclei. The caudal ventrolateral respiratory group (cVRG), as the most caudal part of the VRC, which is generally caudal to the level of the area postrema, contains bulbospinal premotoneurons that project to internal intercostal and abdominal respiratory motoneurons in the ventral horn of the thoracolumbar cord to carry out expiration movements (Blessing 1997). The rostral ventrolateral respiratory group (rVRG), at the level of the area postrema and rostral to the cVRG, contains bulbospinal inspiratory neurons projecting to the phrenic nucleus and to the thoracic ventral horn (Blessing 1997). At the rostral-most portion of the VRC, ventral and ventromedial to the compact division of the nucleus ambiguus (NA), a group of principally expiratory bulbospinal premotoneurons and expiratory interneurons named the Böttinger complex (BötC), was hypothesized to be the expiratory rhythm-generating kernel (Bianchi et al. 1995; Feldman & McCrimmon 1999). Arguably the most key site from the standpoint of rhythmogenesis is the region named the preBöttinger complex (preBötC), which is just caudal to the BötC and rostral to the rVRG, has been proposed to contain propriomedullary interneurons that have specialized role in inspiratory rhythm generation (Feldman et al. 2012): preBötC neurons are necessary for breathing in awake intact adult rodents, as well as necessary and sufficient for breathing rhythms *in vitro* (Ramirez et al. 1998; Gray et al. 2001; McKay et al. 2005; Gray et al. 1999; Smith et al. 1991; Tan et al. 2008). When recorded *in vivo* or *in vitro*, preBötC neurons commence spiking activity at an early stage 300-600 ms prior to inspiration (Rekling et al. 1996; Hayes & Del Negro 2007; Guyenet & Wang 2001; Garcia et al

2011), and then proceed to generate a collective burst that propagates to cranial and spinal respiratory motor nuclei to drive the inspiratory phase of the breathing cycle (Koizumi et al. 2008; Smith et al. 1990).

**BREATHING CAN BE STUDIED *IN VITRO*.** The preBötC can be isolated in slice preparations that retain putatively rhythmogenic inspiratory interneurons. Under physiological conditions, slices remain rhythmically active and inspiratory motor activity is measurable via hypoglossal (XII) nerve output. During the fictive inspiration, neurons in the preBötC discharge robust bursts correlated with XII motor output. Slices have inherent limitations such as requiring an ionic or pharmacologic 'boost' in excitability, typically accomplished by elevating the extracellular K<sup>+</sup> concentration, or lowering extracellular Ca<sup>2+</sup> (Ruangkittisakul et al. 2011; Ruangkittisakul et al. 2007). Moreover, slices only preserve the preBötC and lack expiratory rhythm-generating circuits (Bianchi et al. 1995; Feldman and McCrimmon 1999) and peripheral sensory inputs. Therefore, the XII motor output pattern primarily reflects the inspiratory rhythm (Lieske et al. 2000; Ramirez & Lieske 2003; Smith et al. 1990). These slice preparations represent an advantageous *in vitro* model that can be studied in the context of fictive inspiratory-like behavior to discover the neural mechanisms for rhythm generation *in vivo* (Ramirez et al. 2002). Slice experiments starting from 1991 (Smith et al. 1991) until now, have largely motivated critical tests of hypotheses *in vivo* (Gray et al. 2001; Janczewski & Feldman 2006; Janczewski et al. 2002; Manzke et al. 2003; McKay et al. 2005; Tan et al. 2008).

**WHICH PREBÖTC NEURONS ARE RHYTHMOGENIC?** Approximately 50% of neurons in the preBötC are glycinergic (Winter et al. 2009), yet inhibitory neurotransmission is not obligatory for respiratory rhythm generation (Gray et al. 1999; Feldman & Smith 1989; Shao & Feldman 1997; Ren & Greer 2006). Glutamatergic neurons are known

to be essential for rhythmogenesis (Funk et al. 1993; Greer et al. 1991; Koshiya & Smith 1999; Wallen-Mackenzie et al. 2006), but peptidergic systems appear to be important as well (Gray et al. 1999; Guyenet et al. 2001; Guyenet et al. 2002; Stornetta et al. 2003; Wang et al. 2001). Neuropeptides including substance P (SP) and somatostatin (SST) act in the preBötC to modulate respiratory frequency (Gray et al. 1999; Tan et al. 2008; Rekling et al. 1996). Neurons that express the neurokinin-1 receptor (NK1R), for which SP is the endogenous ligand, are found at a high density in the preBötC and the nearby nucleus ambiguus (Gray et al. 1999; Wang et al. 2001). NK1R<sup>+</sup> neurons, recorded *in vivo* and *in vitro*, express rhythmogenic membrane properties including pre-inspiratory firing patterns (Hayes & Del Negro 2007; Guyenet & Wang 2001). SST and the SST-2a receptor (SST2aR) are also markers that are highly expressed in the preBötC (Stornetta et al. 2003; Gray et al. 2010). SST<sup>+</sup> and SST2aR<sup>+</sup> neurons in the preBötC frequently express NK1Rs too, and thus may share similar functional properties. Importantly, SST<sup>+</sup>/SST2aR<sup>+</sup> and NK1R<sup>+</sup> neurons are glutamatergic (Stornetta et al. 2003; Gray et al. 2010). These data suggest that peptide-sensitive glutamatergic neurons, which also co-release SST, form the rhythmogenic kernel in the preBötC.

To test the hypothesis that peptide receptor expressing neurons comprise the rhythmogenic kernel of the preBötC, the ribosomal toxin saporin conjugated to SP was injected into the preBötC to produce targeted ablation of NK1R<sup>+</sup> neurons over several days (Gray et al. 2001; McKay et al. 2005). Freely behaving adult rats showed a progressive diminution of breathing behavior that led to ataxic breathing, respiratory pathology, and death. In another experiment, transient genetic silencing of SST<sup>+</sup> neurons in the preBötC *in vivo* using the K<sup>+</sup> channel-coupled allatostatin receptor (Tan et al. 2008) caused reversible apneas wherein the animal subjects had

to be mechanically ventilated to prevent asphyxiation (until the effects of allatostatin washed out).

The experiments above demonstrated the existence of an essential preBötC core containing a subset of glutamatergic neurons that are either SST<sup>+</sup> or NK1R<sup>+</sup>. But questions remain: do these neuropeptide receptor-expressing neurons reflect the same or overlapping subpopulations? Because these questions remain unanswered, the cellular composition of the preBötC remains somewhat ambiguous.

**DBX1-DERIVED NEURONS IN THE PREBÖTC MAY DEFINE THE RHYTHMOGENIC CORE.** Glutamatergic NK1R<sup>+</sup> and SST<sup>+</sup>/SST2aR<sup>+</sup> neurons in the preBötC are both derived from the homeodomain transcription factor Dbx1, which influences brainstem and spinal cord development (Lanuza et al. 2004; Pierani et al. 2001; Gray 2008). In the mouse embryo, *Dbx1* expression controls the fate of glutamatergic commissural interneurons in the hindbrain, including rhythm-generating preBötC neurons (Gray et al. 2010; Bouvier et al. 2010). Dbx1<sup>+</sup> neurons in the preBötC have been recorded *in vitro* and it is now known that they are inspiratory (Gray et al. 2010; Bouvier et al. 2010). Therefore, Dbx1<sup>+</sup> neurons express the anatomical and physiological properties that suggest an integral role in respiratory rhythm.

In addition, given that *Dbx1* mutant mice do not generate breathing either *in vivo* or *in vitro* (Gray et al. 2010; Bouvier et al. 2010), it is hypothesized that inspiratory rhythm in preBötC is generated by Dbx1-derived neurons as they meet many of the criteria for respiratory rhythm generation (Feldman & Del Negro 2006; Garcia et al. 2011).

**CHARACTERIZATION AND QUANTIFICATION OF DBX1-DERIVED NEURONS IN THE PREBÖTC.** Previous studies have investigated the membrane properties implicated in rhythm generation. However, these examinations were carried out without regard to the

genotype or transmitter phenotype of the preBötC neurons studied. Thus, an overarching question that pertains to the cellular-level mechanisms of respiratory rhythmogenesis still remain unsolved: do Dbx1-derived neurons comprise the respiratory rhythmogenic core and how can we properly characterize them to understand the cellular-synaptic mechanisms underlying rhythm generation? Moreover, in order to establish a general model of disease with a central etiology that leads to central respiratory failure, we also addressed the question pertaining quantification of basic network properties: how do graded lesions of Dbx1<sup>+</sup> neurons impact rhythm-generating capability and how many cell ablations were required to perturb or stop breathing? Our group addressed these two issues with two specific research projects that were carried out in parallel. On one hand, we analyzed the expression of the membrane properties and the morphological properties of Dbx1<sup>+</sup> neurons in preBötC to examine how Dbx1<sup>+</sup> neurons underlie respiratory rhythmogenesis (Picardo 2012). On the other hand, we developed an *in vitro* laser-lesion technique to cumulatively ablate Dbx1<sup>+</sup> neurons in a controlled sequence in the preBötC. This approach simulates the graded neuronal destruction of networks, which can serve as a model of neurodegenerative disease. Our studies may provide new knowledge about the genetic and cellular underpinnings of breathing behavior in mammals and help quantify the sustainability of the respiratory CPG when facing progressive neuronal loss. We believe our work will be of widespread interest among neuroscientists because it pertains to the genetic and cellular origins and the basic network properties of a key physiological behavior.

**BROADER SIGNIFICANCE: GRADED LESIONS, RHYTHMOGENESIS, AND DISEASE MODELS.**

Adult rats subjected to chronic saporin lesions provide a model of respiratory failure with a central etiology (McKay et al. 2005), which often occurs in the elderly and in patients suffering neurodegenerative disorders such as *multiple systems atrophy*



(MSA) (Benarroch 2003; Benarroch et al. 2003) and Parkinson disease (Maria et al. 2003). However, these experiments could not measure how progressive loss of preBötC neurons correlates with deteriorating respiratory function. Thus the cellular mechanisms that lead to pathophysiology remain incompletely understood. Additionally, activating allatostatin receptors *in vivo* transiently silences a large fraction of the preBötC at once, which precludes studying the effects of graded neuron removal altogether (Tan et al. 2008). While wholesale silencing and chronic lesion experiments *in vivo* provided important new knowledge, both have limitations as disease models. We propose to overcome some of these limitations, and provide an important complement to *in vivo* approaches, by performing graded cell-specific lesions in an *in vitro* slice model of breathing activity. Neurons in the preBötC will be precisely identified by fluorescent markers (Dbx1-specific or rhythmic Ca<sup>2+</sup> activity) and then ablated in a controlled sequence. We will be able to quantify the effects on inspiratory motor output (XII discharge) as a function of number of cells destroyed in the preBötC.

Thus our new lesioning method may help elucidate the mechanisms contributing to respiratory failure in diseases including, but not limited to, MSA and Parkinsonism. This *in vitro* approach will also provide a model that may be broadly applicable to understanding neonatal breathing disorders such as *apnea of prematurity*, and could be readily adapted – using serotonergic neuronal markers – to study *sudden infant death syndrome* (SIDS) (Paterson et al. 2006). Our *in vitro* approach will also provide basic information that may help to understand diverse respiratory pathologies that impact sleep including *central sleep apnea* and *catathrenia* (Vetrugno et al. 2007), i.e., nocturnal groaning among other forms of sleep-disordered breathing (McKay et al. 2005). Neurons with low endogenous Ca<sup>2+</sup> buffers – including XII motoneurons and neurons in the preBötC (Alheid et al. 2002)

– are susceptible to degeneration and cell death in *amyotrophic lateral sclerosis* (ALS) (Alexianu et al. 1994). Thus, we can also provide a complementary *in vitro* model of ALS in which either XII motoneurons or preBötC neurons can be selectively ablated in graded fashion.

### ***Objective of this Dissertation***

We breathe, walk, and chew. Respiration, locomotion and ingestive behaviors all consist of rhythmic movements formed by central pattern generator (CPG) networks of the brainstem and spinal cord (Grillner 2006; Kiehn 2011; Garcia-Campmany et al. 2010). In addition to asking which cell types generate the behavior, we investigate another key issue: how many cells contribute to sustaining these patterns of activity. This question pertains to whether and how cumulative cell loss will impair, and possibly preclude, behaviorally relevant network function. Given that previous studies have helped to determine the cellular composition of the preBötC (Feldman & Del Negro 2006; Smith et al. 1991; Gray et al. 2001; McKay et al. 2005; Tan et al. 2008) but could not measure the resiliency of respiratory network function when faced with silencing or deleting its kernel piecewise, an unresolved issue is to what extent network function is robust in the face of cumulative cell destruction. We designed a unique experimental approach to address three issues: 1) how many neurons are necessary for comprising the minimal rhythmogenic core; 2) how graded lesions impact rhythm-generating capability; and, 3) what this progression can teach us about disease.

In the first chapter, we present an automated cell-specific lesion system that was designed for identifying neurons within tissue slices and individually laser-ablating these neuron targets based on the expression of genotypic fluorescent markers or activity patterns. This system relies on a two-photon confocal microscope

for imaging and laser control, while using a Ti:sapphire laser for localized spot ablation of single neurons. A critical feature of this system is custom software package we wrote in house that autonomously controls stage translation, identifies cell targets, focuses the laser and implements the spot-lesion protocol. We sought to test the sensitivity of respiratory behavior *in vitro* by serial laser ablation using the preBötC neural circuits in mammalian respiratory CPG.

The second chapter is aimed at 1) implementing a *dynamic target detection* module to automatically identify neuron targets based on imaged activity pattern, e.g., Ca<sup>2+</sup> imaging; 2) examining if cumulative deletion of functionally defined rhythmically active neurons in preBötC cause significant, deleterious effects measurable at the system level and how the destruction will impair the network function behaviorally. Aim #1 was achieved by performing a series of image transforms and Fourier analysis to the acquired time-series Ca<sup>2+</sup> stacks, in order to extract extensive fluorescence fluctuations in a user defined frequency band from acquisition. Lesioning of these precisely selected oscillatory targets reveals striking results - on average, the deletion of 120±45 neurons stopped spontaneous respiratory rhythm, and our data suggest ~82% of the rhythm generating neurons remain un-lesioned.

The subsequent investigation in **Chapter 3** examines the issue by applying the same technique protocols but adopting different animal model, which allows us to directly detect neuron targets on the basis of *Dbx1* established genetic marker of the preBötC. To test the role of *Dbx1*-derived neurons in respiratory rhythmogenesis, *Dbx1*<sup>+</sup> neurons are detected and ablated in the preBötC of neonatal *Dbx1*-EYFP reporter (*Dbx1*<sup>+/CreERT2</sup>;*Rosa26*<sup>EYFP</sup>) and *Dbx1*-tdTomato reporter (*Dbx1*<sup>+/CreERT2</sup>;*Rosa26*<sup>tdTomato</sup>) mouse pups. We designed a *static target detector* module to

find the local maxima of fluorescence intensity, i.e., putative Dbx1<sup>+</sup> fluorescent neurons. Following this new detection strategy, sequential laser ablation is carried out to examine how graded neuronal destruction of Dbx1<sup>+</sup> cells in preBötC abruptly result in loss of rhythmic motor output. As a consequence, our experimental data suggest that the deletion of  $85 \pm 45$  Dbx1<sup>+</sup> neurons in preBötC causes severe and irreversible damage to the rhythm-generating core and ultimately leads to rhythm cessation *in vitro*.

We hope the technique described in this dissertation, which have provided a new powerful means to investigate the structure of networks to determine whether specific elements functions as hubs of synaptic integration, may be of great value for studying rhythmic behaviors *in vitro*. In addition, the data contained in this dissertation will be the first studies that interrogate network properties of the mammalian respiratory CPG based on a cumulative lesion approach with single-cell precision. These results provide a novel measurement that can help quantify network properties of the preBötC and gauge its susceptibility to failure. Furthermore, these new discoveries may also advance our understanding of central nervous system (CNS) related etiology of many neurodegenerative diseases.

## References

- Alheid GF, Gray PA, Jiang MC, Feldman JL, McCrimmon DR (2002)** Parvalbumin in respiratory neurons of the ventrolateral medulla of the adult rat. *J Neurocytol* 31:693-717.
- Alexianu ME, Ho BK, Mohamed AH, La Bella V, Smith RG, Appel SH (1994)** The role of calcium-binding proteins in selective motoneuron vulnerability in amyotrophic lateral sclerosis. *Ann Neurol* 36:846-858.
- Benarroch EE (2003)** Brainstem in multiple system atrophy: clinicopathological correlations. *Cell Mol Neurobiol* 23:519-526.
- Benarroch EE, Schmeichel AM, Low PA, Parisi JE (2003)** Depletion of ventromedullary NK-1 receptor-immunoreactive neurons in multiple system atrophy. *Brain* 126:2183-2190.
- Bianchi AL, Denavit-Saubie M, Champagnat J (1995)** Central control of breathing in mammals: neuronal circuitry, membrane properties, and neurotransmitters. *Physiol Rev* 75:1-45.
- Blessing WW (1997)** *The lower brainstem and bodily homeostasis*. New York: Oxford University Press.
- Bouvier J, Thoby-Brisson M, Renier N, Dubreuil V, Ericson J, Champagnat J, Pierani A, Chedotal A, Fortin G (2010)** Hindbrain interneurons and axon guidance signaling critical for breathing. *Nat Neurosci* 13:1066-1074.
- Feldman JL, Del Negro CA (2006)** Looking for inspiration: new perspectives into the generation of respiratory rhythm. *Nat Rev Neurosci*.

**Feldman JL, McCrimmon DR (1999)** Neural control of breathing. In: *Fundamental neuroscience* (Zigmond, M. J., ed), pp 1063-1090 San Diego: Academic Press.

**Feldman JL, McCrimmon DR (2002)** Neural control of breathing. In: *FUNDAMENTAL NEUROSCIENCE* (Squire, L. R. et al., eds), p Chapter 37: Academic Press.

**Feldman JL, McCrimmon DR, Smith JC, Ellenberger HH, Speck DF (1986)** Respiratory pattern generation in mammals. In: *Neurobiology of the Control of Breathing*, 10th Nobel Symposium (von Euler, C. and Lagercrantz, H., eds), pp 157-164 New York: Raven Press.

**Feldman JL, Mitchell GS, Nattie EE (2003)** Breathing: Rhythmicity, Plasticity, Chemosensitivity. *Annu Rev Neurosci* 26:239–266.

**Feldman JL, Smith JC (1989)** Cellular mechanisms underlying modulation of breathing pattern in mammals. *Ann N Y Acad Sci* 563:114-130.

**Funk GD, Smith JC, Feldman JL (1993)** Generation and transmission of respiratory oscillations in medullary slices: role of excitatory amino acids. *J Neurophysiol* 70:1497-1515.

**Garcia, A. J., 3rd, Zanella, S., Koch, H., Doi, A. & Ramirez, J. M. (2011)** *Chapter 3 - networks within networks: the neuronal control of breathing*. Progress in brain research 188, 31-50.

**Garcia-Campmany, L., Stam, F. J. & Goulding, M. (2010)** From circuits to behaviour: motor networks in vertebrates. *Curr Opin Neurobiol* 20, 116-125.

**Gray PA (2008)** Transcription factors and the genetic organization of brain stem respiratory neurons. *J Appl Physiol* 104:1513-1521.

**Gray PA, Hayes JA, Ling GY, Llona I, Tupal S, Picardo MC, Ross SE, Hirata T, Corbin JG, Eugenin J, Del Negro CA (2010)** Developmental origin of preBötzinger complex respiratory neurons. *The Journal of neuroscience* : the official journal of the Society for Neuroscience 30:14883-14895.

**Gray PA, Janczewski WA, Mellen N, McCrimmon DR, Feldman JL (2001)** Normal breathing requires preBötzinger complex neurokinin-1 receptor-expressing neurons. *Nat Neurosci* 4:927-930.

**Gray PA, Rekling JC, Bocchiario CM, Feldman JL (1999)** Modulation of respiratory frequency by peptidergic input to rhythmogenic neurons in the preBötzinger complex. *Science* 286:1566-1568.

**Greer JJ, Smith JC, Feldman JL (1991)** Role of excitatory amino acids in the generation and transmission of respiratory drive in neonatal rat. *The Journal of physiology* 437:727-749.

**Grillner S (2006)** Biological pattern generation: the cellular and computational logic of networks in motion. *Neuron* 52:751-766.

**Guyenet PG, Sevigny CP, Weston MC, Stornetta RL (2002)** Neurokinin-1 receptor-expressing cells of the ventral respiratory group are functionally heterogeneous and predominantly glutamatergic. *The Journal of neuroscience* : the official journal of the Society for Neuroscience 22:3806-3816.

**Guyenet PG, Wang H (2001)** Pre-Bötzinger neurons with preinspiratory discharges "in vivo" express NK1 receptors in the rat. *Journal of neurophysiology* 86:438-446.

**Hayes JA, Del Negro CA (2007)** Neurokinin receptor-expressing pre-Bötzinger complex neurons in neonatal mice studied in vitro. *Journal of neurophysiology* 97:4215-4224.

**Janczewski WA, Feldman JL (2006)** Distinct rhythm generators for inspiration and expiration in the juvenile rat. *J Physiol* 570:407-420.

**Janczewski WA, Onimaru H, Homma I, Feldman JL (2002)** Opioid-resistant respiratory pathway from the preinspiratory neurones to abdominal muscles: in vivo and in vitro study in the newborn rat. *J Physiol* 545:1017-1026.

**Kiehn O (2011)** Development and functional organization of spinal locomotor circuits. *Curr Opin Neurobiol* 21:100-109.

**Koizumi H, Wilson CG, Wong S, Yamanishi T, Koshiya N, Smith JC (2008)** Functional imaging, spatial reconstruction, and biophysical analysis of a respiratory motor circuit isolated in vitro. *The Journal of neuroscience* : the official journal of the Society for Neuroscience 28:2353-2365.

**Koshiya N, Smith JC (1999)** Neuronal pacemaker for breathing visualized in vitro. *Nature* 400:360-363.

**Lanuza GM, Gosgnach S, Pierani A, Jessell TM, Goulding M (2004)** Genetic identification of spinal interneurons that coordinate left-right locomotor activity necessary for walking movements. *Neuron* 42:375-386.

**Lieske SP, Thoby-Brisson M, Telgkamp P, Ramirez JM (2000)** Reconfiguration of the neural network controlling multiple breathing patterns: eupnea, sighs and gasps [see comment]. *Nat Neurosci* 3:600-607.



**Manzke T, Guenther U, Ponimaskin EG, Haller M, Dutschmann M, Schwarzacher S, Richter DW (2003) 5-HT4(a) receptors avert opioid-induced breathing depression without loss of analgesia. *Science* 301:226-229.**

**Maria B, Sophia S, Michalis M, Charalampos L, Andreas P, John ME, Nikolaos SM (2003) Sleep breathing disorders in patients with idiopathic Parkinson's disease. *Respir Med* 97:1151-1157.**

**McKay LC, Janczewski WA, Feldman JL (2005) Sleep-disordered breathing after targeted ablation of preBötzinger complex neurons. *Nat Neurosci* 8:1142-1144.**

**Onimaru H, Arata A, Homma I (1997) Neuronal mechanisms of respiratory rhythm generation: an approach using in vitro preparation. *The Japanese journal of physiology*.**

**Paterson DS, Trachtenberg FL, Thompson EG, Belliveau RA, Beggs AH, Darnall R, Chadwick AE, Krous HF, Kinney HC (2006) Multiple serotonergic brainstem abnormalities in sudden infant death syndrome. *Jama* 296:2124-2132.**

**Picardo MC (2012) Physiological and Morphological Characterization of Genetically Defined Classes of Interneurons in Respiratory Rhythm and Pattern Generation in Neonatal Mice. *Dissertation*.**

**Pierani A, Moran-Rivard L, Sunshine MJ, Littman DR, Goulding M, Jessell TM (2001) Control of interneuron fate in the developing spinal cord by the progenitor homeodomain protein Dbx1. *Neuron* 29:367-384.**

**Ramirez JM, Lieske SP (2003) Commentary on the definition of eupnea and gasping. *Respir Physiol Neurobiol* 139:113-119.**

**Ramirez JM, Schwarzacher SW, Pierrefiche O, Olivera BM, Richter DW (1998)** Selective lesioning of the cat pre-Bötzinger complex in vivo eliminates breathing but not gasping. *J Physiol (Lond)* 507:895-907.

**Ramirez JM, Zuperku EJ, Alheid GF, Lieske SP, Ptak K, McCrimmon DR (2002)** Respiratory rhythm generation: converging concepts from in vitro and in vivo approaches? *Respir Physiol Neurobiol* 131:43-56.

**Ruangkittisakul, A., Panaitescu, B. & Ballanyi, K. (2011)** K(+) and Ca(2)(+) dependence of inspiratory-related rhythm in novel "calibrated" mouse brainstem slices. *Respir Physiol Neurobiol* 175, 37-48.

**Ruangkittisakul, A., Secchia, L., Bornes, T. D., Palathinkal, D. M. & Ballanyi, K. (2007)** Dependence on extracellular Ca<sup>2+</sup>/K<sup>+</sup> antagonism of inspiratory centre rhythms in slices and en bloc preparations of newborn rat brainstem. *J Physiol* 584, 489-508.

**Rekling JC, Champagnat J, Denavit-Saubie M (1996)** Electroresponsive properties and membrane potential trajectories of three types of inspiratory neurons in the newborn mouse brain stem in vitro. *J Neurophysiol* 75:795-810.

**Rekling JC, Feldman JL (1998)** PreBötzinger complex and pacemaker neurons: hypothesized site and kernel for respiratory rhythm generation. *Annu Rev Physiol* 60:385-405.

**Ren J, Greer JJ (2006)** Modulation of respiratory rhythmogenesis by chloride-mediated conductances during the perinatal period. *The Journal of Neuroscience* : the official journal of the Society for Neuroscience 26:3721-3730.

**Richter DW (1982)** Generation and maintenance of the respiratory rhythm. *J. Exp. Biol.* 100:93-107.

**Richter DW, Spyer KM (2001)** Studying rhythmogenesis of breathing: comparison of in vivo and in vitro models. *Trends Neurosci* 24:464-472.

**Shao XM, Feldman JL (1997)** Respiratory rhythm generation and synaptic inhibition of expiratory neurons in pre-Bötzinger complex: differential roles of glycinergic and GABAergic neural transmission. *Journal of Neurophysiology* 77:1853-1860.

**Smith JC, Ellenberger HH, Ballanyi K, Richter DW, Feldman JL (1991)** Pre-Bötzinger complex: a brainstem region that may generate respiratory rhythm in mammals. *Science* 254:726-729.

**Smith JC, Feldman JL (1987)** In vitro brainstem-spinal cord preparations for study of motor systems for mammalian respiration and locomotion. *J. Neurosci. Methods* 21:321-333.

**Smith JC, Greer JJ, Liu GS, Feldman JL (1990)** Neural mechanisms generating respiratory pattern in mammalian brain stem-spinal cord in vitro. I. Spatiotemporal patterns of motor and medullary neuron activity. *Journal of Neurophysiology* 64:1149-1169.

**Stornetta RL, Rosin DL, Wang H, Sevigny CP, Weston MC, Guyenet PG (2003)** A group of glutamatergic interneurons expressing high levels of both neurokinin-1 receptors and somatostatin identifies the region of the pre-Bötzinger complex. *J Comp Neurol* 455:499-512.

**Suzue T (1984)** Respiratory rhythm generation in the in vitro brain stem-spinal cord preparation of the neonatal rat. *The Journal of Physiology* 354:173-183.

**Tan W, Janczewski WA, Yang P, Shao XM, Callaway EM, Feldman JL (2008)** Silencing preBötzing complex somatostatin-expressing neurons induces persistent apnea in awake rat. *Nature Neuroscience* 11:538-540.

**Vetrugno R, Lugaresi E, Plazzi G, Provini F, D'Angelo R, Montagna P (2007)** Catathrenia (nocturnal groaning): an abnormal respiratory pattern during sleep. *European Journal of Neurology* : the official journal of the European Federation of Neurological Societies 14:1236-1243.

**Wallen-Mackenzie A, Gezelius H, Thoby-Brisson M, Nygard A, Enjin A, Fujiyama F, Fortin G, Kullander K (2006)** Vesicular glutamate transporter 2 is required for central respiratory rhythm generation but not for locomotor central pattern generation. *The Journal of Neuroscience* : the official journal of the Society for Neuroscience 26:12294-12307.

**Wang H, Stornetta RL, Rosin DL, Guyenet PG (2001)** Neurokinin-1 receptor-immunoreactive neurons of the ventral respiratory group in the rat. *J Comp Neurol* 434:128-146.

**Winter SM, Fresemann J, Schnell C, Oku Y, Hirrlinger J, Hulsman S (2009)** Glycinergic interneurons are functionally integrated into the inspiratory network of mouse medullary slices. *Pflugers Archiv* : European journal of physiology 458:459-469.

# CHAPTER 1. Automated cell-specific laser detection and ablation system *in vitro*

## 1.1. Introduction

Lesion tools allow neuroscientists to examine the cellular bases for behaviors and to model neuropathology. Ideally, one removes particular neurons from a circuit via ablation, and then measures the effect on network functionality. However, gaining new knowledge from this type of experimental paradigm depends on three key factors: 1) how selectively a class of neurons can be distinguished from its neighbors and thus targeted for ablation, 2) how accurately the neurons of interest can be ablated while minimizing damage to surrounding tissues, and 3), how sensitively lesion effects on network output can be monitored.

Here we demonstrate a cell-specific laser detection and ablation instrument system. It is designed for use in reduced preparations that retain behaviorally relevant activity *in vitro* or *in situ*. An ultra-fast, long-wavelength laser is used to detect specific neuron classes based on genetically encoded fluorescent reporter proteins or functional criteria such as rhythmic  $\text{Ca}^{2+}$  activity. The three-dimensional (3D) coordinates of cell somata are stored as a list of targets in memory. Cell targets are drawn from the list randomly, or in any user-defined sequence, and then laser-ablated one at a time while monitoring network function via electrophysiology. Network output can be measured via cranial or spinal nerve roots or via intracellular recordings. Neurons can thus be cumulatively removed via ablation while the functional capacity of the network is vigilantly measured in real time. Subsequent perturbations of network output can be directly attributed to the lesioned neurons because the tally and map of ablated neurons are tracked in real time too. Open-

source executive software controls all the hardware and carries out the protocol. Two-photon excitation provides confocal specificity and control of each lesion in 3D, while causing no extraneous damage to surrounding neural tissue. This laser detection and ablation system can be added-on to an existing two-photon laser scanning microscope at low cost while expanding the scope of possible experiments to include active interrogation of network functionality in living specimens via cumulative single-cell laser ablations *in vitro* or *in situ*.

## 1.2. Methods

### ***Neonatal mouse slice preparation maintained in vitro***

The Institutional Animal Care and Use Committee at The College of William & Mary approved the following protocols. We use C57BL/6 (wild type, WT) and transgenic mice that express *Cre* recombinase fused to the tamoxifen-sensitive estrogen receptor in neurons that express the transcription factor *Dbx1* (Developing Brain Homeobox-1) gene, *Dbx1<sup>+CreERT2</sup>* (Hirata et al. 2009). *Dbx1<sup>+CreERT2</sup>* mice are coupled with *floxed* reporter mice with inducible expression of the red fluorescent protein variant tdTomato Gt(ROSA)26Sor locus1 (*Rosa26<sup>tdTomato</sup>*, Jax No. 007905) (Madisen et al. 2010) to obtain mice in which *Dbx1*-derived (*Dbx1<sup>+</sup>*) neurons can be identified by red fluorescence in the soma and dendrites. The *Dbx1<sup>+CreERT2</sup>* strain is bred in-house using a CD-1 background strain. The *Rosa26<sup>tdTomato</sup>* is maintained as a homozygous line with C57BL/6J background. We verify animal genotype via polymerase chain reaction (PCR) using primers specific for *Cre* and *tdRFP* (Transnetyx, Cordova, TN). We also use *Dbx1<sup>+LacZ</sup>* mice on a C57BL/6J background (Pierani et al. 2001) and identify heterozygous mutants using fluorescein-di-β-d-galactopyranoside (FDG) (Gray et al. 2010).

Neonatal mice aged postnatal days 0-3 (P0-3) are anesthetized and dissected in artificial cerebrospinal fluid (ACSF) containing (in mM): 124 NaCl, 3 KCl, 1.5 CaCl<sub>2</sub>, 1 MgSO<sub>4</sub>, 25 NaHCO<sub>3</sub>, 0.5 NaH<sub>2</sub>PO<sub>4</sub>, and 30 D-glucose, equilibrated with 95% O<sub>2</sub> and 5% CO<sub>2</sub> (pH=7.4). The neuraxis is isolated and pinned onto a paraffin-coated paddle, with its rostral side up and ventral surface facing out. The paddle is fixed into the vise of a vibrating microtome for sectioning in the transverse plane. We cut 450-500- $\mu$ m-thick slices from the medulla to prepare transverse slices that expose the preBötC at the slice surface.

### ***Fluorescent labeling of Dbx1<sup>+</sup> neurons***

*Dbx1<sup>LacZ</sup>* homozygous mutants die at birth of respiratory failure (Pierani et al. 2001, Gray et al. 2010, Bouvier et al. 2010). We cross WT and *Dbx1<sup>+LacZ</sup>* mice to obtain viable heterozygous pups that develop normally and express the *LacZ* gene product  $\beta$ -galactosidase ( $\beta$ gal) during embryogenesis and neonatal development (Pierani et al. 2001; Lanuza et al. 2004). Brainstem slices from *Dbx1<sup>+LacZ</sup>* mice are incubated in ACSF containing 1.5 mg/ml of fluorescein-di- $\beta$ -d-galactopyranoside (FDG) for 30 min at 37° C. The *LacZ* gene product  $\beta$ gal activates fluorescein and facilitates fluorescent identification of *Dbx1<sup>+</sup>* neurons.

We cross *Dbx1<sup>+CreERT2</sup>* mice with *Rosa26<sup>tdTomato</sup>* Cre-dependent reporter mice to obtain *Dbx1<sup>+CreERT2</sup>;Rosa26<sup>tdTomato</sup>* pups. Tamoxifen administration to pregnant female mice on the 10<sup>th</sup> day after the plug date produces fluorescent *Dbx1<sup>+</sup>* neurons in ~50% of the offspring. Using epifluorescence microscopy with a band-pass emission filter (546-558 nm), a dichroic mirror (560 nm), and a band-pass barrier filter (575-640 nm), *Dbx1<sup>+</sup>* neurons can be readily visualized in the preBötC and contiguous regions of the dorsomedial medulla.

### ***Loading Ca<sup>2+</sup>-sensitive fluorescent dye***

Slices are loaded with the Ca<sup>2+</sup>-sensitive dye Quest Fluo-8 AM (AAT Bioquest, Sunnyvale, CA) for the purpose of fluorescent Ca<sup>2+</sup> imaging of rhythmically active preBötC respiratory neurons. The slices are submerged in a loading solution in 1.5 ml centrifuge tube for 1.5-2 hours in the dark at 37° C. Loading solution consisted of 90 µl of 9 mM K<sup>+</sup> ACSF, 10 µL D-mannitol stock solution (1 M), and 5 µl of Fluo-8 stock solution (50 µg Fluo-8 dissolved in 60 or 30 µl Pluronic® F-127 20% solution in DMSO) for a final Fluo-8 concentration of 32 or 64 µM.

After incubation in Fluo-8 AM loading solution, slices are mounted in a recording chamber and perfused with 27°C ACSF at 4 ml/min. The external potassium concentration ([K<sup>+</sup>]<sub>o</sub>) of the standard ACSF is raised to 9 mM and inspiratory motor output is recorded from XII nerve roots.

Particularly for WT experiments, we typically add 5-µM picrotoxin and 5-µM strychnine to the ACSF before the imaging acquisition to block chloride-mediated inhibitory transmission (disinhibition) before the detection phase of the experiment.

### ***Image acquisition***

We use a fixed-stage upright laser-scanning confocal microscope (LSM 510, Carl Zeiss Inc, Thornwood, NY) equipped with three confocal visible-wavelength lasers and a tunable (710-920 nm) mode-locked Ti:sapphire laser (Mai Tai Rad X, Spectra Physics, Irvine, CA). The Ti:sapphire laser generates pulses of 100 femtosecond duration (100 fs) at wavelength 800 nm. The average power of the pulsed Ti:sapphire laser emitted at ~1 W and measure ~30 mW through the objective at the specimen plane. A 120-W metal halide lamp (EXFO Life Sciences, Montreal, Québec, Canada) is used for rapid screening of the tissue via epifluorescence. All experiments employ a 20x/1.0 numerical aperture (NA) water-immersion objective.



The LSM 510 scan head contains three internal descanned detectors, two external non-descanned detectors used to collect fluorescent emissions, one sub-stage descanned detector for bright-field and infrared-enhanced differential interference contrast (IR-DIC) imaging, and a 12-bit cooled charge-coupled device camera (AxioCam MRm, Zeiss). The AxioCam MRm is used for videomicroscopy in real time applications, to position the slice and recording electrodes, and then to find the rhythmically active collection of neurons corresponding to the preBötC. The recording chamber is secured on a robotic X-Y translation stage (Siskiyou Corp., Grants Pass, OR), which is used to adjust the position of the slice preparation, in particular to move the imaging plane between bilaterally distributed regions of the preBötC. The robotics are manually controlled at the start of the experiments, and then computer-controlled during the automated phases of the experiments (see ***Detecting and lesioning neuron targets*** below).

### ***Electrophysiology***

Inspiratory motor rhythms are recorded from the XII nerve roots using suction electrodes (A-M Systems, Sequim, WA) with custom-fabricated fire-polished tips (inner diameter: 40-100  $\mu\text{m}$ ), a differential amplifier (gain 20k, band-pass filtered at 0.3-1 kHz, Dagan Instruments, Minneapolis, MN), and a 16-bit PowerLab 4-channel data acquisition system (ADInstruments, Colorado Springs, CO). The XII motor output is routinely well above baseline such that signal-to-noise ratio is never an issue; detectability of the signal is guaranteed. XII output is full-wave rectified and smoothed for display.

We perform whole-cell recordings using an EPC-10 amplifier (HEKA Electronic, Bellmore, NY). Standard patch solution contained (in mM): 140 K-Gluconate, 10 NaCl, 0.5 CaCl<sub>2</sub>, 10 HEPES, 1 EGTA, 2 Mg-ATP, and 0.3 Na<sub>3</sub>-GTP

(pH 7.3). We add 50  $\mu$ M Alexa 568 hydrazide (Invitrogen, Carlsbad, CA) prior to use for fluorescent identification of the recorded neurons. All electrophysiology data are low-pass filtered at 1 kHz and digitally acquired at 10 kHz using a 16-bit A/D converter.

Most lesion experiments are done without intracellular recordings, but this additional form of measurement at the single-cell level can be performed in conjunction with the detection and lesion experiment, which is in essence a system-level experiment.

### ***System setup***

The instrument includes a master computer that controls a Ti:sapphire long-wavelength laser, a laser-scanning microscope with visible wavelength lasers and non-descanned detectors, as well as a customized robotic xy translation stage with specimen chamber. Another computer, time-synced to the master, monitors network activity via electrophysiology (Fig. 1.1). A software package dubbed *Ablator* automates the experiments, which consist of three phases. The *initialization phase* defines the domain of the target area. Next, the *detection phase* employs two-photon and/or confocal microscopy with image processing to map cell populations in 3D and arrive at a final target list. Finally, the *ablation phase* selects the order and then sequentially destroys (or attempts to destroy) each entry in the target list until all the targets are exhausted. Physiological monitoring takes place continuously during the detection and ablation phases (Fig. 1.2).

### ***'Ablator' executive software***

We wrote a suite of Python-language scripts that control all operations of the lesioning experiments including microscopy, motorized xy stage translation, online

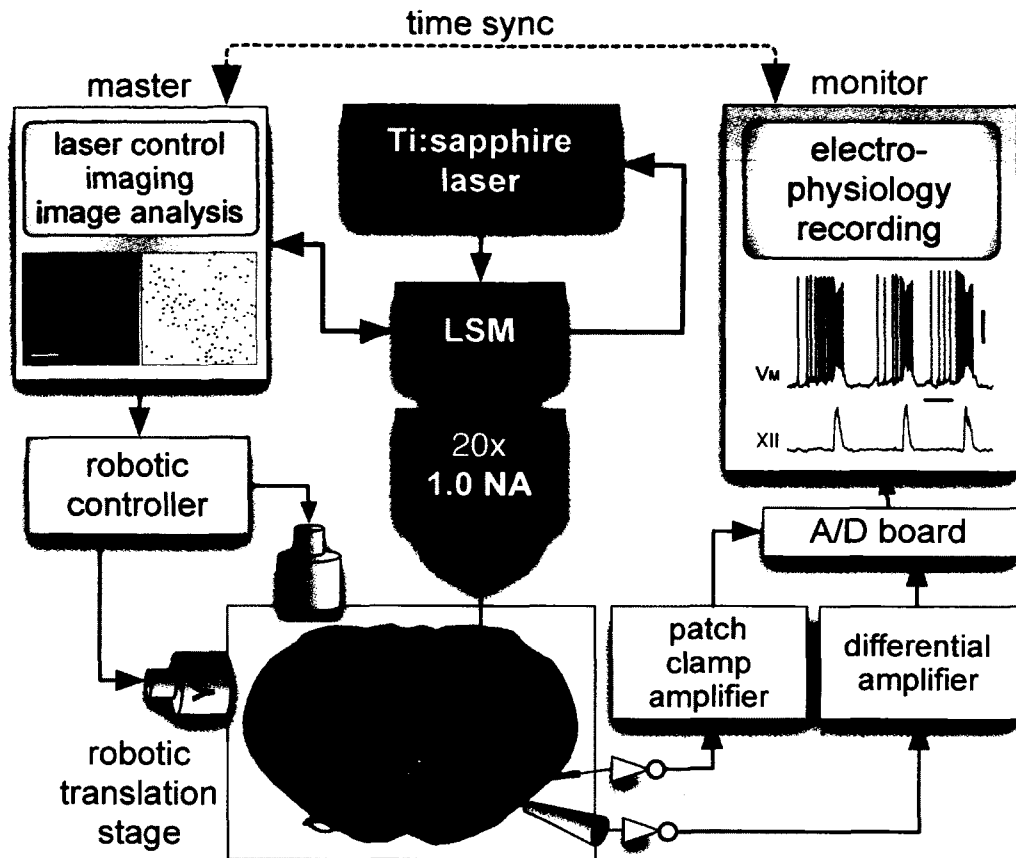


**Figure 1.1** Schematic diagram of the integrated instrument. The master computer (left) controls the Ti:sapphire laser as well as the laser scanning microscope (LSM) and robotic xy translation stage. The master also runs Ablator executive software to implement the protocols. The inset in the master computer panel represents image acquisition and analysis, scale bar shows 100  $\mu\text{m}$ . The robotic translation stage holds the specimen chamber where the inset image shows a slice preparation containing the preBötC. The monitoring computer (right) continuously performs extracellular suction electrode and/or patch-clamp recordings, which are standard tools to measure respiratory rhythm generation *in vitro*. The inset images reflect typical voltage trajectories for a preBötC neuron ( $V_M$ ) and integrated XII nerve root (a.u.) during spontaneous breathing-related activity *in vitro*. Calibration bars show 20 mV (applies to  $V_M$  trace) and 1 s (applies to both  $V_M$  and XII traces). Amplifiers and the analog-to-digital (A/D) converter are shown in the schematic too. Master and monitor computers are time synchronized.

analysis and target detection, target selection, as well as laser ablation using the Ti:sapphire laser. We call the software *Ablator*, which was constructed to be modular, which means it can potentially control additional microscopes, robotic stages, and other devices. The Python code is GPL-compatible open source programming

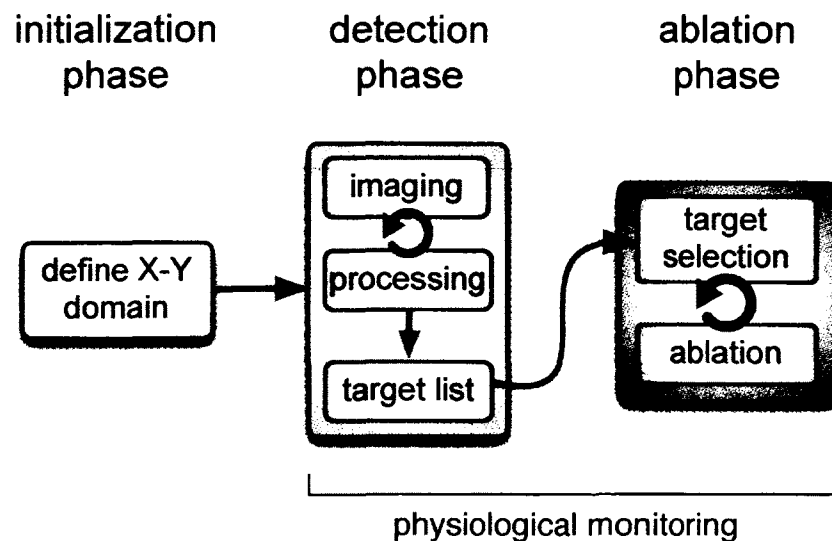


**Figure 1.2** Schematic diagram of the basic three-phase protocol: initialization, detection, and ablation. Each phase is described in the **Methods** section. Essential information obtained during each phase of the experiment is passed (rightward) to the subsequent phase. Circular arrows indicate iterative steps in the detection and ablation phases. Physiological monitoring takes place continuously during the detection and ablation phases.

language and features relatively simple syntax that facilitates cross-platform applicability and modularity. Ablator is available from the following website: <http://sourceforge.net/projects/ablator/>.

Ablator controls xy stage movements through a MC1000e (Siskiyou Corp., Grants Pass, OR) and its respective axis motors. It also controls LSM 510 imaging protocols through the proprietary Zeiss software, sets the wavelength and strength of the Ti:sapphire laser, and performs online image analyses via routines in a modified version of the open-source Java software *ImageJ* (National Institutes of Health, Bethesda, MD). Because of the modularity of the Ablator software, the detection and ablation routines can be adapted to other neurobiological applications.

*Software control of the motorized xy translation stage.* Ablator controls the position of the xy stage via a custom-made circuit (**Fig. 1.3**) that interfaces with a

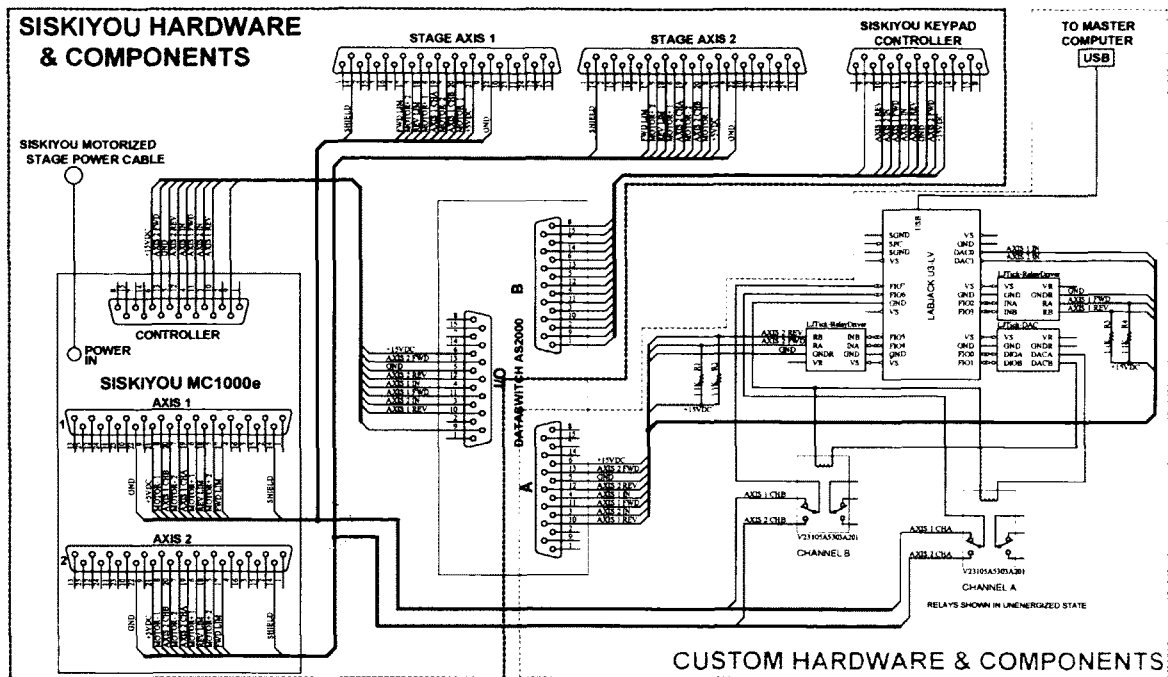


**Figure 1.3** Custom circuit to control the motorized xy translation stage. The blue dashed line outlines the commercial Siskiyou MC1000e motorized axes controller and its critical components (left), the AS2000 I/O dataswitch is a commercially-available D15 switch (center), and the custom hardware components necessary for software interface to the master computer (top-right) are wrapped in the red dashed line (right). The principal interface to the computer is through a USB connection to the LabJack U3-LV that is controlled through custom components of the Ablator software. The LabJack has three expansion slots as displayed: two LJTick-RelayDrivers for switching between forward and reverse for each axis motor, and one LJTick-DAC for controlling separate relays (V23105A5303A201) to switch between channel A (CHA) and channel B (CHB) of each axis motor, which allows the distance traversed of each motor to be recorded (FIO6/FIO7). Note that these CHA and CHB wires must be interfaced with the normal connections of the cables going into the axis motors and MC1000e (indicated by the joined connections within the violet dashed circle). The LabJack U3's DAC0/DAC1 determine the speed each respective axis motor is translated, the appropriate direction for each motor must be specified using FIO4/FIO5 and FIO2/FIO3, and the settings of FIO0/FIO1 determine which axis motor's feedback is reported to FIO6/FIO7 forming a closed-loop. Axis motors must be used serially and not concurrently for the latter reason.

LabJack U3 LV (LabJack Corp., Lakewood, CO) data acquisition device. Ablator controls the LabJack through its Python application-programming interface (API). This custom circuit manipulates the Siskiyou MC1000e while also receiving feedback on the distance traversed by the specimen stage after each command, thus forming a closed-loop feedback system for increased accuracy of spatial positioning from the Python scripts. A simple graphical user interface (GUI), provided with Ablator, is used

to specify the xy sub-domain(s) of a prospective experiment during the initialization phase, and these values are transparently used by the subsequent detection and ablation phases of the experiments.

*Software control of the laser-scanning microscope.* Ablator also controls the Zeiss LSM software to acquire images and perform laser ablations. This was achieved by using a GUI automation library from Python called *pywinauto* (<http://code.google.com/p/pywinauto/>). This library enables scripted control of the mouse, keyboard, and graphical components in separate software programs (i.e., the LSM software) on Windows computers. This approach provides a mechanism for broadly controlling proprietary devices, which may not provide easy software access for controlling their hardware.

### ***Detecting and lesioning neuron targets***

Experiments were carried out in three steps as described above (**Fig. 1.2**) by Ablator software. The following text summarizes the protocol details.

#### ***STEP 1: INITIALIZATION PHASE.***

With the experimenter manually controlling the robotic xy translation stage and focus, the specimen is maneuvered to situate the nucleus or region of interest in the center of the field of view under videomicroscopy and epifluorescence. The data-switch is in position 'B' for manual control of the xy translation stage (**Fig. 1.3**). Ablator software can accommodate a single uniform domain or a domain that consists of  $n$  isolated parts. For slice preparations that generate respiratory rhythm, the experimenter uses videomicroscopy and well-established neuroanatomical landmarks in the ventrolateral medulla (Ruangkittisakul et al. 2011) to locate one side of the preBötC. If  $\text{Ca}^{2+}$ -sensitive dyes are used, a 45 s time-series of  $\text{Ca}^{2+}$  fluorescence imaging is

acquired from the preBötC (unilaterally) under epifluorescence, and then analyzed to confirm that clustered fluorescent oscillations occur within the field of view. Once this first 'hot spot' is determined, the data-switch is changed to position 'A' (computer control of the xy translation stage) and a graphical user interface (GUI) in Ablator software is used to store the center position for this first part of the xy domain (Fig. A.1). After that, the GUI can be used to control the stage (from position 'A') to find and define other sub-regions of the xy domain. The center position for each sub-domain is similarly entered into the GUI and thus stored in memory. This process repeats  $n$  times for an xy domain consisting of  $n$  parts. In preBötC experiments, the xy domain bilateral.

The z-range for each part of the xy domain must also be specified. Confocal or two-photon imaging is used to determine the z-range rather than epifluorescence (as above), which was used to specify the xy domain boundaries. The slice is scanned using an excitation filter, dichroic mirror, and barrier filter as appropriate depending on the fluorophore as well as choice of excitation laser and detector (descanned versus non-descanned). The configuration is stored in the LSM software to be reused during the *detection phase*. Focus is set manually to the surface of the slice preparation, defined as  $z=0 \mu\text{m}$ . The depth (z-range) is stepped in user-defined increments, generally  $10 \mu\text{m}$ . The full z-range is defined for each part of the xy domain based on whether (and how many) fluorescent cells are detectable at depths  $\leq 100 \mu\text{m}$ . In practice the limit is generally  $\leq 100 \mu\text{m}$ . Thus limiting the z-range ensures that the automated cell-detection algorithm does not get stuck in a fruitless search for suitable targets at slice depths where fluorescent dyes and/or long-wavelength laser pulses cannot penetrate effectively. The limits of the z-range ascertained for each part of the xy domain are entered into an Ablator configuration file - `AblatorConfiguration.py` (see APPENDIX). The information regarding the xy

domain and z-range is stored so that robotics can translate the stage to positions 1 through  $n$  automatically and over their full respective z-ranges. For our application in preBötC, the z-range ascertained on both sides of the transverse slice is entered into **AblatorConfiguration.py** in the variables `POSITION_1_ZRANGE = [z1, z2]` and `POSITION_2_ZRANGE = [z3, z4]`, where  $z$  indicates confocal plane depth in  $\mu\text{m}$ . This information is stored in memory so that robotics can translate the stage to position 1 and 2 automatically.

A digital-to-analog connection is established from the master computer that runs the Ablator software to the robotic xy stage translators and microscope controllers as indicated above. The computer that acquires electrophysiology data is time-synced with the master computer to record real time network motor output. A user defined name, usually of the form `YYMMDDslice#lesion#` (e.g., `120908s1lesion1`), assigns a unique experiment identification that applies to files and directories for the experiment, which are automatically created to store the data on the master computer.

#### ***STEP 2: DETECTION PHASE.***

Neurons subject to the ablation protocols are detected on the basis of their static criteria, *i.e.*, the expression of genetically encoded fluorescent protein markers, or dynamic criteria, *i.e.*, patterns of rhythmic activity detectable via  $\text{Ca}^{2+}$  imaging.

The general algorithm for detecting targets is the same between both classes of experiments and starts with generating an image from the raw data that broadly captures features of the potential targets. Then, Ablator uses an iterative threshold-crossing algorithm to generate a list of ROIs that represent these targets. Finally, the software does post-processing validation and pruning of targets based on further criteria that depend on whether the targets are statically or dynamically detected.

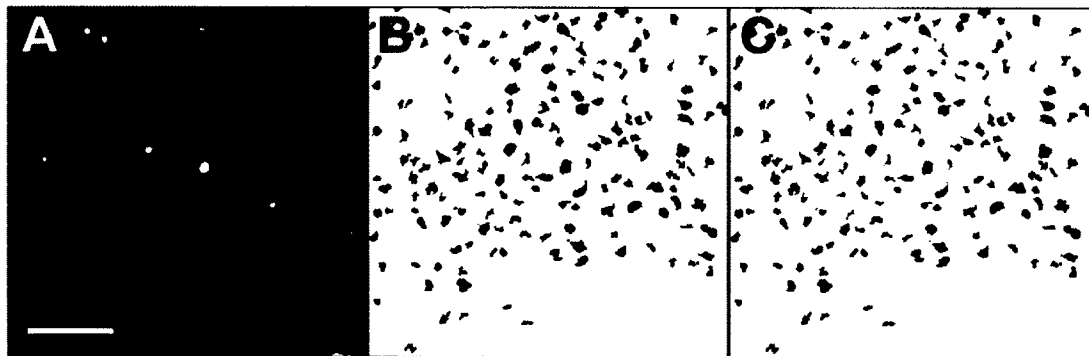


Image processing steps are repeated bilaterally for each increment of the z-axis, and the final map of targets is stored in memory.

*Detecting cells via fluorescent reporters.* Detecting targets based on static images using fluorescent reporters is the simplest case. Ablator acquires a relatively high-resolution (512 x 512) image at a given depth, which covers the entire field of view (420.84 x 420.84  $\mu\text{m}^2$ ). The choice of laser depends on the fluorescent protein. The Ti:sapphire laser with 800-960 nm excitation wavelength is effective for detection of GFP- and YFP-labeled cells (Wilson et al. 2007). However, for red reporters such as tdTomato (Madisen et al. 2010), which we favor for its brightness, a 543 nm Helium-Neon excitation laser is applied and an image is acquired via the descanned detector. After processing the raw image through noise reduction and contrast enhancement filters, **StaticImageAnalyzer.py** (see APPENDIX) routine in Ablator then calls the iterative threshold-crossing routine described below (see "*Iterative threshold-crossing algorithm and image processing*") to find a mask of local maxima representing all potential targets for that focal plane. After the mask of potential targets is determined, the post-processing step occurs (see "*Post-detection pruning of potential targets*").

*Detecting rhythmically active cells.* Bidirectional scans of the xy domain are performed with the Ti:sapphire laser wavelength set to 800 nm (optimal for green  $\text{Ca}^{2+}$  dyes) at ~25% power. **DynamicTargetDetector\_PrecalculatedTargets.py** (see APPENDIX) in Ablator package acquires a time series of images at 4 Hz (250 ms per frame) for 1 min. Each image is 256 x 256 pixels, which covers the entire domain 420.84 x 420.84  $\mu\text{m}^2$ . The stack of images is first processed by routine **DynamicImageAnalyzer.py** (see APPENDIX) through a series of filters using ImageJ as a software library: Gaussian-Blur, Despeckle, and Remove Outliers

operations are used to reduce noise. A temporal lag filter is applied to compute fluorescence changes ( $\Delta F = F - F_0$ ) normalized to baseline ( $F_0$ ), i.e.,  $\Delta F / F_0$ , which can be plotted as a function of time where  $F_0$  is fluorescence measurement 4 frames (1 s) prior to the current value. The temporal lag filter emphasizes periodic fluorescence changes that reflect synchronized respiratory cycles among preBötC cell targets. These rhythmic criteria are specific to our application in the preBötC, but could be similarly applied to experiments in mammalian central pattern generator model systems such as the lumbar spinal cord circuits for locomotion as well as oral-motor circuits in the vicinity of the trigeminal motor nucleus. The image stack is then projected into one single planar image by calculating the standard deviation (SD) of the fluorescence intensity at each pixel through the stack (Fig. 1.4A). From the SD image, a binary mask of local maxima is created by the iterative threshold-crossing algorithm described in the next subsection (Fig. 1.4B).



**Figure 1.4** Planar images pertaining to a  $\text{Ca}^{2+}$  acquisition stack. (A) Analyzed image shows standard deviation (SD) of fluorescence changes ( $\Delta F$ ) for a 1-min  $\text{Ca}^{2+}$  imaging time series. Full frame represents  $420.84 \times 420.84 \mu\text{m}$  field centered on the preBötC. Scale bar shows  $100 \mu\text{m}$ . (B) The mask of all potential targets where all ROIs are preliminary, i.e., based solely on SD, and not yet evaluated by frequency or threshold tests (see Fig. 1.7D-E). (C) Validated (red) and rejected (blue) cell targets after analyses.

*Iterative threshold-crossing algorithm and image processing.* Given an image that captures features of potential targets (obtained via a higher-resolution image of fluorescent protein reporter expression or  $\text{Ca}^{2+}$  imaging), the software uses the

'Analyze Particles' routine in ImageJ to select ROIs. The software detects particles using a pixel intensity threshold. It starts with a high value (near the maximum) and iteratively drops the threshold while accumulating particles (*i.e.*, target ROIs) within a certain range of areas specified within the Ablator configuration. At first, with a high threshold, few local maxima are detected and the mask is small and sparse with ROIs. The routine then lowers the threshold by a user-defined increment and re-analyzes the image. As threshold decreases in steps, more ROIs become detectable. These newly detected ROIs are added to the mask, which expands the list of potential targets. The threshold is decreased incrementally over a number of partitions determined by the quotient of 4096 values of fluorescence intensity (for a 12-bit image) divided by the user-defined increment (above). As the detection process continues and threshold decreases incrementally, the smaller ROIs from prior iterations – which are fully contained in larger ROIs from the current iteration – are discarded, and the new larger ROIs are retained. Conversely, if a newly detected ROI at the current iteration envelopes two or more ROIs from a prior iteration, then the newly detected 'superset' ROI is discarded and the multiple ROIs from the earlier iteration are retained. Thus the system avoids spuriously conflating two (or more) cells into a single target. After looping through all the partitions, the remaining set of ROIs is saved as the mask of potential target neurons for that focal plane (Fig. 1.4B).

As part of the threshold-crossing algorithm, Ablator preferentially selects ROIs based on their level of circularity. The software computes circularity score ( $C$ ) according to the formula  $C = 4\pi( a / p^2 )$ , where  $a$  is the area and  $p$  is the perimeter of an ROI. Area  $a$  and perimeter  $p$  are computed by ImageJ as part of the 'Analyze Particles' routine.  $C$  ranges from 0 to 1. Scores approaching 0 indicate an increasingly elongated polygon.  $C \sim 1$  indicates a perfect circle. If  $C$  falls below a user-

specified cut-off, the ROI is rejected from the potential target list. The appropriate C score depends on the characteristic morphology of the neurons of interest, and needs to be determined empirically on a case-by-case basis. In the preBötC, ROIs that indicate valid cell targets pass the circularity test with the default range [0.5, 1] when detected via Ca<sup>2+</sup>-imaging and [0.75, 1] for genetically encoded fluorescent reporters. We apply more stringent circularity criteria for static targets because of the ability of tdTomato to label cell bodies and neuropil (Madisen et al. 2010).

When using fluorescent reporters to identify cell targets, circularity is particularly useful in biasing target detection to somata rather than neuropil or auto-fluorescent detritus (Fig. 1.5A<sub>1</sub>,A<sub>2</sub>). Rejecting an isolated dendrite segment (e.g., Fig. 1.5B<sub>1</sub>,B<sub>2</sub>) avoids protracted lesion attempts during the ablation phase of the

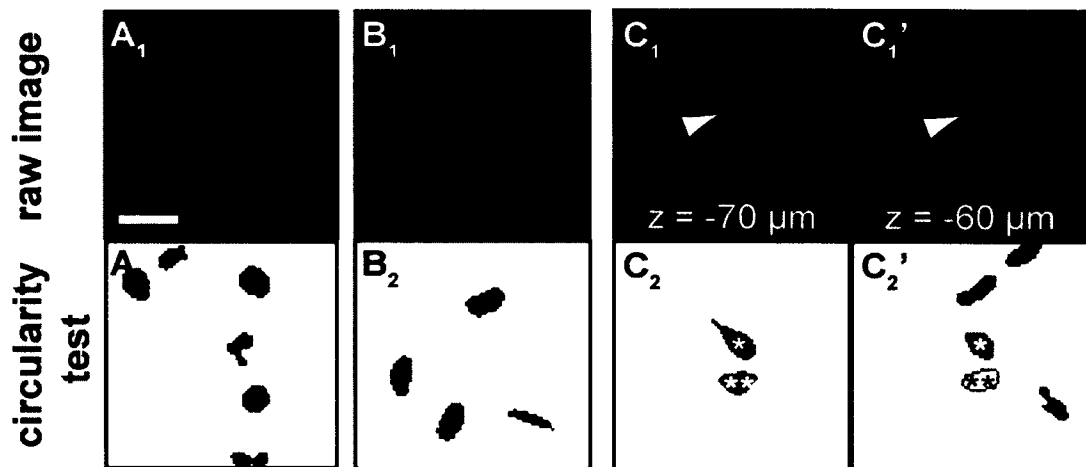


**Figure 1.5** Detecting cell targets via fluorescent reporters. Images in A<sub>1</sub>, B<sub>1</sub>, C<sub>1</sub> and C<sub>1</sub>' show preBötC neurons from *Dbx1<sup>CreERT2</sup>;Rosa26<sup>tdTomato</sup>* mice, in which *Dbx1*-derived neurons express tdTomato. Masks A<sub>2</sub>, B<sub>2</sub>, C<sub>2</sub> and C<sub>2</sub>' show ROIs obtained by analyzing the corresponding images above. Red ROIs are deemed valid targets by the circularity test; blue ROIs are rejected. Circularity analyses differentiate somata from auto-fluorescent detritus (A<sub>1</sub>,A<sub>2</sub>) as well as isolated pieces of dendrites (B<sub>1</sub>,B<sub>2</sub>). Non-somatic auto-fluorescence and isolated parts of dendrite are not valid targets, and thus are rejected. Circularity analysis furthermore rejects ROIs that include the soma plus an adjacent dendritic segment. A contiguous soma-dendrite ROI (C<sub>1</sub>, C<sub>2</sub> blue ROI \*) is rejected in the -70 μm focal plane, but the same cell is validated by circularity analysis at -60 μm (C<sub>1</sub>', C<sub>2</sub>' red ROI \*). In C<sub>1</sub>,C<sub>2</sub>, the red ROI \*\* is validated at -70 μm, but then is rejected by the priority rule at -60 μm (C<sub>1</sub>',C<sub>2</sub>' unfilled blue ROI \*\*). Rejected neuropil is also visible at -60 μm (C<sub>2</sub>' blue ROI).

experiment, which are problematic because the dendrite and its soma are redundant targets and attempting to laser-ablate the dendrite is more likely to sever the process (Kole 2011) rather than kill the neuron. Furthermore, circularity analysis can differentiate a target cell that is visible with a contiguous dendritic segment from the same cell in an adjacent plane where the dendrite is not visible. The neuron in (Fig. 1.5C<sub>1</sub> arrowhead) produces an ROI in the mask that fails the circularity test (Fig. 1.5C<sub>2</sub> \* blue ROI). Nonetheless, the same cell is detectable in an adjacent focal plane (Fig. 1.5C<sub>1</sub>', arrowhead) where its corresponding ROI does not include the dendrite and the cell passes the circularity test (Fig. 1.5C<sub>2</sub>', \* red ROI). Less stringent circularity criteria are, in practice, optimal for cell targets detected by Ca<sup>2+</sup>-imaging because detritus and non-oscillating targets are filtered out in the post-detection pruning step that relies on Fourier analysis (below).

*Post-Detection Pruning of Potential Targets.* For detecting static targets, the final step of processing (the priority rule) eliminates redundant targets from adjacent focal planes. A cell that is detected in more than one plane may pass the circularity test in more than one plane too. Overlaying ROIs within four consecutive focal planes are parsed such that the ROI from the earliest acquisition is retained and all others are deleted. Fig. 1.6A-D shows four adjacent focal planes and their corresponding masks. ROI 1 is detected at -80, -70, and -60 μm, yet is accepted as a valid target only at -80 μm. ROI 7 is first detected at -70 μm but fails the circularity test (Fig. 1.6B<sub>2</sub>), and then subsequently passes and is validated at -60 μm (Fig. 1.6C<sub>2</sub>). By the priority rule, ROI 7 is ignored at -50 μm (Fig. 1.6D<sub>2</sub>). As mentioned above, the cut-off for the circularity score can be adjusted to accept non-circular shapes according to a graded scale (e.g., for neurons that have pyramidal or fusiform somata).

## priority rule

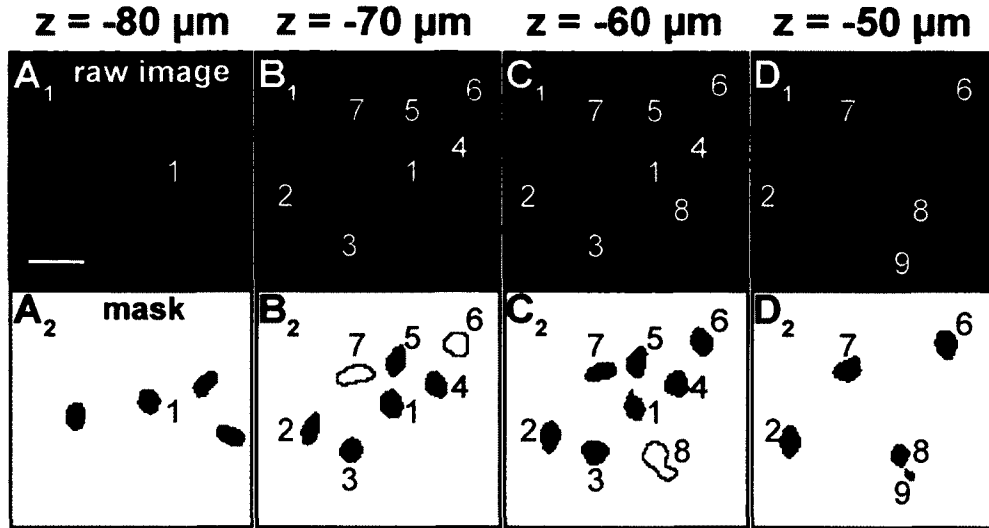


**Figure 1.6** The priority rule in target cell detection. (**A<sub>1</sub>-D<sub>1</sub>**) Images of *Dbx1*-derived neurons in four adjacent focal planes. ROIs are detected in more than one focal plane. (**A<sub>2</sub>-D<sub>2</sub>**) Masks of targets from **A<sub>1</sub>-D<sub>1</sub>**. The ROI from the deepest focal plane to pass the circularity test is validated and any subsequent overlaying ROIs (that may also pass the circularity test) are rejected. Red ROIs are validated and blue ROIs rejected by the priority rule. Unfilled ROIs (blue outline) are rejected by the circularity test. Scale bar shows 20  $\mu\text{m}$ .

For detecting rhythmically active targets, ablator evaluates each ROI identified by  $\text{Ca}^{2+}$  imaging based on dynamic fluorescence changes from the time series (**Fig. 1.7B<sub>1-5</sub>**). This subsequent layer of analysis, frequency domain analysis, unambiguously evaluates rhythmicity in putative inspiratory neurons. Ablator calls 'Plot Z Axis Profile' function in ImageJ to plot fluorescence changes  $\Delta F/F_0$  for each ROI, and then scripted routines in **DynamicImageAnalyzer.py** calculate a relative power spectrum density graph from each profile plot using Fourier analysis. The software searches for significant power at frequencies in the range of 0.15-0.5 Hz, which is typical for respiratory rhythm in slice preparations (Feldman et al. 2012; Smith et al. 1991; Smith et al. 1990). This range of frequencies is arbitrary and can be modified by the experimenter in setup settings routine **AblatorConfiguration.py**. A score is then evaluated based on the maximum peak power in the specified

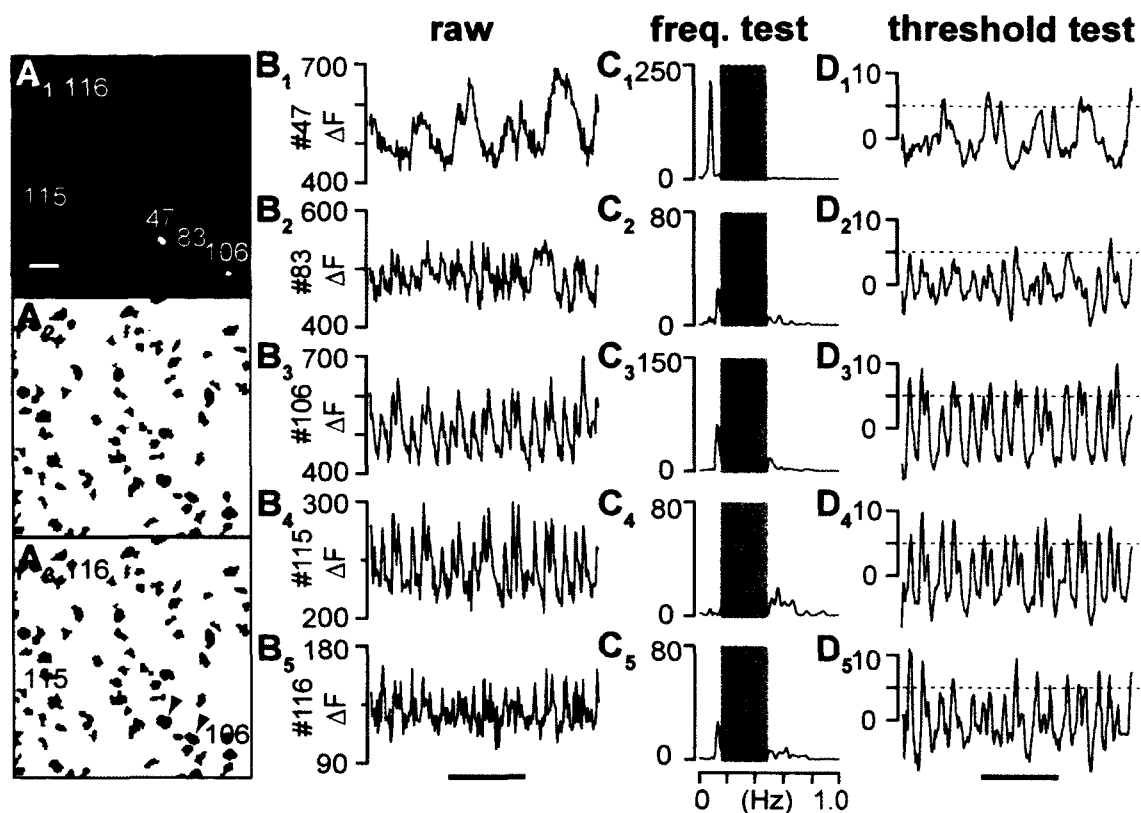


**Figure 1.7** Detecting cell targets via  $\text{Ca}^{2+}$  imaging. (**A**<sub>1-3</sub>) Analyzed image **A**<sub>1</sub> shows standard deviation (SD) of fluorescence changes ( $\Delta F$ ) for a 1-min  $\text{Ca}^{2+}$  imaging time series. Scale bar shows 20  $\mu\text{m}$ . **A**<sub>2</sub> shows the mask of all potential targets from **A**<sub>1</sub>; unevaluated ROIs are grey. **A**<sub>3</sub> shows the mask of validated (red) and rejected (blue) targets. (**B**<sub>1-5</sub>) Raw  $\Delta F$  activity is displayed for ROIs 47, 83, 106, 115, and 116 from **A**<sub>1</sub>. Scale bar shows 20 s. (**C**<sub>1-5</sub>) The frequency test analyzes power spectra computed from the time series in **B**<sub>1-5</sub>, showing peak power as a function of characteristic frequency. Frequency band for respiratory rhythm *in vitro* (0.15-0.5 Hz) is shown in gray. (**D**<sub>1-5</sub>) The threshold test counts the peaks in the normalized  $\Delta F$  time series that cross a user-defined level (dashed red line); scale bar shows 20 s. ROIs 106, 115, and 116 are deemed valid targets because each crosses the threshold five or more times per min. ROI 47 shows a large amplitude  $\Delta F$  signal (**B**<sub>1</sub>) with 5 threshold crossings (**D**<sub>1</sub>), but its dominant frequency is  $<0.15$  Hz so it is rejected (but displayed for pedagogical purposes). ROI 83 is rhythmically active in the expected frequency range (**C**<sub>2</sub>) but fails the threshold test and thus is deemed too weak, and is rejected.

frequency range. ROIs that score at least 50 (arbitrary units) are accepted and pass to the next level of evaluation. The remaining ROIs that score  $<50$  a.u. are discarded. The cut-off (50 a.u. in the present study) is adjustable and was empirically determined for application to the preBötC. **Figure 1.7C**<sub>1-5</sub> show power spectra for ROIs 47, 83, 106, 115, and 116. Peak power exceeds 50 a.u. in all cases, but ROI 47

is rejected because the peak frequency is lower than 0.15 Hz. The range of frequencies (here 0.15-0.5 Hz) is arbitrary and can be modified by the experimenter for alternative applications.

The last layer of analysis for ROIs detected via  $\text{Ca}^{2+}$  imaging is the peak count analysis. In this process, `DynamicImageAnalyzer.py` measures amplitude of  $\Delta F/F_0$  fluorescence peaks during the 1-min imaging bout for each ROI, then compares the peak amplitude values to a pre-adjusted amplitude threshold (pre-entered in setup settings routine `AblatorConfiguration.py`, also see APPENDIX for how to obtain the value for amplitude threshold) and counts the peaks that exceed the amplitude threshold. If the number of peaks exceeds the peak count threshold (5 in the present study, i.e. 5/min), then the ROI is deemed a legitimate respiratory neuron, i.e., a valid target (Fig. 1.7D<sub>1-5</sub>). Post-processing analysis is repeated for every ROI on the potential target list, to acquire cell targets with sufficiently high amplitude oscillations in the appropriate frequency range.

The software thus arrives at a final array of cell targets, in which many of the original ROIs have been rejected (Fig. 1.4C, 1.7A<sub>3</sub>). The criteria above are arbitrary parameters that can be modified to accommodate different experimental applications; the preBötC is just one model system. The nature and age of the tissue specimen, laser strength, choice of indicator dye, and other factors can influence the amplitude and frequency of network oscillations so Ablator is adjustable.

To corroborate the quality of automated dynamic target detection routine we performed whole-cell patch-clamp recordings from cell targets that passed the analyses of  $\Delta F/F_0$  activity (Fig. 1.8), which all showed robust respiratory activity (n=3).



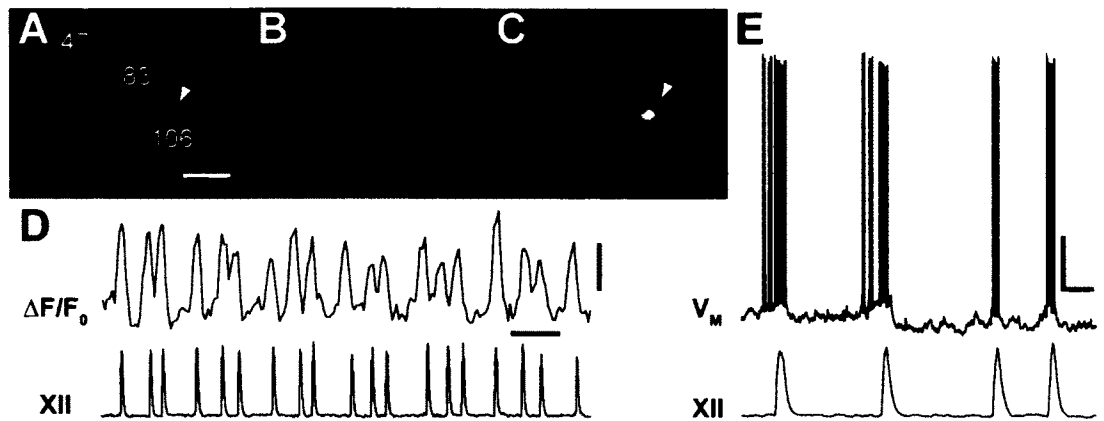


**Figure 1.8** Whole-cell recording from the preBötC neuron that was first identified as ROI 106 in Fig. 1.7 (see panels A<sub>1</sub>, B<sub>3</sub>, C<sub>3</sub>, D<sub>3</sub>). (A) SD Image showing Ca<sup>2+</sup> fluorescence with superimposed ROI labels. Scale bar shows 20 μm. (B) Same neuron as A filled with Alexa 568 through the patch pipette. (C) Merged image from A and B. (D)  $\Delta F/F_0$  from ROI 106 displayed with XII output. Vertical calibration reflects 10%  $\Delta F/F_0$ . Time calibration bar shows 5 s. (E) Intracellular recording (whole-cell) plotted with XII output. Voltage calibration shows 20 mV, time calibration shows 1 s.

### **STEP 3: ABLATION PHASE.**

Order of target selection. Target selection is random by default, drawn from the 3D volume of detected neurons (or glia), but any criterion can be used. For example, targets can be preferentially selected based on proximity to the centroid of the collection of targets. Depending on the experimental preparation, centroid selections may be drawn from one continuous volume or from any one of  $n$  sub-domains. Targets can also be preferentially drawn based on magnitude of the fluorescent signal so that the most rhythmically active, or brightest cells are ablated first. Arbitrary sequences are also acceptable; the user just uploads a text document that specifies the order.

When the xy domain consists of two or more sub-domains, a specified number of target selections may be made within a sub-domain before moving to another; the default is one. The strategy of left-right alternation will be relevant to a variety of slice models cut in the transverse or frontal planes, which preserve bilateral

symmetry. The respiratory circuits including the preBötC are a useful example of such a system from the brainstem. In practice, an alternation strategy would apply to any bilaterally distributed network or any domain with  $n$  sub-regions. It is advantageous to batch-lesion 50 or 100 targets per side before alternating. This minimizes long-distance translations of the xy specimen stage, which due to mechanical lash, can cause disparity between the internally stored map of targets and their actual locations. More significantly, translations also increase the time between lesions dramatically.

*Laser ablation.* The Ti:sapphire laser is tuned to 800 nm, focused on the target ROI in a planar scan mode but with maximum optical zoom (10.52  $\mu\text{m}$  x 10.52  $\mu\text{m}$  region), and then scanned at maximum intensity through a narrow band of wavelengths (560-615 nm) until the software deems it vaporized. **AblatorUtils.py** (see APPENDIX) confirms the lesion by analyzing the image acquired during the full-intensity scan. Emission within this range detects light scattering due to vaporized tissue (i.e., a cavity in the tissue now filled with water vapor), while excluding green dyes (e.g., fluorescein, Fluo-8 AM, etc...) as well as infrared wavelength reflections from the laser (Fig. 1.9A). **AblatorUtils.py** measures the brightness (maximum gray value) of water vapor autofluorescence at the target location. Maximum gray value can take any value from 0 to 4095 for a 12-bit image. The threshold to pass this maximum-gray-value test is for any pixel to exceed 2000, which is an adjustable setting defined by the user in **AblatorConfiguration.py**. We find empirically that 2000 is a good default setting; in successful lesions 5-40% of all pixels pass the test. In failed lesions 0 pixels pass this threshold; the maximum gray value generally measures less than 500 in failed lesions. Therefore, the criteria that distinguish successful and failed lesions are distinct and false positives (i.e., false lesion confirmations) are unlikely.

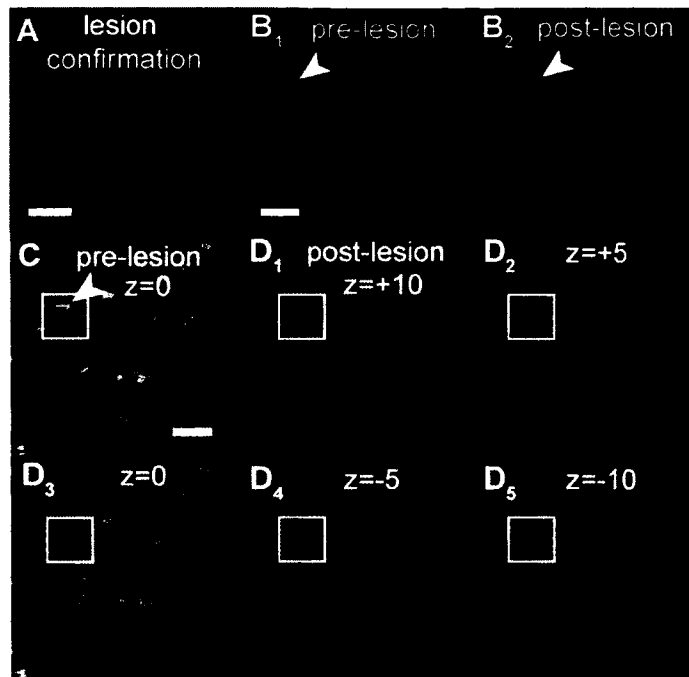


**Figure 1.9** Laser ablation and confirmation. (A) Image acquired in the band 560-615 nm during maximum-intensity spot scanning for cell destruction. Scale bar shows 2  $\mu\text{m}$ . (B<sub>1-2</sub>) Images of Fluo-8 AM-labeled preBötC neurons before (B<sub>1</sub>) and after (B<sub>2</sub>) a single-cell laser ablation. The target cell (arrowhead) is visible pre-lesion but not in the post-lesion image. Neighboring (un-lesioned) cells are present in both images. Scale bar showing 10  $\mu\text{m}$  applies to all images in B-D. (C, D<sub>1-5</sub>) Infrared-enhanced differential interference contrast images of the target cell (white box) prior to (C), and after (D<sub>1-5</sub>) laser lesion. Arrowhead in C matches B as a reference for target cell position. The focal plane (C) is normalized to  $z=0$   $\mu\text{m}$  for relative comparisons with panels D<sub>1-5</sub>, which show 5- $\mu\text{m}$  increments above and below the target cell.

Nevertheless, un-lesioned tdTomato-labeled cell targets should be detectable in the band 560-615 nm too, which would make lesion confirmation with tdTomato reporters untenable. However, in practice, 800-nm laser pulses are not optimal for tdTomato excitation, so the fluorophore does not emit significantly during lesion attempts. Moreover, choosing a sufficiently high threshold ensures that only vaporized cell targets – and not a small degree of fluorescence from un-lesioned tdTomato-labeled cells – result in lesion confirmation.

Ablated cell targets vanish from the fluorescence images, providing an intuitive form of confirmation (Fig. 1.9B<sub>1-2</sub>). Differential interference contrast imaging

shows that in successful lesions, a pockmark replaces the original cell image (Fig. 1.9C,D<sub>3</sub>). The cavity resulting from the lesion is limited to the borders of the cell and occupies less than 10  $\mu\text{m}$  in the z-axis, demonstrating that the volume of damage is limited to the target ROI (Fig. 1.9D<sub>1-6</sub>). Confirmed lesions are added to the tally. In the case of a failure to confirm a lesion, the target selection algorithm does not advance and another attempt is made to lesion the ROI. The scanning speed is decreased by one (initial scanning speed is five in LSM software, *i.e.*, 1.95 s, reducing the scanning speed by one in LSM software indicates the scanning time is approximately doubled) to increase the likelihood of lesioning the target. If the lesion is now confirmed, the system moves on to select a new target. If not, a third attempt to lesion the target is initiated. The scanning speed in the third attempt is further decreased beyond the second attempt. The lesion attempts can be repeated a user-defined number of times before the ROI is finally deemed a failed lesion. For applications to the preBötC, the default maximum number of attempts was set to three. In practice, increasing the number of lesion attempts increases the percentage of successful lesions per number of detected targets. However, since the duration of the scan increase geometrically with each lesion attempt, the exhaustive approach to each lesion, which can involve five (or more) attempts per target ROI, can be prohibitively time-consuming.

Failed lesions do not contribute to the tally and their ROIs are removed from the list of targets to avoid re-selection for the remainder of the experiment. The software writes a log file that documents the progress of the experiment and lists all lesions by index number and time of confirmation of ablation. Therefore, the status of network activity and the XII rhythm can be explicitly tracked in time with lesion tally. Therefore, network function can be explicitly tracked in real time with lesion tally. The software images the full field of targets after a user-defined number of lesions, which

is generally set to a default of ten in the setup settings routine `AblatorConfiguration.py`. Selection and ablation are repeated iteratively until all targets are exhausted (Fig. 1.2). Alternatively, the experimenter can simply terminate the program at any time.

### 1.3. Results

Figure 1.10A illustrates a typical 400- $\mu\text{m}$ -thick slice in which green-shaded regions indicate the xy domain of the preBötC and a z-axis depth of 80  $\mu\text{m}$ , which is typical for experiments that employ  $\text{Ca}^{2+}$  indicator dye in the preBötC (Hayes et al. 2012; Ruangkittisakul et al. 2009). The slice also retains oligosynaptic premotor circuits and hypoglossal (XII) motor neurons (Koizumi et al. 2008). Respiratory motor output is measured via the XII cranial nerve rootlets (Fig. 1.10A). The xy domain is stored in memory so that the robotics can position the specimen appropriately during the detection and ablation phases.

The general strategy for target detection is to acquire and analyze images of an xy domain at focal planes separated by 10- $\mu\text{m}$  increments in the z-axis (Fig. 1.10A). For  $\text{Ca}^{2+}$ -imaging experiments, the system acquires time-series images. The stack is projected into one plane by calculating the standard deviation of the fluorescence intensity at each pixel through the stack (Fig. 1.4A, 1.7A<sub>1</sub>). Regions of interest (ROIs) with large fluorescence changes stand out (e.g., 47, 83, 106, 115, 116, Fig. 1.7A<sub>1</sub>), which is used to produce a mask of potential targets (Fig. 1.4B, 1.7A<sub>2</sub>). Ablator finds local maxima via the iterative threshold-crossing routine (see **Methods**) and defines them as ROIs. Each ROI is then further analyzed through the frequency domain test (Fig. 1.7B<sub>1-5</sub>, C<sub>1-5</sub>) and amplitude threshold test (Fig. 1.7D<sub>1-5</sub>), only ROIs pass both tests are accepted as *bona fide* respiratory neurons (Fig. 1.4C, 1.7A<sub>3</sub>). Thus, Ablator identifies cell targets with sufficiently high amplitude oscillations

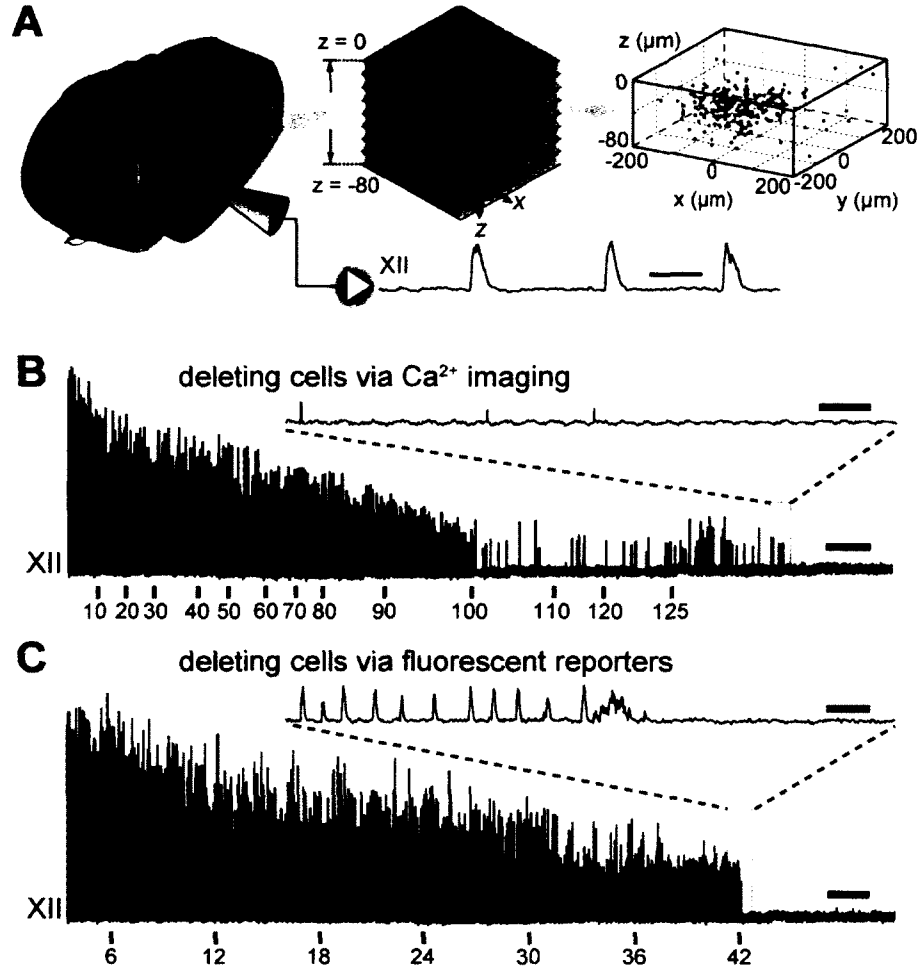


**Figure 1.10** Automated cell target detection and ablation in the preBötC. **(A)** Rhythmically active slice preparation containing the preBötC as well as premotor neurons and XII motoneurons. Spontaneous breathing-related motor output is measurable via suction electrode recordings from the XII nerve root. Scale bar shows 1 s. Green boxes demarcate the bilaterally distributed xy domain of the preBötC. Image stacks (middle) show 1-min acquisitions using  $\text{Ca}^{2+}$  indicator dye over the domain of the right half of the preBötC. Each time series is repeated in 10- $\mu\text{m}$  increments from the surface of the tissue to a final depth of 80  $\mu\text{m}$  in the z-axis. The 3D map (right) shows all validated cell targets for the right half of the preBötC. Validated cell targets are colored red, as also shown in a single focal plane in **Fig. 1.4C, 1.7A<sub>3</sub>**. **(B)** Serial destruction of preBötC neurons detected via  $\text{Ca}^{2+}$  imaging. The abscissa is a timeline; its scale bar shows 5 min. The last 2 min of XII motor output are highlighted by a grey box and then expanded above (scale bar shows 10 s). In the main display and the inset, the ordinate plots XII amplitude (a.u.). Numbered ticks (bottom) represent the tally of single-cell ablations; each lesion was confirmed according to criteria shown in **Fig. 1.9**. **(C)** Serial destruction of  $\text{Dbx1}^+$  neurons detected via reporter expression in  $\text{Dbx1}^{\text{LacZ}}$  knock-in mice. Display conventions match panel **B** except for scale bars, which represent 2 min in the main display and 3 s in the inset (above). For **B** and **C** the recording trace is no longer displayed after 12 min of XII quiescence, although the XII output was monitored for 30-60 additional min to verify rhythm cessation.

in the appropriate frequency range.

Cells that express genetically encoded reporters (e.g., GFP, YFP, tdTomato) can also be automatically detected. Ablator acquires a higher-resolution image and then calls the iterative threshold-crossing routine to find ROIs that represent all potential targets for the focal plane. Then the circularity test is applied to distinguish cell bodies from auto-fluorescent debris (Fig. 1.5A<sub>1-2</sub>) and isolated segments of dendrites whose somata are detected in an adjacent plane and retained as a valid target (Fig. 1.5B<sub>1-2</sub>, C<sub>1-2</sub>, C<sub>1'</sub>, C<sub>2'</sub>). A priority rule applied in the final stage eliminates redundant targets from adjacent planes. If two or more overlaying ROIs pass the circularity test, then the ROI from the earliest acquisition is retained and all others are rejected (Fig. 1.5C<sub>2</sub>, C<sub>2'</sub>, Fig. 1.6).

Every ROI in the xy domain, throughout the z-axis, is analyzed and the final target list is passed to the *ablation phase*, which begins as individual targets are drawn from the 3D volume (Fig. 1.10A). Selection is random by default and left-right alternation applies to preparations that preserve bilateral symmetry. The Ti:sapphire laser, tuned to 800 nm, is focused on one target. Maximum intensity scanning over a 110- $\mu\text{m}^2$  spot centered on the ROI is performed while acquiring an image with a 560-615 nm band-pass filter. Confirmation of ablation is obtained by applying a threshold-crossing algorithm to analyze the image in this range of wavelengths, which detects presumed water vapor in the cell cavity, while excluding green emissions of Ca<sup>2+</sup>-indicator dyes or YFP, as well as infrared reflections of the long-wavelength laser (Fig. 1.9). Following lesion confirmation, Ablator chooses a new target and re-starts the lesion process, which is repeated in a loop until all the targets are exhausted (Fig. 1.2).

We routinely detect up to hundreds of targets per experiment in the preBötC. Because laser ablation and confirmation requires 2-16 s per cell, the entire target list can be exhausted in <1 hr. The preBötC reliably generates robust motor output at ~0.2 Hz in slices for many hours (Feldman et al. 2012; Smith et al. 1991; Ruangkittisakul et al. 2006). The straightforward result of cumulative cell-specific laser ablations is that respiratory frequency and motor output both decline, and ultimately rhythm stops altogether. This fundamental result is obtained whether cell targets are detected via  $\text{Ca}^{2+}$  imaging (Fig. 1.10B) or via fluorescent reporters (Fig. 1.10C). Cumulative single-cell ablations ostensibly disassemble the rhythmogenic core of the preBötC, which is evident by the degradation of network activity (Fig. 1.10B,C, Hayes et al. 2012).

#### **1.4. Discussion**

Lesion techniques can interrogate the cellular bases of network function and dysfunction. The usefulness of any lesion method depends on three key factors: selectivity, accuracy, and monitoring sensitivity. Ideally, one differentiates a class of neurons from its neighbors and then selectively targets its constituents for ablation, while minimizing collateral damage. Finally, one monitors the effect of each lesion on network output so that the level of functionality, or loss of function, can be directly attributed to the corresponding set of deleted cell targets.

Conventional lesion techniques suffer limitations in one or more categories above. Electrolytic and excitotoxic lesions are crude techniques, seldom used, that lack anatomical precision and damage cells and axons of passage in the target area. Transgenic and knockout mouse models have been generated that can eliminate, silence, or poison specific cell classes. Limiting these effects to localized neural populations, however, has proven extremely difficult except in rare cases (Ray et al.



2011). Viral transfection methods offer the specificity of destroying or transiently silencing particular cell types, and can be injected into specific nuclei, but like transgenic and knockout approaches, cell classes are removed wholesale rather than piecewise (Lechner et al. 2002; Tan et al. 2008), which precludes tracking the behavioral consequences in parallel with the extent of the lesion.

In our approach, cell targets are vetted by well-defined criteria codified as *static target detection* (Figs. 1.5,1.6) and *dynamic target detection* (Fig. 1.7) routines in Ablator software (see **Methods**). If fluorescent reporter protein expression is too low, or the signal-to-noise ratio of  $\text{Ca}^{2+}$  imaging is insufficient, then the system may overlook valid targets. Additionally, for static targets, circles are judged to be better targets than elongated polygons. This criterion will not be universally applicable, so the cut-off for the circularity score can be adjusted to accept non-circular shapes according to a graded scale. Importantly, the algorithm (open-source Python code) can be user-modified to optimize the selection of any quantifiable feature of morphology. Rhythmic frequency is the signature feature of dynamic target detection, which applies to central pattern generator networks, but may not be appropriate for non-rhythmogenic systems. Nevertheless, the dynamic target detection algorithm can be modified to detect any measurable feature in a time series (e.g., latency, peak response time, etc.).  $\text{Ca}^{2+}$  imaging experiments in the preBötC assume that rhythmic fluorescence changes reflect neuronal activity (Frermann et al. 1999; Ballanyi & Ruangkittisakul 2009; Bobocea et al. 2010; Koshiya & Smith 1999). However, an important caveat is that rhythmicity may not always differentiate neurons from glia, as is the case in the preBötC where rhythmogenic neurons and astrocytes may oscillate with commensurate frequency (Okada et al. 2012). In some cases the software may detect astrocytes rather than neurons. Nevertheless, whole-cell

recordings demonstrate that fast  $\text{Ca}^{2+}$  transients identify respiratory neurons in the majority of cases (Del Negro et al. 2011).

With the increasing availability of mouse models featuring cell-specific expression of Cre recombinase and bright Cre-dependent reporters, it is realistic to detect the target class of neurons in more than one way. For example, rhythm-generating preBötC neurons can be detected in *Dbx1<sup>CreERT2</sup>* mice coupled with EYFP or tdTomato reporters, as well as rhythmic  $\text{Ca}^{2+}$  transients in register with XII output.

For lesion accuracy, the present approach requires that the map of targets exactly captures the physical cell locations, however, these two factors can become progressively uncorrelated during an experiment. A mismatch between the map of targets and the actual target positions results from mechanical lash in the translation stage, or because of tissue deformation over time. In either case, the disparity between the map and actual target locations must be rectified by stopping the ablation phase and restarting the acquisition phase (Fig. 1.2). An error of this type can be avoided by: 1) minimizing the number of xy translations during an experiment, and 2) providing 30-60 min of 'settling in' time in which the preparation resides, with perfusion, in the specimen chamber, before starting the detection phase of the experiment.

Ablations are produced by two-photon excitation, which depends on photon density squared and confines excitation to an ellipsoid volume at the focal point where two (or more) coincident low-energy photons converge. Long-wavelength single photons outside the focal point do not damage the tissue (Rubart 2004; So 2002; Svoboda & Yasuda 2006). Thus, cell targets can be vaporized while

neighboring neurons, glia, and axons of passage remain unharmed (Hayes et al. 2012).

The most significant limitation with respect to selectivity and accuracy pertains to laser pulses in tissue at depth. Ti:sapphire lasers can penetrate up to 900  $\mu\text{m}$  in mouse tissue (Svoboda & Yasuda 2006). However, in our experience 32 mW pulses (measured through the objective at the specimen stage from 800 nm, maximum intensity excitation) are rarely effective for detection and ablation deeper than 100  $\mu\text{m}$ . We routinely limit the depth to 80  $\mu\text{m}$  because the inherent limitations can cause too many false negatives in the detection phase and in the ablation phase too many failed lesions at depths exceeding 80  $\mu\text{m}$ .

With regard to monitoring sensitivity, a particular advantage of the present method is its ability to continuously measure network output while performing laser ablations in random or user-defined sequences. This advantage is not entirely new. Cell-specific laser lesions can be performed in sequence with physiological monitoring in larval zebrafish and *C. elegans*, where individual neurons are hand-targeted by an experimenter with prior knowledge of the system and its neuroanatomy (Bargmann & Avery 1995; Eklof-Ljunggren et al. 2012; Liu et al. 1999). However, our approach is practical for mammalian models where the organism is not transparent, cell targets are more abundant, and aside from general neuroanatomical guidelines, the specific map of targets is unknown beforehand. The present method does not require *a priori* knowledge of target cell locations; the map of targets is generated online during the experiment.

The present laser detection and ablation system can address the structure-function relationship of a neural circuit and may provide a model of neurodegenerative disease. Neurodegeneration *in vivo* takes place on various time

scales from hours to weeks, months, or years (depending on disease type and its etiology) and may involve long-term pathological changes to cells and their connectivity. In contrast, the present method is limited to abbreviated time window on the order of minutes to hours (depending on the number of cell targets and the normal viability of the preparation), which precludes many forms of plasticity and compensatory changes in the network structure. Therefore, the present approach could allow investigators to isolate the effects of progressive neuronal death in a simple *in vitro* (or *in situ*) model of a disease, which could be a useful complement to *in vivo* animal models of neurodegenerative disorders.

The integrated instrument system we present is economically feasible. It consists of executive software in the public domain that harnesses a Ti:sapphire laser, laser-scanning microscope, and electrophysiology instruments. These tools are widely available in universities, research institutes, and medical schools where neuroscience is a key research focus. Given a well-equipped core facility, the present technique can be implemented cost effectively by acquiring or fabricating a robotic translation stage. Moreover, implementing the present technique does not irreversibly modify an existing imaging setup. If Ablator software is offline, conventional imaging applications are not affected and the robotic translation stage can be controlled manually.

## 1.5. References

**Ballanyi K, Ruangkittisakul A (2009)** Structure-function analysis of rhythmogenic inspiratory pre-Bötzinger complex networks in "calibrated" newborn rat brainstem slices. *Respir Physiol Neurobiol* 168:158-178.

**Bargmann C, Avery L (1995)** Laser killing of cells in *Caenorhabditis elegans*. In: *Caenorhabditis elegans: modern biological analysis of an organism*, vol. 48 (Epstein, H. and Shakes, D., eds), pp 225-250 Amsterdam: Elsevier.

**Bobocea N, Ruangkittisakul A, Ballanyi K (2010)** Multiphoton/confocal Ca<sup>2+</sup>-imaging of inspiratory pre-Bötzinger complex neurons at the rostral or caudal surface of newborn rat brainstem slices. *Adv Exp Med Biol* 669:81-85.

**Bouvier J, Thoby-Brisson M, Renier N, Dubreuil V, Ericson J, Champagnat J, Pierani A, Chedotal A, Fortin G (2010)** Hindbrain interneurons and axon guidance signaling critical for breathing. *Nat Neurosci* 13:1066-1074.

**Del Negro CA, Hayes JA, Rekling JC (2011)** Dendritic Calcium Activity Precedes Inspiratory Bursts in preBötzinger Complex Neurons. *J Neurosci* 31:1017-1022.

**Eklof-Ljunggren E, Haupt S, Ausborn J, Dehnisch I, Uhlen P, Higashijima S, El Manira A (2012)** Origin of excitation underlying locomotion in the spinal circuit of zebrafish. *Proceedings of the National Academy of Sciences of the United States of America* 109:5511-5516.

**Feldman JL, Del Negro CA, Gray PA (2012)** Understanding the rhythm of breathing: so near yet so far. *Annu Rev Physiol* in press.

**Frermann D, Keller BU, Richter DW (1999)** Calcium oscillations in rhythmically active respiratory neurones in the brainstem of the mouse. *J Physiol* 515 ( Pt 1): 119-131.

**Gray PA, Hayes JA, Ling GY, Llona I, Tupal S, Picardo MC, Ross SE, Hirata T, Corbin JG, Eugenin J, Del Negro CA (2010)** Developmental origin of preBötzinger complex respiratory neurons. *J Neurosci* 30:14883-14895.

**Hayes JA, Wang X, Del Negro CA (2012)** Cumulative lesioning of respiratory interneurons disrupts and precludes motor rhythms in vitro. *Proceedings of the National Academy of Sciences of the United States of America* 109(21): p. 8286-91.

**Hirata T, Li P, Lanuza GM, Cocas LA, Huntsman MM, Corbin JG (2009)** Identification of distinct telencephalic progenitor pools for neuronal diversity in the amygdala. *Nat Neurosci* 12:141-149.

**Koizumi H, Wilson CG, Wong S, Yamanishi T, Koshiya N, Smith JC (2008)** Functional imaging, spatial reconstruction, and biophysical analysis of a respiratory motor circuit isolated in vitro. *J Neurosci* 28:2353-2365.

**Kole MH (2011)** First node of Ranvier facilitates high-frequency burst encoding. *Neuron* 71:671-682.

**Koshiya N, Smith JC (1999)** Neuronal pacemaker for breathing visualized in vitro. *Nature* 400:360-363.

**Lanuza GM, Gosgnach S, Pierani A, Jessell TM, Goulding M (2004)** Genetic identification of spinal interneurons that coordinate left-right locomotor activity necessary for walking movements. *Neuron* 42:375-386.

**Lechner, H. A., Lein, E. S. & Callaway, E. M. (2002)** A genetic method for selective and quickly reversible silencing of Mammalian neurons. *J Neurosci* 22, 5287-5290.

**Liu KS, Fetcho JR (1999)** Laser ablations reveal functional relationships of segmental hindbrain neurons in zebrafish. *Neuron* 23:325-335.

**Madisen L, Zwingman TA, Sunkin SM, Oh SW, Zariwala HA, Gu H, Ng LL, Palmiter RD, Hawrylycz MJ, Jones AR, Lein ES, Zeng H (2010)** A robust and high-throughput Cre reporting and characterization system for the whole mouse brain. *Nat Neurosci* 13:133-140.

**Okada Y, Sasaki T, Oku Y, Takahashi N, Seki M, Ujita S, Tanaka KF, Matsuki N, Ikegaya Y (2012)** Preinspiratory calcium rise in putative pre-Bötzinger complex astrocytes. *J Physiol*.

**Pierani A, Moran-Rivard L, Sunshine MJ, Littman DR, Goulding M, Jessell TM (2001)** Control of interneuron fate in the developing spinal cord by the progenitor homeodomain protein Dbx1. *Neuron* 29:367-384.

**Ray RS, Corcoran AE, Brust RD, Kim JC, Richerson GB, Nattie E, Dymecki SM (2011)** Impaired respiratory and body temperature control upon acute serotonergic neuron inhibition. *Science* 333, 637-642.

**Ruangkittisakul A, Panaitescu B, Ballanyi K (2011)** K<sup>+</sup> and Ca<sup>2+</sup> dependence of inspiratory-related rhythm in novel "calibrated" mouse brainstem slices. *Respir Physiol Neurobiol* 175:37-48.

**Ruangkittisakul A, Schwarzacher SW, Secchia L, Poon BY, Ma Y, Funk GD, Ballanyi K (2006)** High sensitivity to neuromodulator-activated signaling pathways at

physiological  $[K^+]$  of confocally imaged respiratory center neurons in on-line-calibrated newborn rat brainstem slices. *J Neurosci* 26:11870-11880.

Rubart M (2004) Two-photon microscopy of cells and tissue. *Circ Res* 95:1154-1166.

Smith JC, Ellenberger HH, Ballanyi K, Richter DW, Feldman JL (1991) Pre-Bötzinger complex: a brainstem region that may generate respiratory rhythm in mammals. *Science* 254:726-729.

Smith JC, Greer JJ, Liu GS, Feldman JL (1990) Neural mechanisms generating respiratory pattern in mammalian brain stem-spinal cord in vitro. I. Spatiotemporal patterns of motor and medullary neuron activity. *J Neurophysiol* 64:1149-1169.

So PTC (2002) *Encyclopedia of Life Sciences*. vol. 21-32.

Svoboda K, Yasuda R (2006) Principles of two-photon excitation microscopy and its applications to neuroscience. *Neuron* 50:823-839.

Tan W, Janczewski WA, Yang P, Shao XM, Callaway EM, Feldman JL (2008) Silencing preBötzinger complex somatostatin-expressing neurons induces persistent apnea in awake rat. *Nature Neuroscience* 11:538-540.

Wilson JM, Dombek DA, Diaz-Rios M, Harris-Warrick RM, Brownstone RM (2007) Two-photon calcium imaging of network activity in XFP-expressing neurons in the mouse. *J Neurophysiol* 97:3118-3125.



## **CHAPTER 2. Cumulative lesioning of functionally identified respiratory interneurons disrupts and precludes motor rhythms *in vitro***

### **2.1. Introduction**

CPG networks produce coordinated motor patterns that underlie behaviors such as breathing, locomotion, and chewing (Grillner 2006; Kiehn 2011). A key issue is not just which cell types generate these patterns of activity, but how many? This question pertains to whether and how cumulative cell loss will impair, and possibly preclude, behaviorally relevant network function.

Breathing consists of inspiratory and expiratory phases and preBötC putatively contains the respiratory CPG (Feldman & Del Negro 2006; Smith et al. 1991). Over several days *in vivo*, saporin-mediated destruction of preBötC neurons that express neurokinin-1 receptors (NK1Rs) causes sleep-disordered breathing and fatal respiratory pathology (Gray et al. 2001; McKay et al. 2005). Similarly, acute cell-silencing of a subset of the same NK1R-expressing population of preBötC neurons stops spontaneous breathing in awake adult rats (Tan et al. 2008). These studies helped to determine the cellular composition of the preBötC and confirmed that it was essential for breathing in an otherwise intact animal, but could not measure the resiliency of the preBötC when faced with silencing or deleting its core piecewise.

We examined this issue using slice preparations that capture the preBötC and spontaneously generate fictive breathing-related activity *in vitro*. These slices contain rhythm-generating interneurons, premotor neurons, as well as motoneurons and motor-nerves (Janczewski & Feldman 2006). The rhythmogenic core can be exposed at the slice surface (Ruangkittisakul et al. 2011). We applied the lesion

system described in **Chapter 1** to the perinatal mouse preBötC to test the hypothesis that piecewise destruction of the CPG core would cause graded loss of motor activity up to rhythm cessation. We surmised that this would occur principally via changes in cycle period. However, we observed two main effects. The cumulative deletion of preBötC interneurons diminished the amplitude of respiratory motor output and caused an increase in the cycle period that led inexorably to rhythm cessation. This suggests that the preBötC neurons coordinate both the periodicity as well as the strength of drive to premotor circuits. Our measurements provide an upper limit for tolerance to cell destruction in a mammalian CPG that serves a key physiological function.

## **2.2. Methods**

The Institutional Animal Care and Use Committee at The College of William & Mary approved these protocols. Neonatal mice aged postnatal days 0-3 (P0-3) were anesthetized and dissected in ACSF containing (in mM): 124 NaCl, 3 KCl, 1.5 CaCl<sub>2</sub>, 1 MgSO<sub>4</sub>, 25 NaHCO<sub>3</sub>, 0.5 NaH<sub>2</sub>PO<sub>4</sub>, and 30 D-glucose, equilibrated with 95% O<sub>2</sub> and 5% CO<sub>2</sub> (pH=7.4). Transverse slice preparations (450-500 μm) containing the preBötC were loaded with 36 μM Quest Fluo-8 AM (AAT Bioquest, Sunnyvale, CA) and perfused with 27°C ACSF at 4 ml/min. The external K<sup>+</sup> concentration in the ACSF was raised to 9 mM and inspiratory motor output was recorded from XII nerve roots. Picrotoxin and strychnine (5 μM) were added to the ACSF prior to the start of the experiments. Imaging and ablations were performed using a laser-scanning microscope (Zeiss LSM 510, Thornwood, NY) and a Ti:sapphire laser (Spectra Physics, Irvine, CA).

We cut 450-500- $\mu$ m-thick slices from the medulla and implemented two cutting strategies to prepare transverse slices that both retain the preBötC and expose inspiratory-modulated neurons at the slice surface.

The geometry of the first slice type exposed the preBötC at its rostral face (i.e., a preBötC-surface slice, Fig. 2.1). In these slices, the rostral boundary was

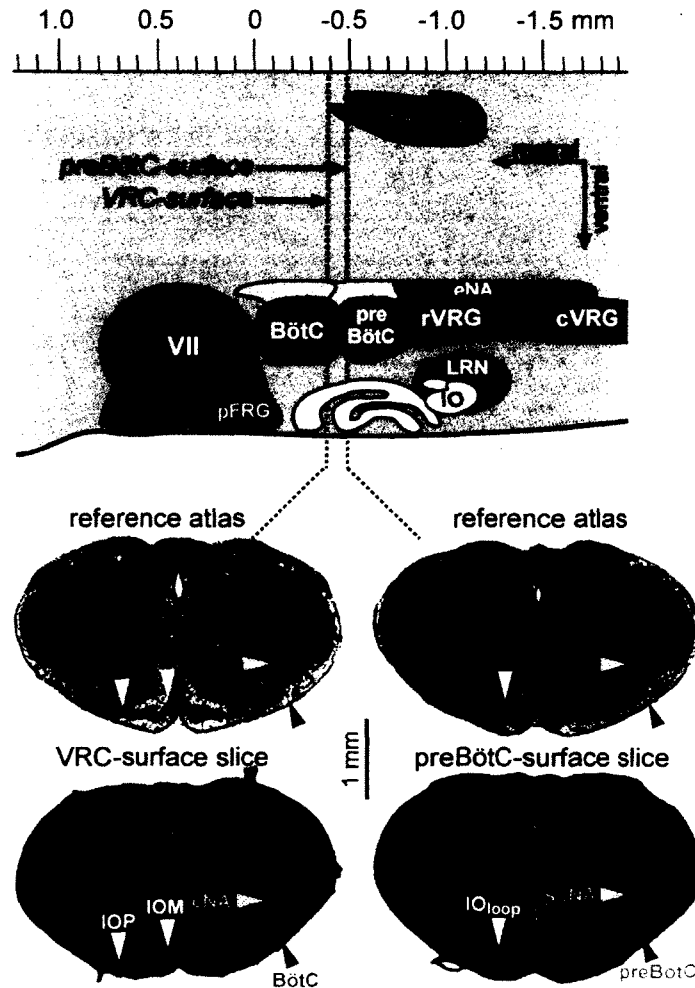


**Figure 2.1** Anatomy of slices that retain the preBötC. Para-sagittal view (top) shows nuclei that comprise the ventral respiratory column (VRC): Bötzing complex (BötC), preBötzing complex (preBötC), rostral and caudal ventral respiratory group (rVRG and cVRG), facial nucleus (VII), and the parafacial respiratory group (pFRG). Also shown are the compact, semi-compact, and external (loose) formations of the nucleus ambiguus (cNA, scNA, and eNA). The hypoglossal nucleus (XII) is shown dorsally. The principal and medial divisions of the inferior olive (IOP and IOM), and the visible loop (IO<sub>loop</sub>), are located, with the lateral reticular nucleus (LRN), ventral to the VRC. The axis (top) is reproduced from brainstem atlas for newborn mice; preBötC-surface and VRC-surface slices are shown with reference images.

identified by the appearance of dorsomedial cell column and principal lateral loop of the inferior olivary (IO) nucleus, and the area postrema, at which point the fourth ventricle opens to the obex.

In contrast, the geometry of the second slice type exposed a rostrally adjacent region of the ventral respiratory column (VRC). The rostral surface of this slice type was located at least 100  $\mu\text{m}$  rostral to the preBötC (i.e., a VRC-surface slice, **Fig. 2.1**). In these slices, the dorsal part of the principal loop of the IO reaches the midline while its ventral part intersects with the dorsal IO. These slices were calibrated online according to a respiratory brainstem histology atlas for newborn mice (Ruangkittisakul et al. 2011). Slice geometry was subsequently confirmed after the experiment via anatomical processing (see details below).

Experiments were carried out in three steps by Ablator software package as described in **Chapter 1 (Fig. 1.2)**. Rhythmically active inspiratory neurons were detected via fluorescent  $\text{Ca}^{2+}$  imaging combined with the iterative threshold-crossing analysis and additional layers of rhythmicity evaluation (**Chapter 1 Methods**). Ablations were performed using the Ti:sapphire laser to spot-scan cell targets with 800-nm pulses at maximum intensity until each target was vaporized (**Chapter 1 Methods**).

We measured XII burst amplitude, cycle period, and coefficient of variation (CV) using Chart software (ADInstruments, Colorado Springs, CO) and custom Python scripts. Most measurements were compared for pre- and post-lesion conditions. Each data set was tested for normality using a Shapiro-Wilk test. We rejected the null hypothesis that the data were drawn from a normal distribution if the p-value was less than alpha 0.05. Data that could be considered normally distributed were compared using two-tailed unpaired t-tests, whereas data that did not conform

to the normal distribution were compared using non-directional (two-tailed) Mann-Whitney *U*-tests. XII burst area, amplitude, cycle period, and CV are reported in the Results section with standard error (i.e., mean  $\pm$  SEM). Discrete cell counts (pertaining to the number of cells detected or the number of cells lesioned) are reported according to the mean and standard deviation (i.e., mean  $\pm$  SD) because the SD conveys a more accurate sense of the range of cell counts. Both SEM and SD are reported in Tables 1 and 2 for cell counts.

We computed a regularity score ( $R_n$ ) to assess cycle-to-cycle changes in the respiratory period *in vitro*.  $R_n$  was defined as the quotient of period of the present cycle ( $T_n$ ) with respect to the mean cycle period for the previous  $M$  cycles ( $T_{n-M}, \dots, T_{n-1}$ ). We set  $M=10$ . The final expression for  $R_n$  is:

$$R_n = T_n / (\sum(T_{n-M}, \dots, T_{n-1}) / M), M=10.$$

$R_n$  value of 1 nominally indicates perfect regularity with respect to the preceding  $M$  cycles;  $R_n$  of 2 would be a burst cycle twice as slow as the preceding epoch, and so on.  $R_n$  is advantageous because it not only provides a metric of fluctuation, but also shows whether the fluctuations are tending toward longer ( $R_n > 1$ ) or shorter ( $R_n < 1$ ) cycle periods.

We used an online calibrated atlas of the neonatal mouse respiratory network to verify the respiratory brain stem structures retained at the rostral face of each slice preparation (Ruangkittisakul et al. 2011). Slices were subject to a more rigorous off-line analysis after each experiment using the following procedure. The slice was placed into fixation solution composed of 4% paraformaldehyde in phosphate buffer (1:2 mixture of 0.1 M  $\text{NaH}_2\text{PO}_4$  + 0.1 M  $\text{Na}_2\text{HPO}_4$  in double-distilled deionized water, pH = 7.2) for at least 1 hour. The slice was then rinsed in phosphate buffer for 2 min, washed in de-ionized distilled water ( $\text{dH}_2\text{O}$ ) briefly thereafter and

transferred onto a glass slide. Then the slice was submerged for 60-75 s in staining solution containing 1% thionin acetate, 0.1 M sodium acetate trihydrate, and 0.1 M acetic acid. Afterwards, stained slices were consecutively washed with dH<sub>2</sub>O (30 s), 50% ethanol (1 min), 70% ethanol (1 min), 50% ethanol (1 min), and phosphate buffer (10 min). Finally, washed slices were transferred to a Petri dish in phosphate buffer and photographed via digital CCD (Infinity 1-2M, 2.0 Megapixel, Lumenera, Ottawa, Ontario, Canada) through a stereomicroscope (EMZ-8TR, magnification 45x, Meiji Techno America, Santa Clara, CA). Each slice preparation was classified as either a VRC-surface or preBötC-surface based on neuroanatomical landmarks (Fig. 2.1 illustrates some characteristic features that differentiate the VRC-surface and preBötC-surface slices). Slices with ambiguous structures were discarded.

### **2.3. Results**

Breathing-related neurons form a ventral respiratory column (VRC) that begins at the caudal pole of the facial nucleus (VII) and spans past the spinomedullary junction into the cervical spinal cord. Contiguous respiratory nuclei serve different functions. The preeminent rhythmogenic role for the inspiratory phase of breathing is attributed to interneurons within the bilaterally distributed preBötC (Feldman & Del Negro 2006; Smith et al. 1991; Gray et al. 2001; Tan et al. 2008; Ren & Greer 2006). Transverse slice preparations that capture the preBötC generate inspiratory-related rhythms *in vitro* that are measurable as motor output from the hypoglossal (XII) nerve rootlets (Smith et al. 1991; Janczewski & Feldman 2006) (Fig. 2.2A).

We sought to interrogate network properties in the preBötC by deleting its constituent interneurons, one cell at a time, while monitoring network function via the XII nerve. As described in **Chapter 1**, our setup consists of one master computer that controls a Ti:sapphire long-wavelength laser, a laser-scanning microscope, and a

robotic xy stage control system, while another workstation that is time-synced to the master monitors preBötC network activity continuously via XII recordings (Fig. 1.1).

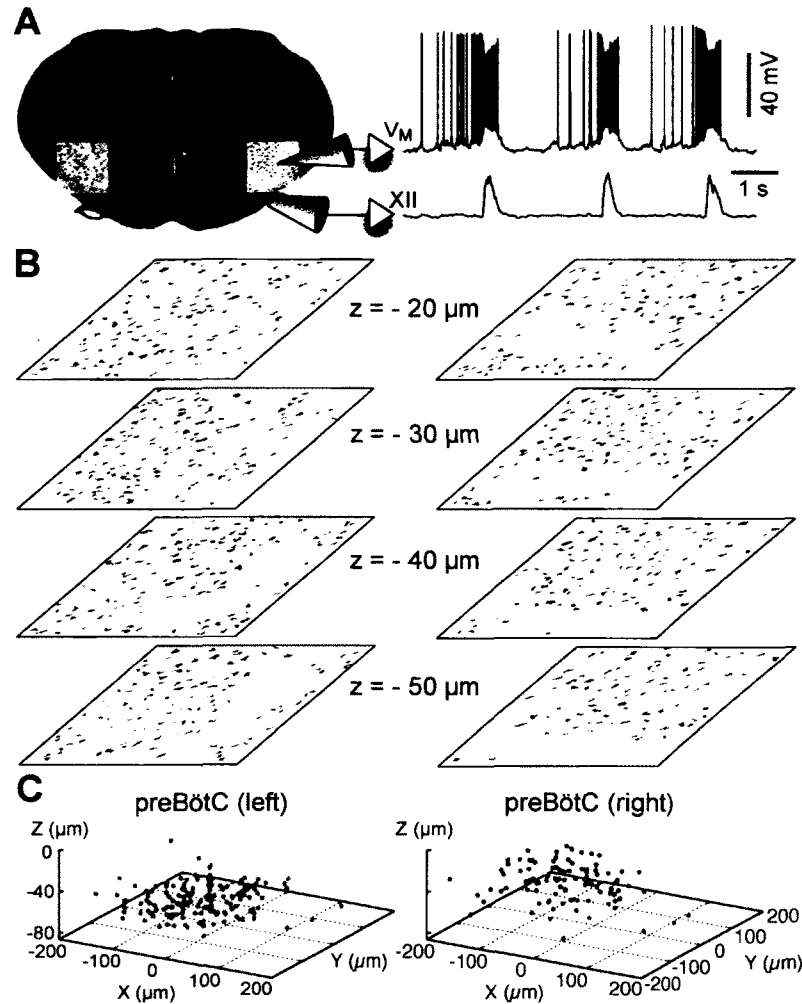


**Figure 2.2** Inspiratory neurons in the preBötC. (A) Rhythmically active neurons identified bilaterally by imaging. Whole-cell recording (upper trace) with XII motor output (lower trace). (B) Mask of targets showing inspiratory (red) and non-inspiratory neurons (blue) for focal planes (from -20 to -50  $\mu\text{m}$  shown here). (C) 3D reconstruction of detected targets for focal planes from -20 to -50  $\mu\text{m}$ , where each inspiratory neuron is represented by a single point at the soma.

### ***Detecting and ablating inspiratory neurons in the preBötC and ventral respiratory column***

We implemented two cutting strategies to prepare transverse slices that both retain the preBötC and expose inspiratory-modulated neurons at the slice surface (Fig.

2.1). The geometry of the first slice type exposed the VRC at least 100  $\mu\text{m}$  rostral to the preBötC (i.e., a *VRC-surface slice*), whereas the second type exposed the preBötC at its rostral face (i.e., a *preBötC-surface slice*, Fig. 2.1). These slices were calibrated online according to a respiratory brainstem histology atlas for newborn mice (Ruangkittisakul et al. 2011). After cutting, slices were incubated with the  $\text{Ca}^{2+}$ -sensitive indicator Fluo-8 AM to detect rhythmic inspiratory activity. We were able to image to a depth of 80  $\mu\text{m}$  using Ti:sapphire laser pulses in both slice types. Synaptic inhibition is not essential for rhythmogenesis *in vitro*, but it influences the amplitude of XII motor output (Ritter & Zhang 2000; Kuwana et al. 2006). Therefore, we added 5- $\mu\text{M}$  strychnine and picrotoxin to the ACSF prior to starting the detection phase so that XII output would be insensitive to the effects of laser-ablating inhibitory neurons (Winter et al. 2009; Ruangkittisakul et al. 2009) during the subsequent ablation phase.

Inspiratory-modulated neurons could be identified automatically by Ablator (see details in Chapter 1 Methods, *Detecting and lesioning neuron targets*). Detection was repeated bilaterally at all resolvable depths (Fig. 2.2B, only four focal planes on each side of the preBötC are shown in this panel). Inspiratory neurons occupied a roughly circular region 150-200  $\mu\text{m}$  in diameter in the ventrolateral margins of the slice, which is characteristic of nuclei throughout the VRC, including – but not limited to – the preBötC (Fig. 2.2A).

PreBötC-surface slices showed on average  $9 \pm 5$  (mean  $\pm$  SD) rhythmic neurons per 10- $\mu\text{m}$  plane per side (n=5 slices). VRC-surface slices showed on average  $12 \pm 9$  inspiratory neurons per plane per side (n=8 slices). This difference was not statistically significant (p=0.2, Mann-Whitney *U*-test, Fig. 2.3, Tables 2.1,2.2).



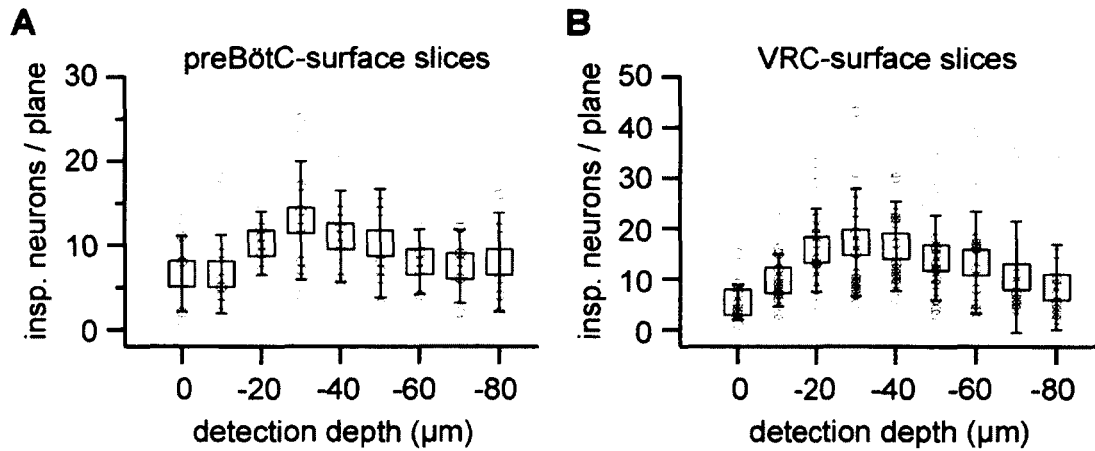


**Figure 2.3** Average number of inspiratory neurons detected at each acquisition depth in both VRC-surface slices and preBötC-surface slices. **(A)** Number of inspiratory neurons detected per 10- $\mu\text{m}$  focal plane per side in preBötC-surface slices from  $z=0$  (surface) to  $z=-80$   $\mu\text{m}$ . See **Table 2.1** for numerical values. **(B)** Number of inspiratory neurons detected per 10- $\mu\text{m}$  focal plane per side in VRC-surface slices from  $z=0$  to  $z=-80$   $\mu\text{m}$ . See **Table 2.2** for numerical values. The number of inspiratory neurons detected per focal plane per side are shown individually for each individual experiment with gray circles. The mean  $\pm$  SD for all experiments are shown with black lines and square symbols.

**Table 2.1** Number of inspiratory neurons detected per 10- $\mu\text{m}$  plane per side in  $n=5$  preBötC-surface slices. Corresponds to **Fig. 2.3A**.

Depth ( $\mu\text{m}$ )	0	-10	-20	-30	-40	-50	-60	-70	-80	all
Mean	6.6	6.6	10.0	12.9	11.0	10.2	8.0	7.5	8.0	9.2
SD	4.5	4.6	3.8	7.0	5.4	6.4	3.9	4.3	5.8	5.4
SEM	1.6	1.6	1.3	2.2	1.9	2.1	1.4	1.5	2.6	0.6
Max	13	18	17	25	21	24	13	13	16	25
Min	1	3	3	4	5	3	2	2	2	1

**Table 2.2** Number of inspiratory neurons detected per 10- $\mu\text{m}$  plane per side in  $n=8$  VRC-surface slices. Corresponds to **Fig. 2.3B**.

Depth ( $\mu\text{m}$ )	0	-10	-20	-30	-40	-50	-60	-70	-80	all
Mean	5.2	9.5	14.8	15.8	15.8	13.3	12.6	9.7	7.9	11.7
SD	3.5	5.1	8.2	10.6	8.8	8.4	10.1	11.0	8.4	9.1
SEM	0.9	1.3	2.0	2.7	2.2	2.1	2.5	2.8	2.2	0.8
Max	15	22	33	43	31	34	39	39	35	43
Min	1	2	5	5	4	3	2	1	1	1

Following the detection phase, inspiratory neurons were randomly selected from the 3D collection of targets (e.g., **Fig. 2.2C**) and subjected to laser-ablation, one cell at a time. The Ti:sapphire laser was focused on the target and then scanned over a 110  $\mu\text{m}^2$  sub-region at the center of the ROI with 800-nm pulses at full intensity, while acquiring an image in the band 560-615 nm. The lesion was confirmed by analyzing the acquired image (see details in **Chapter 1 Methods, *Detecting and lesioning neuron targets***). Ablator obtained lesion confirmation 91 $\pm$ 1% of the time over all experiments (n=2331 lesion attempts in n=13 slices). During any experiment, only confirmed lesions were added to the tally. After each ablation the system randomly selected another target and attempted another lesion. Since the preBötC is bilaterally distributed, the specimen stage was left-right alternated after every 50<sup>th</sup> lesion. The system looped between target selection and laser ablation until the whole 3D set of targets was exhausted on both sides. We continuously monitored the XII nerve output to evaluate changes in respiratory network function.

#### ***Ablation of inspiratory neurons from the ventral respiratory column***

Prior to lesioning, VRC-surface slices and preBötC-surface slices (**Fig. 2.1**) function indistinguishably from the standpoint of XII motor output because both slices retain the necessary and sufficient medullary circuits to generate spontaneous respiratory rhythms *in vitro* (Janczewski & Feldman 2006; Ruangkittisakul et al. 2011). However, these two cutting strategies expose different respiratory circuits at the rostral face of the slice. VRC-surface slices expose respiratory neurons rostral to the preBötC, in a region that includes the Bötzing complex (BötC) (Barnes et al. 2007; Ptak et al. 2009), which is not associated with inspiratory rhythmogenesis. We hypothesized

that cumulative ablation of VRC inspiratory neurons at the level of the BötC would not affect cycle period or stop rhythmogenesis.

We cumulatively ablated an average of  $192 \pm 80$  inspiratory neurons in VRC-surface slices ( $n=8$  slices, **Fig. 2.4A**). The magnitude of the XII output always measured  $\geq 50\%$  of its control amplitude during the entire ablation phase (**Fig. 2.5A**). On average, the XII motor amplitude measured  $76 \pm 7\%$  of control during the *post-lesion epoch* (32 min of continuous recording following the final target ablation, **Fig. 2.5B**). The respiratory cycle period did not change significantly during the ablation phase or during the post-lesion epoch (**Fig. 2.5C,D**). Cycle period measured  $5.2 \pm 0.3$  s during the *pre-lesion epoch* (the period of time from the end of the detection phase to the beginning of the ablation phase) and  $4.3 \pm 0.3$  s during the post-lesion epoch ( $p=0.07$ , t-test). Additionally, the coefficient of variation (CV) of pre-lesion periods was not significantly different from post-lesion periods (pre-lesion  $CV=0.41 \pm 0.04$ ; post-lesion  $CV=0.33 \pm 0.04$ ,  $p=0.13$ , t-test, **Fig. 2.5E**). The regularity score ( $R_n$ ), which measures cycle-to-cycle fluctuations in period, settled at  $\sim 1$  after the ablation phase, which implies nominally perfect regularity (e.g., **Fig. 2.4A**). These data show that cumulative ablation of inspiratory neurons outside of the preBötC does not perturb or stop spontaneous respiratory rhythms *in vitro*, although the amplitude of XII motor output declines.

#### ***Ablation of inspiratory neurons in preBötC***

The outcome was different in preBötC-surface slices ( $n=5$  slices, **Fig. 2.4B**). Cumulative single-cell laser ablations decreased the amplitude of XII output as well as respiratory frequency (**Fig. 2.5A-D**), and ultimately stopped the rhythm altogether (**Figs. 2.4B, 2.6A**). During the ablation phase in preBötC-surface slices, the amplitude of XII motor output declined 0.6% per neuron deleted, whereas in VRC-

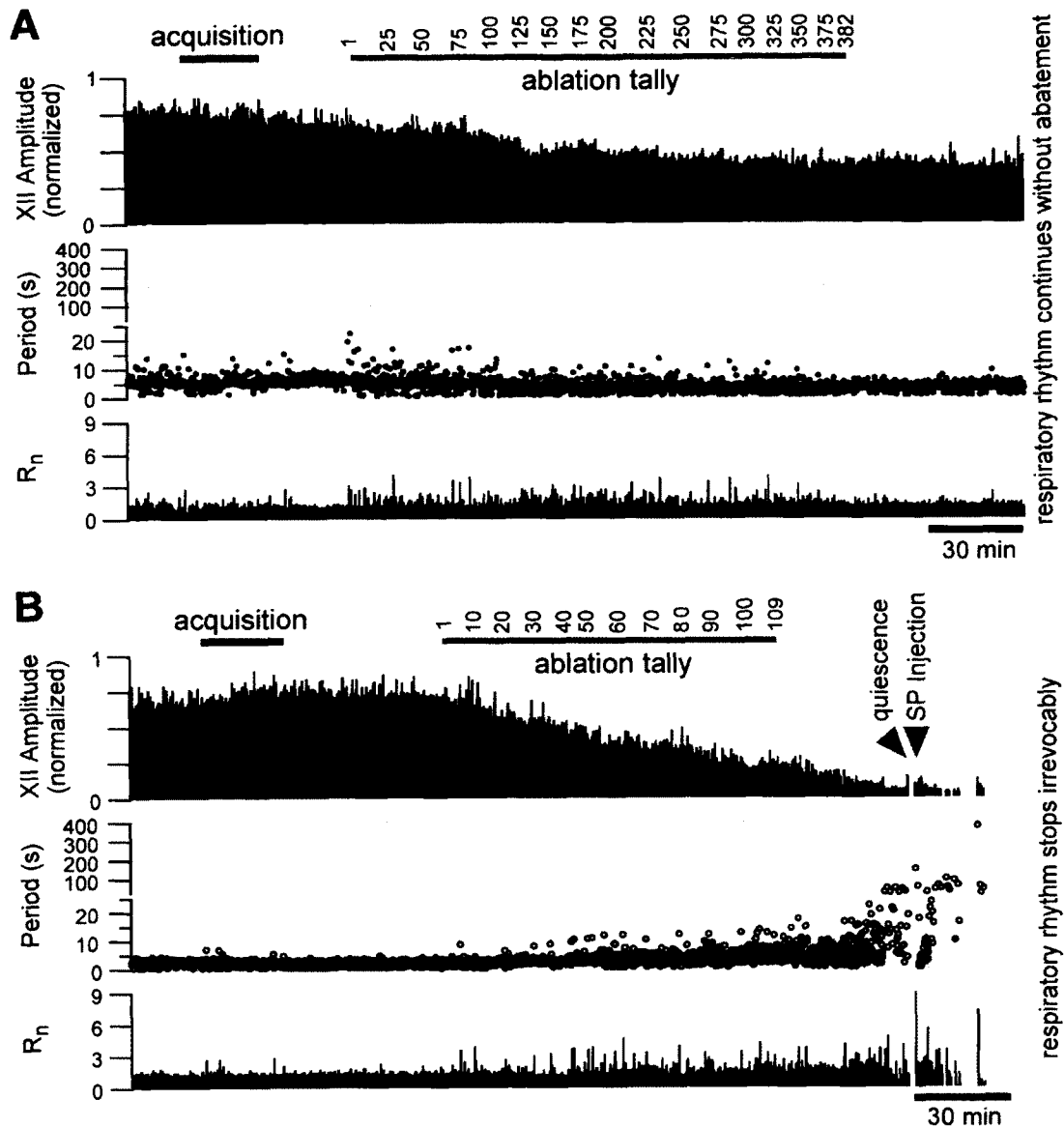


**Figure 2.4** Cumulative deletion of inspiratory neurons. **(A-B)** The x-axis is a timeline. The y-axis plots XII amplitude (normalized units, top), respiratory period (middle), and regularity score ( $R_n$ ) (bottom). The respiratory period axis is continuous (0-400 s) but plotted with two scales. Major ticks are separated by 5 s from 0-25 s, and thereafter major ticks are plotted in 100 s divisions from 26-400 s. Period and regularity axes plot a data point for every instantaneous period measured. The recording in **B** stops after 10 min of XII quiescence. **(A)** Ablating inspiratory neurons in a VRC-surface slice preparation. **(B)** Ablating inspiratory neurons in a preBötC-surface slice preparation with SP injection (right red triangle).

surface slices it declined 0.16% per neuron deleted, which was significantly different ( $p=0.001$ , Mann-Whitney  $U$ -test,  $n=8$  vs.  $n=5$  slices tested, **Fig. 2.5A**). The amplitude

of XII motor output of preBötC-surface slices declined to  $37\pm 7\%$  of control during the post-lesion epoch, which was significantly greater than the XII decline measured similarly post-lesion in VRC-surface slices ( $p=0.002$ , t-test, **Fig. 2.5B**).

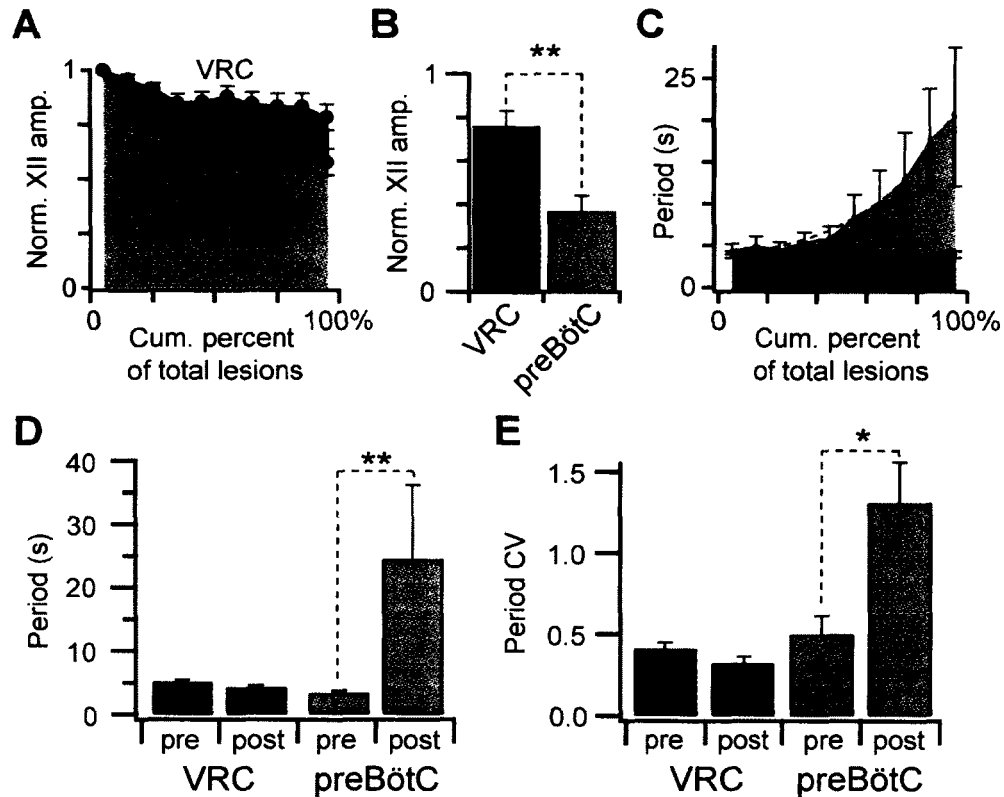


**Figure 2.5** Ablation effects on respiratory rhythm and XII amplitude. (A-E) Measurements are displayed in light grey for preBötC-surface slices and dark grey for VRC-surface slices. (A) XII amplitude vs. cumulative percent of total lesions. (B) Post-lesion changes in XII amplitude (\*\* indicates statistical significance at  $p=0.001$ ). (C) Cycle periods vs. cumulative percent of total lesions. A dashed exponential function is fit to the cycle period data for preBötC-surface slices. (D) Mean cycle period for pre- and post-lesion epochs, (\*\* indicates statistical significance at  $p=0.008$ ). (E) Mean CV for pre- and post-lesion epochs (\* indicates statistical significance at  $p=0.02$ ).

The respiratory cycle period increased during the course of lesioning with respect to the percent of total neurons lesioned (**Fig. 2.5C**). The cycle period also continued to increase after lesion targets were exhausted (reaching 120-200 s **Figs. 2.4B, 2.6A**). The mean period for the post-lesion epoch was  $25\pm 12$  s, which compared to  $3.4\pm 0.4$  s pre-lesion, was statistically significant ( $p=0.008$ , Mann-Whitney *U*-test, **Fig. 2.5D**). Post-lesion periods formed a unimodal long-tail

distribution without exhibiting discrete jumps in periodic activity, i.e., quantal slowing (Ren & Greer 2006). There was also a statistically significant change in the CV for cycle period, which measured  $0.5 \pm 0.1$  pre-lesion and  $1.3 \pm 0.3$  during the post-lesion epoch ( $p=0.02$ , Mann-Whitney *U*-test, Fig. 2.5E). Unlike VRC-surface slices in which cycle period re-established regularity after the ablation phase, preBötC-surface slices showed large cycle-to-cycle fluctuations in period that are reflected in  $R_n$  measurements in the range of 1-9 after the ablation phase (Fig. 2.4).

On average, the confirmed deletion of  $120 \pm 45$  preBötC neurons (mean  $\pm$  SD) resulted in rhythm cessation  $32 \pm 2$  min (mean  $\pm$  SEM) after the final cell ablation. We continued to monitor XII activity to confirm that rhythm never recovered spontaneously within a 2-3 hours range ( $n=5$ ).

#### ***Transiently rescuing rhythmic, but irregular, preBötC activity***

The data in Figs. 2.4 and 2.5 suggest that the cumulative deletion of inspiratory neurons in preBötC-surface slices had a profound effect on XII output and caused a catastrophic change in the CPG that degraded and destabilized its rhythmogenic capability. However, another explanation could simply involve a loss of excitatory drive to the rhythmogenic core in preBötC-surface slices because of the ablation of rhythmic neurons that support CPG function via neuromodulation. This potential explanation could be supported by the fact that rhythm cessation never occurred during a bout of lesions in preBötC-surface slices but after a slow decay of XII amplitude, frequency, and regularity post-lesion (Fig. 2.4B). Monoaminergic and peptidergic projections ordinarily maintain excitability in the preBötC and exogenous substance P (SP) has widely been used to boost preBötC excitability transiently by acting on the core population of NK1R-expressing rhythmogenic interneurons (Ptak et al. 2009). Monoaminergic and peptidergic neurons also receive feedback

projections from the preBötC, which endows them with respiratory rhythmicity and makes them susceptible to loss of input due to the cumulative laser ablation protocol. To test the idea that sequential lesions simply reduce preBötC excitability, we injected a bolus of SP into the preBötC after the respiratory cycle period exceeded

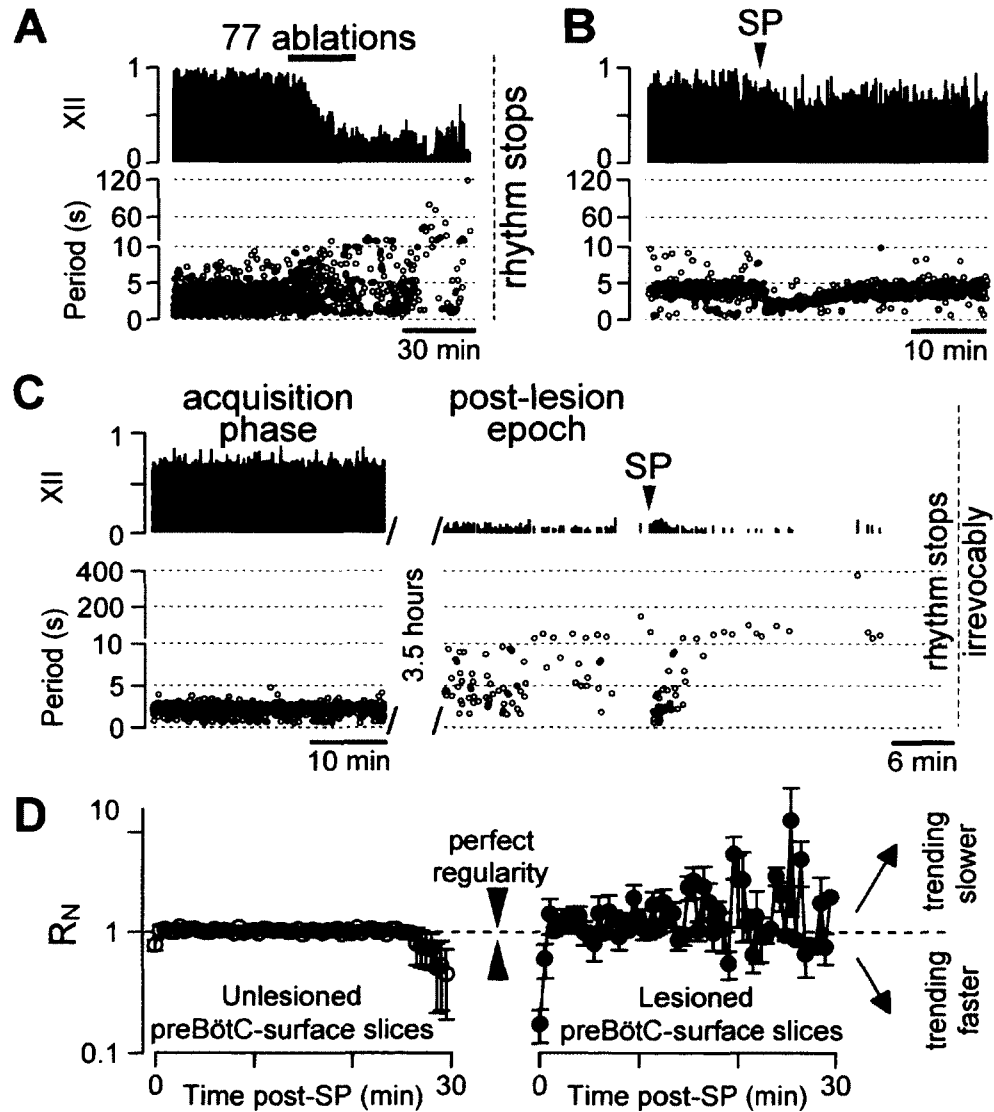


**Figure 2.6** SP injections in preBötC-surface slices. (A) Lesioned preBötC-surface slice without SP injection. (B) Un-lesioned preBötC-surface slice injected with a bolus of SP. (C) Lesioned preBötC-surface slice shown in the acquisition phase (left) and 3.5 hours later during the post-lesion epoch (right). (D)  $R_N$  binned in 0.5 min increments for un-lesioned preBötC-surface slices (left, n=4) and lesioned preBötC-surface slices (right, n=5) following SP injection at t=0. Values approaching one are increasing in regularity whereas values greater than or less than unity are becoming more irregular.

120 s, which we empirically determined was a reliable benchmark of a slice that, without SP injection, would cease rhythmic function within 5-10 min (e.g., Fig. 2.6A).

Slices bathed in 9 mM K<sup>+</sup> ACSF normally discharge XII bursts with a cycle period of ~5 s. In n=4 un-lesioned preBötC-surface slices that served as controls, bolus injection of 1 mM SP transiently lowered the average cycle period to 2.2±0.2 s (mean ± SEM, computed for 25 consecutive XII bursts); period remained below 5 s for 13±1 min (Fig. 2.6B). In n=5 lesioned preBötC-surface slices, bolus SP injection revived activity transiently (Figs. 2.4B,2.6C). The average cycle period was 1.8±0.2 s (mean ± SEM, computed for 10 consecutive XII bursts); period remained below 5 s for 5±1 min. Judged by the duration that the cycle periods remained less than 5 s, the effect of SP was significantly shorter in lesioned preBötC-surface slices compared to un-lesioned ones (p=0.002, t-test, Fig. 2.6B,C). Furthermore, lesioned preBötC-surface slices did not continue rhythmic output indefinitely after the effects of the SP injection subsided, whereas un-lesioned controls maintained rhythmicity for 4-6 hours. More importantly, the SP-revived rhythmic activity in lesioned preBötC-surface slices was irregular, whereas un-lesioned controls maintained nearly perfect regularity scores post-SP injection (Fig. 2.6D). Together, these observations suggest that NK1R-expressing neurons in the preBötC core of lesioned slices still form a network that can generate irregular cycles if suitably modulated, but this network cannot sustain regular rhythmogenesis.

For those measurements that were compared for pre- and post-lesion conditions previously, we defined the *pre-lesion epoch* as the period of time from the end of the detection phase to the beginning of the ablation phase (~30 min) and the *post-lesion epoch* as 32 min of continuous data after the final cell lesion of the ablation phase. The duration for *post-lesion epoch* was chosen because it represents



the average time preBötC-surface slices remained active post-lesion. That is, lesioned preBötC-surface slices showed a progression to longer cycle periods during and after the ablation phase, and ultimately cease functioning after the ablation phase when the cycle period reached 120 s. This outcome generally occurred 32 min after the final single-cell ablation on average (n=5 preBötC-surface slices).

## 2.4. Discussion

Laser ablation has been applied to study locomotor networks. In zebrafish cyan (488-nm) laser exposure for 10-12 min photoablated reticulospinal neurons by augmenting the toxicity of indicator dyes, revealing specific roles for Mauthner cells and their homologs in short-latency escape behaviors (Liu & Fetcho 1999). Ultraviolet lasers (~400 nm) were used in *C. elegans* to investigate locomotion, chemotaxis, and mechanosensation (Bargmann & Avery 1995). Cell killing required several minutes of laser exposure and often damaged surrounding tissues. In zebrafish and *C. elegans* prior knowledge of cell locations was required to ablate the targets manually. The system we developed (Chapter 1) does not require *a priori* knowledge of target cell locations. The map of targets is generated online and measurable cell function is the principal selection criterion. Laser ablation is fast too; each lesion can be accomplished in 2-16 s. These features are important for applicability in mammalian networks where there may be hundreds of cell targets, and aside from general neuroanatomical guidelines, the specific map of targets is unknown beforehand.

Viral transfection can be used to silence neuron populations (Lechner et al. 2002). Knock-out mice, or conditional knock-outs, also remove cell classes wholesale rather than piecewise (Jackson & Abbott). These techniques operate at the whole-population level and have proven helpful in answering questions regarding *which cells* generate a particular behavior. However, such techniques do not allow

cellular-level quantitative analyses of lesion effects on behavior. Similarly, the toxin saporin causes graded cell destruction over several days, but it is impossible to keep a running tally of cell destruction *in vivo* while monitoring behavioral changes (Gray et al. 2001; McKay et al. 2005; Mantyh et al. 1997). We developed the present system for slices that retain behaviorally relevant function and expose CPG interneurons. Single-cell ablations elicit real-time feedback to address the question *how many neurons contribute to sustaining network function?* Understanding the robustness of network behavior when constituent nodes are attacked is a cross-disciplinary problem in the science of networks (Barabási 2003; Newman et al. 2006; Callaway et al. 2000; Albert et al. 2000) with obvious ramifications for circuits in the brain.

In both slice types the amplitude of XII output decreased as a function of lesion tally. Nevertheless, the XII amplitude decreased more in preBötC-surface slices, which suggests that the preBötC has some premotor function and does not perform a purely rhythmogenic clock-like function. This conclusion is consistent with whole-cell recordings demonstrating that excitatory drive from the preBötC is conserved in XII premotor circuits (Koizumi et al. 2008).

Respiratory period and CV increased in preBötC-surface slices as the lesion tally increased. Cycle period and CV did not show similar changes in VRC-surface slices. We conclude that respiratory period and its regularity are directly related to the number of rhythmogenic neurons in the preBötC. However, the cycle period continued to lengthen after the lesioning stopped, with rhythm cessation occurring after ~30 min. What causes this delay? Ablating a glutamatergic neuron removes AMPA receptor-mediated input from its synaptic partners, but also removes the input mediated by metabotropic glutamate receptors (mGluRs) that regulate

phosphoinositide intracellular signaling and maintain robust function of inspiratory burst-generating conductances. Intracellular pharmacology experiments have shown that antagonists of the phosphoinositide signaling system can take 20–40 minutes to attenuate excitability and burst generation (Crowder et al. 2007; Pace et al. 2007). Therefore, the delayed effects of cumulative single-cell laser ablations on cycle period are attributable, at least in part, to the rundown of phosphoinositide signaling after removal of mGluR-mediated drive.

The present results support the hypothesis that laser ablations destroy a critical mass of the preBötC core that precludes rhythm generation. As an additional metric to assess the post-lesion state of the CPG, we exploited previous evidence that SP excites NK1R-expressing preBötC neurons to boost respiratory activity (Gray et al. 1999). Lesioned preBötC-surface slices exhibited irregular SP-evoked rhythms that were unsustainable (Fig. 2.6C,D). We conclude that the cumulative serial ablation leaves the respiratory CPG irreparably damaged.

As a consequence, this study provides a novel measurement that can help quantify network properties of the preBötC: the destruction of  $120 \pm 45$  inspiratory neurons stops the spontaneous respiratory rhythm irreversibly *in vitro*. An important consideration is that neuroanatomical evidence shows that approximately half of the neurons in the preBötC are inhibitory, either glycinergic or GABAergic, and half are glutamatergic (Winter et al. 2009; Gray et al. 2010). Glutamatergic transmission is obligatory for rhythmogenesis *in vitro* (Wallen-Mackenzie et al. 2006; Funk et al. 1993), whereas inhibitory transmission is not (Feldman & Smith 1989; Brockhaus & Ballanyi 1998). Synaptic inhibition nonetheless regulates the amplitude of XII motor output (Ren & Greer 2006; Ritter & Zhang 2000). To focus on the role of glutamatergic neurons, we performed these experiments in the presence of

picrotoxin and strychnine. Disinhibition conditions ensured that deleting inhibitory neurons would not affect the XII output. Inspiratory neurons express both excitatory (Gray et al. 2010; Guyenet et al. 2002; Stormetta et al. 2003; Bouvier et al. 2010) and inhibitory (Kuwana et al. 2006; Winter et al. 2009) transmitters, but it is not possible to differentiate the two phenotypes based on  $\text{Ca}^{2+}$  transients in rhythmically active slices. Therefore, approximately half of the targets in our experiments are presumably inhibitory and should be discounted from the lesion tally. We conclude that deleting  $60 \pm 23$  glutamatergic neurons (mean  $\pm$  SD) stopped respiratory rhythmogenesis *in vitro*.

From the number of inspiratory neurons detected per imaging plane, we may estimate the population of the preBötC core by extrapolating through the volume of the preBötC and correcting for the fraction of cells that are inhibitory. We detected the highest number of inspiratory neurons in the preBötC at  $-30 \mu\text{m}$  (13 per side, **Table 2.1**). Therefore, we assume that, on average, fewer than 13 neurons were detected at superficial levels due to slicing-related tissue damage, and that fewer than 13 neurons were detected at deeper levels due to limited dye penetration and scattering of laser pulses (Svoboda & Yasuda 2006). Even if technical limitations prevented their detection, we assume an average uniform density of 13 inspiratory neurons per  $10\text{-}\mu\text{m}$  per side in the preBötC, which occupies  $250\text{-}\mu\text{m}$  in the rostrocaudal axis, bilaterally (Ruangkittisakul et al. 2006; Ruangkittisakul et al. 2011; Gray et al. 2010). Thus we calculate 650 inspiratory neurons comprise the preBötC. If half are inhibitory (Winter et al. 2009; Gray et al. 2010), then the rhythm-generating glutamatergic core contains 325 interneurons.

These data and calculations imply that destroying 18% (60/325) of the preBötC core, with the 95% confidence intervals of 4% (14/325) to 33% (106/325),

stopped the respiratory rhythm. Because bolus injection of SP evoked a transient sequence of XII bursts, connectivity among core neurons must still exist. As a consequence, we conclude that the lesion procedure did not destroy the respiratory rhythm-generating network *per se*, but destroyed enough of it to preclude sustainable and stable rhythmic function *in vitro*. It may be possible to restore some functionality to a lesioned preparation by exploiting the remaining un-lesioned neurons and their connectivity, but to attempt to do so is beyond the scope of the present study.

## 2.5. References

**Albert R, Jeong H & Barabási AL (2000)** Error and attack tolerance of complex networks. *Nature* 406, 378-382.

**Bargmann C, Avery L (1995)** Laser killing of cells in *Caenorhabditis elegans*. In: *Caenorhabditis elegans: modern biological analysis of an organism*, vol. 48 (Epstein, H. and Shakes, D., eds), pp 225-250 Amsterdam: Elsevier.

**Barabási AL (2003)** *Linked : how everything is connected to everything else and what it means for business, science, and everyday life*. (Plume, New York).

**Barnes BJ, Tuong CM, Mellen NM (2007)** Functional imaging reveals respiratory network activity during hypoxic and opioid challenge in the neonate rat tilted sagittal slab preparation. *J Neurophysiol* 97:2283-2292.

**Bouvier J, Thoby-Brisson M, Renier N, Dubreuil V, Ericson J, Champagnat J, Pierani A, Chedotal A, Fortin G (2010)** Hindbrain interneurons and axon guidance signaling critical for breathing. *Nat Neurosci* 13:1066-1074.

**Brockhaus J, Ballanyi K (1998)** Synaptic inhibition in the isolated respiratory network of neonatal rats. *Eur J Neurosci* 10:3823-3839.

**Callaway D, Newman MEJ, Strogatz S & Watts D (2000)** Network robustness and fragility: percolation on random graphs. *Phys Rev Lett* 85, 5468-5471.

**Crowder EA, Saha MS, Pace RW, Zhang H, Prestwich GD, Del Negro CA (2007)** Phosphatidylinositol 4,5-bisphosphate regulates inspiratory burst activity in the neonatal mouse preBötzinger complex. *J Physiol* 582:1047-1058.

**Feldman JL, Del Negro CA (2006)** Looking for inspiration: new perspectives on respiratory rhythm. *Nat Rev Neurosci* 7:232-242.

**Feldman JL, Smith JC (1989)** Cellular mechanisms underlying modulation of breathing pattern in mammals. *Ann N Y Acad Sci* 563:114-130.

**Funk GD, Smith JC, Feldman JL (1993)** Generation and transmission of respiratory oscillations in medullary slices: role of excitatory amino acids. *J Neurophysiol* 70:1497-1515.

**Gray PA, Hayes JA, Ling G, Llona I, Tupai S, Picardo MC, Ross S, Hirata T, Corbin JG, Eugenin J, Del Negro CA (2010)** Developmental Origin of preBötzinger Complex Respiratory Neurons. *J Neurosci* 30:14883-14895.

**Gray PA, Janczewski WA, Mellen N, McCrimmon DR, Feldman JL (2001)** Normal breathing requires preBötzinger complex neurokinin-1 receptor-expressing neurons. *Nat Neurosci* 4:927-930.

**Gray PA, Reikling JC, Bocchiario CM, Feldman JL (1999)** Modulation of respiratory frequency by peptidergic input to rhythmogenic neurons in the preBötzinger complex. *Science* 286:1566-1568.

**Grillner S (2006)** Biological pattern generation: the cellular and computational logic of networks in motion. *Neuron* 52:751-766.

**Guyenet PG, Sevigny CP, Weston MC, Stornetta RL (2002)** Neurokinin-1 receptor-expressing cells of the ventral respiratory group are functionally heterogeneous and predominantly glutamatergic. *J Neurosci* 22:3806-3816.

**Jackson, I.J. & Abbott, C.M. (2000)** *Mouse genetics and transgenics : a practical approach.* (Oxford University Press, Oxford ; New York).

**Janczewski WA, Feldman JL (2006)** Distinct rhythm generators for inspiration and expiration in the juvenile rat. *J Physiol* 570:407-420.

**Kiehn O (2011)** Development and functional organization of spinal locomotor circuits. *Curr Opin Neurobiol* 21:100-109.

**Koizumi H, Wilson CG, Wong S, Yamanishi T, Koshiya N, Smith JC (2008)** Functional imaging, spatial reconstruction, and biophysical analysis of a respiratory motor circuit isolated in vitro. *J Neurosci* 28:2353-2365.

**Kuwana S, Tsunekawa N, Yanagawa Y, Okada Y, Kuribayashi J, Obata K (2006)** Electrophysiological and morphological characteristics of GABAergic respiratory neurons in the mouse pre-Bötzinger complex. *Eur J Neurosci* 23:667-674.

**Lechner HA, Lein ES, Callaway EM (2002)** A genetic method for selective and quickly reversible silencing of Mammalian neurons. *J Neurosci* 22:5287-5290.

**Liu KS, Fetcho JR (1999)** Laser ablations reveal functional relationships of segmental hindbrain neurons in zebrafish. *Neuron* 23:325-335.

**Mantyh PW, Rogers SD, Honore P, Allen BJ, Ghilardi JR, Li J, Daughters RS, Lappi DA, Wiley RG, Simone DA (1997)** Inhibition of hyperalgesia by ablation of lamina I spinal neurons expressing the substance P receptor. *Science* 278:275-279.

**McKay LC, Janczewski WA, Feldman JL (2005)** Sleep-disordered breathing after targeted ablation of preBötzinger complex neurons. *Nat Neurosci* 8:1142-1144.

**Newman, MEJ, Barabási AL & Watts DJ (2006)** *The structure and dynamics of networks*. (Princeton University Press, Princeton).



**Pace RW, Mackay DD, Feldman JL, Del Negro CA (2007)** Inspiratory bursts in the preBötzinger Complex depend on a calcium-activated nonspecific cationic current linked to glutamate receptors. *J Physiol* 582:113-125.

**Ptak K, Yamanishi T, Aungst J, Milesco LS, Zhang R, Richerson GB, Smith JC (2009)** Raphe neurons stimulate respiratory circuit activity by multiple mechanisms via endogenously released serotonin and substance P. *J Neurosci* 29:3720-3737.

**Ren J, Greer JJ (2006)** Modulation of respiratory rhythmogenesis by chloride-mediated conductances during the perinatal period. *J Neurosci* 26:3721-3730.

**Ritter B, Zhang W (2000)** Early postnatal maturation of GABA<sub>A</sub>-mediated inhibition in the brainstem respiratory rhythm-generating network of the mouse. *Eur J Neurosci* 12:2975-2984.

**Ruangkittisakul A, Okada Y, Oku Y, Koshiya N, Ballanyi K (2009)** Fluorescence imaging of active respiratory networks. *Respir Physiol Neurobiol* 168:26-38.

**Ruangkittisakul A, Panaitescu B, Ballanyi K (2011)** K<sup>+</sup> and Ca<sup>2+</sup> dependence of inspiratory-related rhythm in novel "calibrated" mouse brainstem slices. *Respir Physiol Neurobiol* 175:37-48.

**Ruangkittisakul A, Schwarzacher SW, Secchia L, Poon BY, Ma Y, Funk GD, Ballanyi K (2006)** High sensitivity to neuromodulator-activated signaling pathways at physiological [K<sup>+</sup>] of confocally imaged respiratory center neurons in on-line-calibrated newborn rat brainstem slices. *J Neurosci* 26:11870-11880.

**Smith JC, Ellenberger HH, Ballanyi K, Richter DW, Feldman JL (1991)** Pre-Bötzinger complex: a brainstem region that may generate respiratory rhythm in mammals. *Science* 254:726-729.

**Stornetta RL, Rosin DL, Wang H, Sevigny CP, Weston MC, Guyenet PG (2003)** A group of glutamatergic interneurons expressing high levels of both neurokinin-1 receptors and somatostatin identifies the region of the pre-Bötzinger complex. *J Comp Neurol* 455:499-512.

**Svoboda K, Yasuda R (2006)** Principles of two-photon excitation microscopy and its applications to neuroscience. *Neuron* 50:823-839.

**Tan W, Janczewski WA, Yang P, Shao XM, Callaway EM, Feldman JL (2008)** Silencing preBötzinger Complex somatostatin-expressing neurons induces persistent apnea in awake rat. *Nat Neurosci* 11:538-540.

**Wallen-Mackenzie A, Gezelius H, Thoby-Brisson M, Nygard A, Enjin A, Fujiyama F, Fortin G, Kullander K (2006)** Vesicular glutamate transporter 2 is required for central respiratory rhythm generation but not for locomotor central pattern generation. *J Neurosci* 26:12294-12307.

**Winter SM, Fresemann J, Schnell C, Oku Y, Hirrlinger J, Hulsman S (2009)** Glycinergic interneurons are functionally integrated into the inspiratory network of mouse medullary slices. *Pflugers Arch* 458:459-469.

## **CHAPTER 3. Cumulative lesioning of genetically defined respiratory interneurons disrupts and precludes motor rhythms *in vitro***

### **3.1. Introduction**

Breathing in mammals depends on neural rhythms that emanate from the preBötC. Respiratory rhythm generation in the preBötC depends on glutamatergic neurons, as well as neurons that express neuropeptides and peptide receptors (Gray et al. 1999; Gray et al. 2001; Wallen-Mackenzie et al. 2006; Tan et al. 2008). Moreover, neurons with glutamatergic and peptidergic transmitter phenotypes, that also express peptide receptors, form a superset of neurons from the same genetic lineage. Recent findings demonstrated that homeobox gene *Dbx1* controls the fate of glutamatergic commissural interneurons in the hindbrain in mouse embryonic development, and *Dbx1*-expressing progenitors give rise to interneurons in preBötC that are necessary for respiratory rhythm generation *in vivo* and *in vitro* (Bouvier et al. 2010; Gray et al. 2010). Furthermore, using transgenic reporter mice, our group showed that *Dbx1*<sup>+</sup> neurons are inspiratory (i.e., rhythmically active in sync with inspiratory network activity and motor output), and given that there are no other sources of glutamatergic interneurons in ventral medulla, these data suggest that *Dbx1*<sup>+</sup> neurons are not merely an important source of modulatory input that sustains excitability in the preBötC but that these neurons make up its rhythmogenic core (Gray et al. 2010). Characterization of *Dbx1*<sup>+</sup> neurons at cellular level confirms that they express rhythmogenic membrane properties (Picardo 2012). Discovering the developmental origin and identity of the neurons constituting a CPG is crucial for understanding the general principles of neural circuit formation (and function). However, quantifying the neuron populations in a well defined neural network and assessing the sensitivity of

the network in the face of progressive cell loss is another key issue pertaining the basic network properties and disease models.

In this chapter, we address the question by using transgenic reporter mice *Dbx1<sup>CreERT2</sup>;Rosa26<sup>tdTomato</sup>* and *Dbx1<sup>+</sup>/CreERT2;Rosa26<sup>EYFP</sup>*, in which Dbx1-derived neurons express tdTomato and YFP fluorescent proteins, respectively. Reduced slices are prepared as described above (see **Chapter 1 Methods**) to capture the preBötC and retain the minimal inspiratory circuits that spontaneously generate fictive breathing-related activity *in vitro*. We apply the laser detection and ablation approach we developed previously (see **Chapter 1**) to the preBötC to test the hypothesis that cumulative destruction of the respiratory CPG core, which is composed of Dbx1<sup>+</sup> neurons, would cause graded deterioration in network motor activity, and ultimate cessation of inspiratory motor behavior *in vitro*.

Based on extrapolations from experimental results in the previous study, we predicted that deleting  $60 \pm 23$  glutamatergic neurons (mean  $\pm$  SD) would stop respiratory rhythmogenesis *in vitro* (see **Chapter 2 Discussion**). Given that Dbx1<sup>+</sup> neurons are excitatory and comprise the rhythmogenic kernel of the preBötC, we hypothesize that destruction of ~60 Dbx1<sup>+</sup> will preclude the rhythmogenesis *in vitro*.

### **3.2. Methods**

The Institutional Animal Care and Use Committee at The College of William & Mary approved all protocols. Transverse slice preparations (400-450  $\mu$ m) from neonatal (P0-P2) transgenic mice were dissected as described previously (**Chapter 1 Methods**).

Slices containing the preBötC were perfused with 27°C ACSF at 4 ml/min. The external K<sup>+</sup> concentration in the ACSF was raised to 9 mM and inspiratory motor

output was recorded from XII nerve roots. Imaging and ablations were performed using the automated laser detection and ablation system described previously (**Chapter 1 Methods**).

We crossed *Dbx1<sup>+CreERT2</sup>* mice with *Rosa26<sup>tdTomato</sup>* and *Rosa26<sup>EYFP</sup>* Cre-dependent (i.e., floxed) reporter mice to obtain *Dbx1<sup>+CreERT2</sup>;Rosa26<sup>tdTomato</sup>* and *Dbx1<sup>+CreERT2</sup>;Rosa26<sup>EYFP</sup>* pups. Tamoxifen administration to pregnant female mice on the 10<sup>th</sup> day after the plug date produces fluorescent *Dbx1<sup>+</sup>* neurons in ~50% of the offspring. Under epifluorescence microscopy, a bilateral strip of *Dbx1<sup>+</sup>* neurons can be readily visualized in the preBötC and contiguous regions of the dorsomedial medulla (**Fig. 3.1A**).

Two cutting strategies were implemented to prepare transverse slices that both retain the preBötC and expose inspiratory-modulated neurons (**Fig. 3.1B**) at the slice surface as described previously (**Chapter 2 Methods, Fig. 2.1**). preBötC-surface slices and VRC-surface slices were calibrated according to the online histology atlas for newborn mice and the geometry of slice was subsequently confirmed after the experiment via anatomical processing (for details see **Chapter 2 Methods**).

Experiments were carried out in three steps by Ablator software as described in **Chapter 1 (Fig. 1.2)**. The protocols described in **Chapter 2** were followed, except for the detection strategy. In this chapter, fluorescent *Dbx1<sup>+</sup>* neurons were detected via acquisition of high resolution planar images (**Fig. 3.1C<sub>1-2</sub>**), followed by application of the iterative threshold-crossing analysis routine, and finally additional layers of circularity and redundancy analysis (**Chapter 1 Methods, Figs. 1.5,1.6**) to produce mask images for software identified neuron targets (**Fig. 3.1D<sub>1-2</sub>**). Ablations were performed by using the Ti:sapphire laser to spot-scan cell targets, which were

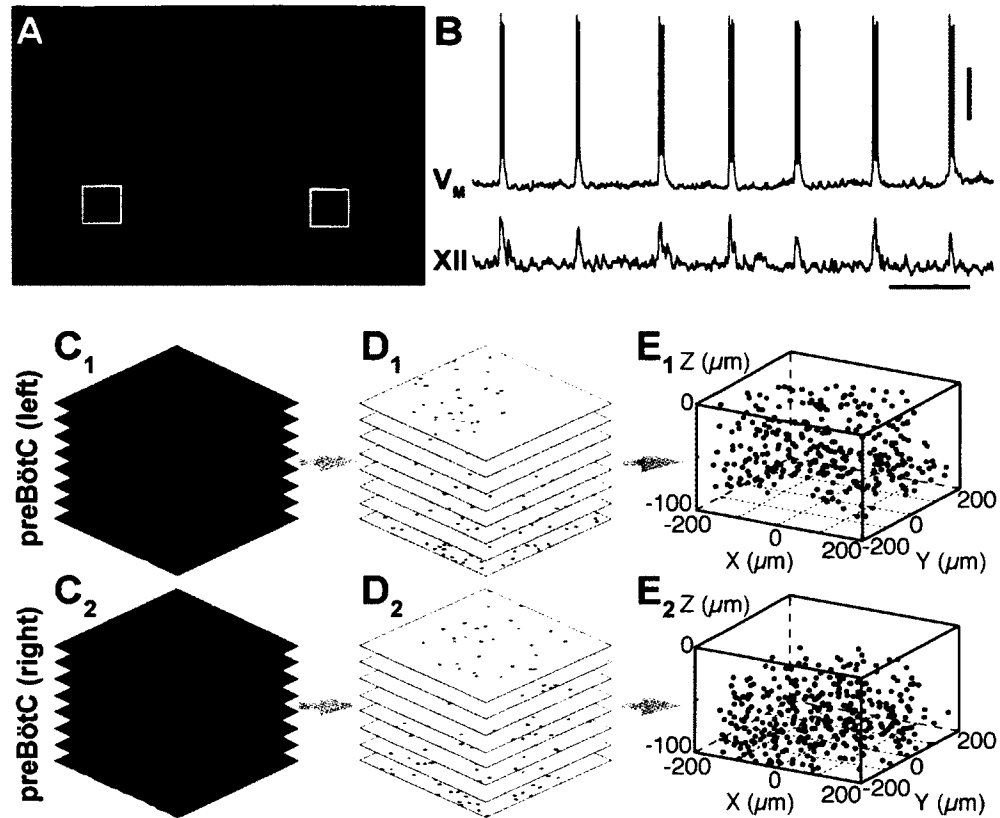


**Figure 3.1** Dbx1<sup>+</sup> neurons in the preBötC. (A) Bilateral expression of fluorescent Dbx1<sup>+</sup> neurons from *Dbx1<sup>CreERT2</sup>;Rosa26<sup>tdTomato</sup>* mice by epifluorescence imaging. (B) Whole-cell recording (upper trace, scale bar shows 40 mV) with XII motor output (lower trace, scale bar shows 5 s). (C<sub>1-2</sub>) Planar images show preBötC neurons expressing tdTomato (red) from all focal planes (0-70 μm) on both sides of the preBötC. (D<sub>1-2</sub>) Mask of targets showing software detected Dbx1<sup>+</sup> neurons. (E<sub>1-2</sub>) 3D reconstruction of detected targets for all focal planes, where each Dbx1<sup>+</sup> neuron is represented by a single point at the soma.

randomly selected from the 3D volume of the target pool (Fig. 3.1E<sub>1-2</sub>), with 800-nm pulses at maximum intensity until each target was vaporized, or the ablation procedure was aborted after being deemed a failed lesion (see Chapter 1 Methods, Fig. 1.9).

We measured XII burst amplitude, cycle period, and computed the regularity score (see Chapter 2 Methods for  $R_n$  calculations) using Chart software (ADInstruments, Colorado Springs, CO) and custom Python scripts. We define the *pre-lesion epoch* (i.e., control epoch) as 30 minutes of continuous recording from the

end of the detection phase to the beginning of the ablation phase and *post-lesion epoch* as 30 minutes of continuous recording after the final target ablation. Measurements were compared for un-lesioned versus lesioned conditions or pre- and post-lesion conditions. Each data set was tested for normality using a Shapiro-Wilk test. We rejected the null hypothesis that the data were drawn from a normal distribution if the p-value was less than alpha 0.05. Data that could be considered normally distributed were compared using two-tailed unpaired t-tests, whereas data that did not conform to the normal distribution were compared using non-directional (two-tailed) Mann-Whitney *U*-tests. XII burst amplitude and cycle period are reported in the Results section with standard error (i.e., mean  $\pm$  SEM). Discrete cell counts (pertaining to the number of cells detected or the number of cells lesioned) are reported according to the mean and standard deviation (i.e., mean  $\pm$  SD) because the SD conveys a more accurate sense of the range of cell counts.

### **3.3. Results**

As stated previously in Chapter 2, both slice cutting strategies preserve the sufficient medullary circuits in the preparation for generating respiratory rhythms *in vitro*. Therefore, no distinct difference in network functionality can be gleaned from the features of XII motor output. However, VRC-surface slices are prepared to expose respiratory neurons rostral to the preBötC region, which are typically not associated with inspiratory rhythmogenesis. In contrast, inspiratory rhythmogenic interneurons can be detected directly at the rostral face of preBötC-surface slices (Fig. 3.2A). Thus, we hypothesized that serial deletion of Dbx1<sup>+</sup> neurons in VRC-surface slices would not disrupt inspiratory rhythm generation, whereas even less Dbx1<sup>+</sup> neuron destruction in the ventral medulla of preBötC-surface slices could impede the normal rhythmogenesis *in vitro*.

### ***Deleting Dbx1<sup>+</sup> neurons from the ventral respiratory column***

On average, we detected and ablated  $746 \pm 223$  Dbx1<sup>+</sup> neurons in VRC-surface slices ( $n=4$ , Fig. 3.2B). The amplitude of the XII motor output always measured  $\geq 50\%$  of its control during the ablation phase. On average, the XII output measured  $78 \pm 11\%$  at the end of the ablation phase (Fig. 3.3A) and maintained  $71 \pm 11\%$  of control amplitude during the post-lesion epoch. Respiratory cycle period did not change significantly during the ablation phase (Fig. 3.3B) or during the post-lesion epoch; cycle period measured  $3.9 \pm 0.3$  s during the pre-lesion epoch and  $4.1 \pm 0.4$  s during the post-lesion epoch ( $p=0.8$ , t-test). Furthermore, the CV of pre-lesion periods ( $0.37 \pm 0.07$ ) was not significantly different from the post-lesion CV ( $0.38 \pm 0.08$ ) ( $p=0.9$ , t-test). The regularity score ( $R_n$ ), which measures fluctuations in cycle period, settled at  $\sim 1$  during the ablation phase (Fig. 3.3C), which implies nominally perfect regularity. These data show that cumulative ablation of a mass of Dbx1<sup>+</sup> neurons outside of the preBötC does not perturb or stop respiratory CPG, although the amplitude of XII motor output declines 20-30% on average.

### ***Deleting Dbx1<sup>+</sup> neurons in preBötC***

The outcome was significantly different in preBötC-surface slices ( $n=5$ , Fig. 3.2C) when ablating Dbx1<sup>+</sup> neurons in the preBötC. Cumulative destruction inside of the preBötC decreased the amplitude of XII output as well as respiratory frequency (Figs. 3.2C, 3.3A-B), and ultimately stopped the rhythm (Fig. 3.2C). During the ablation phase in preBötC-surface slices, the amplitude of XII motor output declined  $0.9 \pm 0.3\%$  per neuron deleted, whereas in VRC-surface slices it declined  $0.03 \pm 0.01\%$  per neuron deleted ( $p=0.02$ , Mann-Whitney *U*-test). The amplitude of XII motor output of preBötC-surface slices declined to  $42 \pm 9\%$  of control during the ablation phase, which was significantly greater than the XII decline measured similarly during



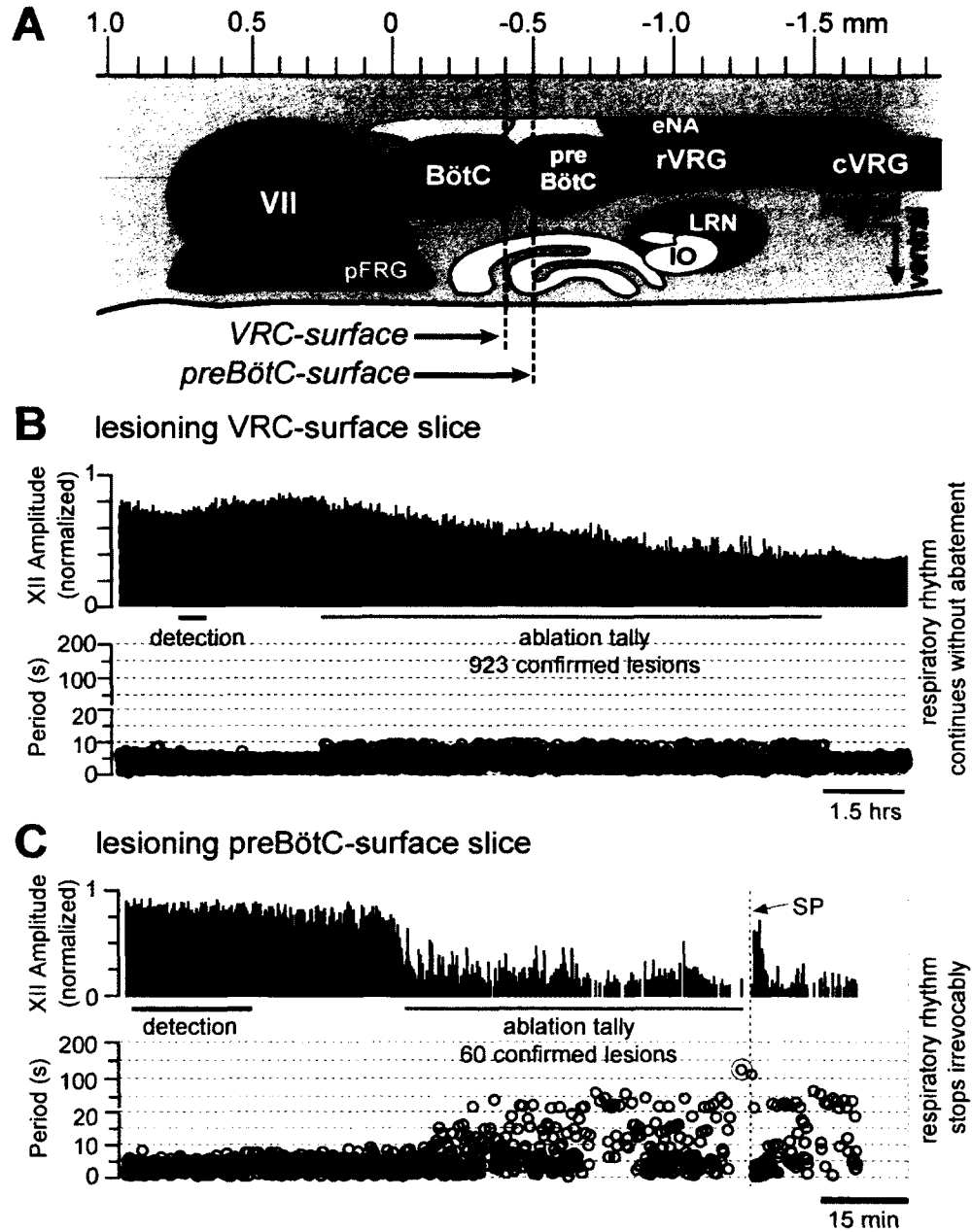


**Figure 3.2** Cumulative deletion of Dbx1<sup>+</sup> neurons. **(A)** Anatomy of slices that retain the preBötC. Para-sagittal view shows nuclei that comprise the VRC (see details in Fig. 2.1). The axis (top) is reproduced from brainstem atlas for newborn mice; preBötC-surface and VRC-surface slices are shown with reference images. **(B-C)** The x-axis is a timeline. The y-axis plots XII amplitude (normalized units, upper) and respiratory cycle period (lower). The respiratory period axis is continuous (0-200 s) but plotted with two scales. Major ticks are separated by 10 s from 0-20 s, and thereafter major ticks are plotted in 100 s divisions from 21-200 s. Period axes plot a data point for every instantaneous period measured. The recording in C stops after 5 min of XII quiescence. **(B)** Ablating Dbx1<sup>+</sup> neurons in a VRC-surface slice preparation. **(C)** Ablating Dbx1<sup>+</sup> neurons in a preBötC-surface slice preparation with SP injection (right red triangle).

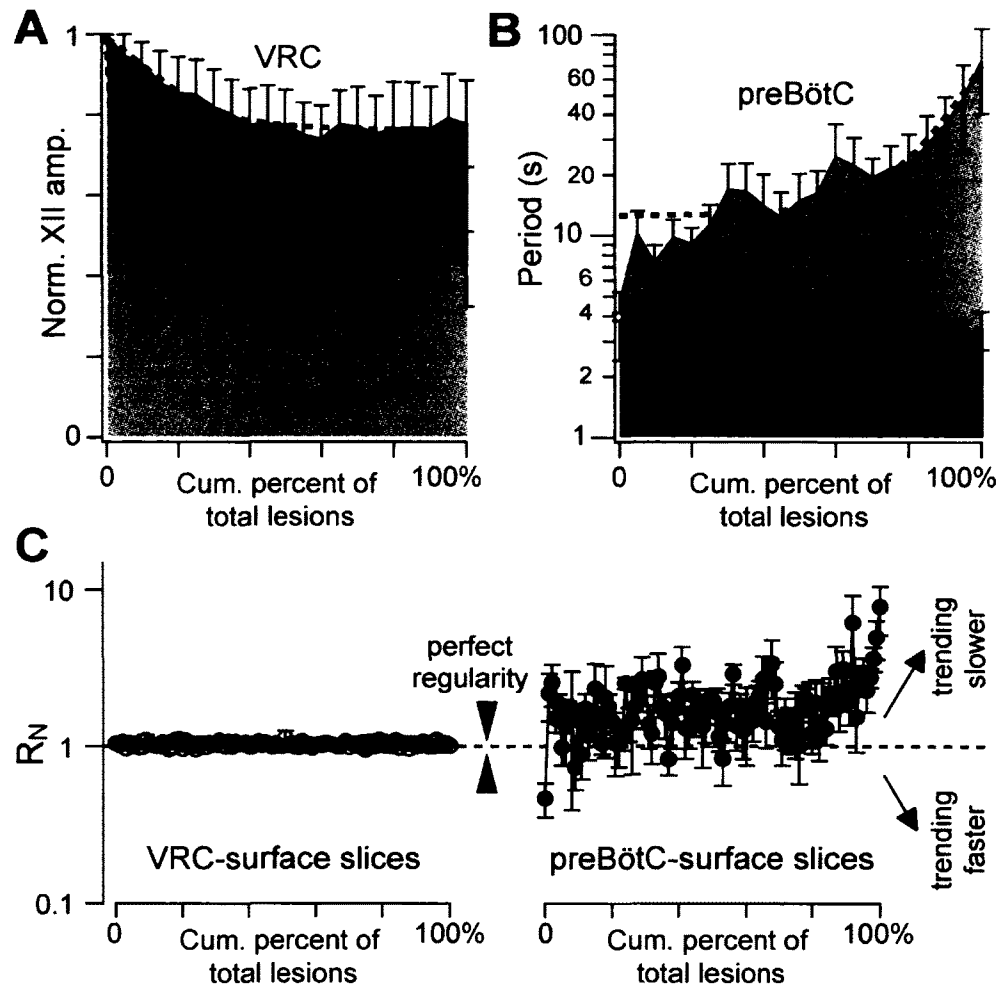


**Figure 3.3** Ablation effects on respiratory rhythm and XII amplitude. (A-B) Measurements are displayed in light grey for preBötC-surface slices and dark grey for VRC-surface slices. (A) XII amplitude vs. cumulative percent of total lesions. (B) Cycle periods vs. cumulative percent of total lesions. A dashed exponential function is fit to the cycle period data for preBötC-surface slices. (C)  $R_n$  vs. cumulative percent of total lesions.  $R_n$  binned in 1% increments for lesioned VRC-surface slices (left,  $n=4$ ) and lesioned preBötC-surface slices (right,  $n=5$ ). Values approaching one are increasing in regularity whereas values greater than or less than unity are becoming more irregular.

lesioning in VRC-surface slices ( $p=0.03$ , Mann-Whitney  $U$ -test, **Fig. 3.3A**).

The cycle period increased during the course of lesioning (**Figs. 3.2C,3.3B**). We force-terminated the ablation procedure when cycle period reached 120 s, since our prior study (**Chapter 2**) indicated that a cycle period of 120 s was a bellwether of a dying preBötC network (**Fig. 2.6A**). By arresting the ablations at the stage of first

detection of a 120-s cycle period, we could attempt a rescue of network function with SP before the preBötC completely perished (Hayes et al. 2012). Consequently, we could not compare rhythmic activity post-lesion to its pre-lesion control state in preBötC-surface slices from *Dbx1<sup>+/CreERT2</sup>;Rosa26<sup>tdTomato</sup>* and *Dbx1<sup>+/CreERT2</sup>;Rosa26<sup>EYFP</sup>* mouse pups. We compare measurements in the pre-lesion state to rhythmic activity during the ablation phase instead. The period continuously increased during the ablation phase with augmentation to  $74\pm 33$  s measured at the end of the lesioning, which compared to  $4.3\pm 0.6$  s pre-lesion, was statistically significant ( $p=0.02$ , Mann-Whitney *U*-test, Fig. 3.3B). The average CV for cycle period changed significantly as well from  $0.36\pm 0.03$  pre-lesion to  $0.7\pm 0.04$  during ablation ( $p=0.009$ , Mann-Whitney *U*-test). Unlike VRC-surface slices that maintained stable regularity ( $R_n\sim 1$ ) during the entire ablation phase, preBötC-surface slices showed an exponential increase in period with large cycle-to-cycle fluctuations that are reflected in  $R_n$  measurements in the range of 1-15 during lesioning (Fig. 3.3C).

On average, the confirmed deletion of  $85\pm 45$  *Dbx1<sup>+</sup>* neurons (mean  $\pm$  SD) in the preBötC ultimately resulted in rhythm cessation. We continued to monitor XII activity to confirm that rhythm never recovered spontaneously within a 2-3 hour range ( $n=5$ ).

#### ***Attempted rescue: erratic evoked rhythms in preBötC-surface slices***

The results shown in Figs. 3.2 and 3.3 suggest that cumulative deletion of a small fraction of *Dbx1<sup>+</sup>* neurons in preBötC-surface slices had a destructive effect on the respiratory CPG and degraded its rhythmogenic capabilities. In order to test whether the remaining un-lesioned neurons in the CPG would be able to support functionality, we stimulated the residual rhythmogenic core of the preBötC, which is marked by NK1R expression (Gray et al. 2010; Wang et al. 2001; Guyenet & Wang 2001;

Stornetta et al. 2003; Pagliardini et al. 2005; Hayes & Del Negro 2007), before the rhythmic function was completely broken down by ablation. As shown previously in **Chapter 2**, we injected a bolus of SP into the preBötC immediately after the respiratory cycle period exceeded 120 s, which was determined empirically as a

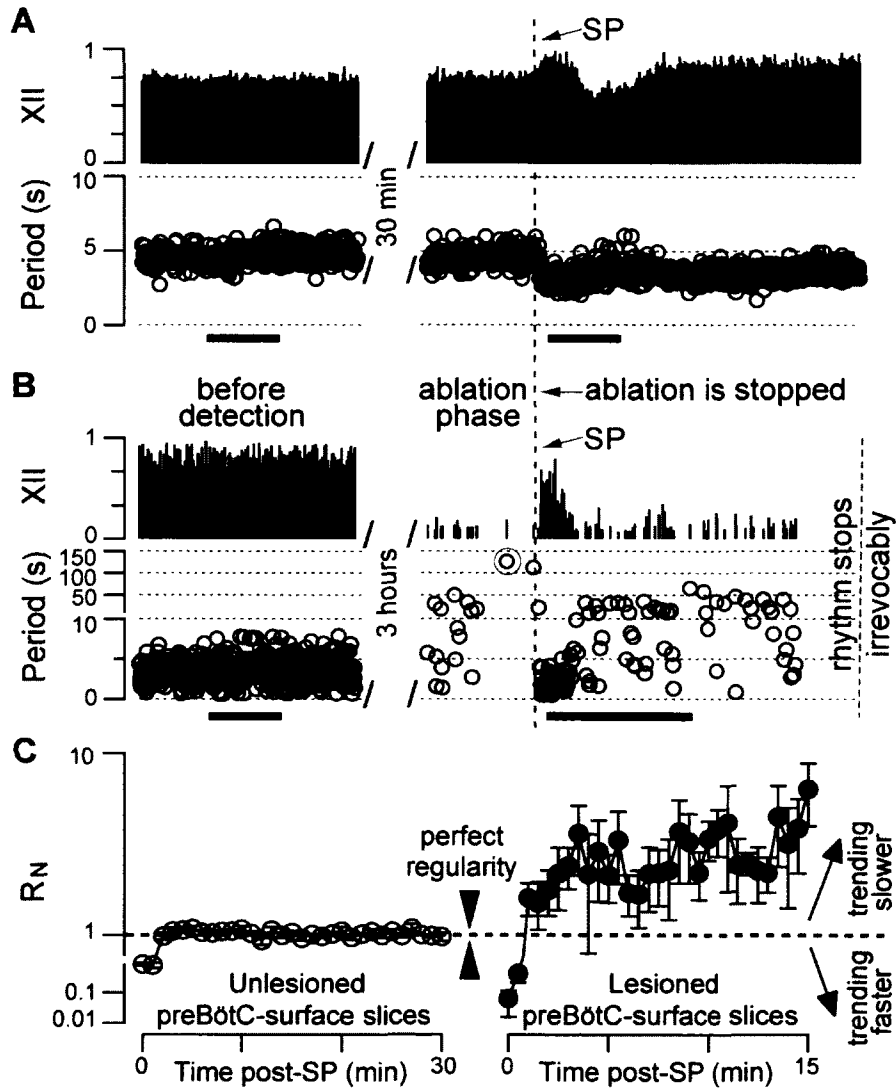


**Figure 3.4** SP injections in preBötC-surface slices. **(A)** Un-lesioned preBötC-surface slice injected with a bolus of SP. **(B)** Lesioned preBötC-surface slice shown before detection phase (left) and 3 hours later during the ablation phase (right). **(C)**  $R_N$  binned in 1 min increments for un-lesioned preBötC-surface slices (left,  $n=4$ ) and 0.5 min increments for lesioned preBötC-surface slices (right,  $n=4$ ) following SP injection at  $t=0$  (red dotted line). Values approaching one are increasing in regularity whereas values greater than or less than unity are becoming more irregular. All scale bars show 10 min.

reliable benchmark for a preBötC network headed inexorably toward rhythm cessation (Hayes et al. 2012).

In four un-lesioned control slices with a mean cycle of  $4.7 \pm 0.1$  s, bolus injection of 1 mM SP transiently lowered the cycle period to  $3.2 \pm 0.1$  s (mean  $\pm$  SEM,  $n=4$ , computed for 40 cycles), which remained below 5 s for  $21 \pm 2$  min. Interesting – and in contrast to slices from WT mice (Chapter 2) – the transient injection of SP ultimately caused a shift in the cycle period to  $3.3 \pm 0.1$  s, which persisted (Fig. 3.4A), and was significantly accelerated compared to control ( $p=0.049$ , Mann-Whitney  $U$ -test). These data suggest that transient exposure to SP can cause a steplike increase in the excitability of the rhythmogenic network, which makes it a useful stimulus to try and revive a preBötC subject to laser ablation protocols (e.g., Fig. 3.2C).

In four lesioned slices, bolus SP injection revived rhythmic respiratory activity transiently. The average cycle period was  $1.7 \pm 0.2$  s (mean  $\pm$  SEM, computed for 40 cycles), which remained below 5 s for  $3 \pm 1$  min (Fig. 3.4B). We compared the duration that cycle periods remained less than 5 s for lesioned slices with un-lesioned slices. The SP effect was significantly shorter in lesioned preBötC-surface slices ( $p=0.02$ , Mann-Whitney  $U$ -test). Furthermore, lesioned slices did not sustain rhythmic output indefinitely after the effects of the SP injection subsided, whereas un-lesioned controls maintained stable rhythmicity for 3-5 hours. More importantly, the SP-evoked rhythmic activity was erratic and slowed down cycle by cycle, whereas un-lesioned controls maintained nearly perfect regularity scores post-SP injection (Fig. 3.4C). These data suggest that for a subpopulation of Dbx1<sup>+</sup> preBötC neurons that express NK1R, if suitably modulated, the remaining un-lesioned class of neurons is still able to generate transient irregular cycles when the network is

severely damaged by ablation, but the remaining core of Dbx1<sup>+</sup> and NK1R<sup>+</sup> neurons in the preBötC is incapable of sustaining regular rhythmogenesis.

### 3.4. Discussion

Here we show that destroying a small fraction of Dbx1<sup>+</sup> interneurons in preBötC leads irreversibly to rhythm cessation. In both slice geometries, the amplitude of XII motor output decreased as a function of lesion tally. Consistent with our prior study that ablated preBötC neurons in WT mice detected by Ca<sup>2+</sup> imaging (Chapter 2), the XII amplitude decreased significantly more in preBötC-surface slices ( $p=0.03$ , Mann-Whitney *U*-test, Fig. 3.3A). Moreover, an abrupt drop in the XII amplitude occurred during the first 10% of lesion tally (amplitude quickly declined to  $52\pm 12\%$  as the first  $8.5\pm 4.5$  neurons deleted) in preBötC-surface slices, whereas amplitude degradation in VRC-surface slices was gradual and slow. These data suggest that Dbx1<sup>+</sup> neurons comprise the normal rhythm generator in preBötC as well as circuits that influence motor output. These Dbx1<sup>+</sup> circuits are extremely sensitive to ablation, and removing as few as <10 Dbx1<sup>+</sup> neurons can immediately cause significant, deleterious effects measurable at the system level in the integrated XII's burst amplitude. A parallel study carried out in our lab recently showed that Dbx1<sup>+</sup> neurons have smooth unbranched dendrites that are largely confined to the transverse plane, and do not extend the dendritic arbor in the rostral-caudal axis (Picardo 2012). These anatomical data suggest that Dbx1<sup>+</sup> neurons facilitate local synaptic integration (most likely receiving synaptic input from other Dbx1<sup>+</sup> neurons) and maintain strong magnitude of synaptic input (Rall & Agon-Snir 1998). The local projections of Dbx1<sup>+</sup> neurons also include the downstream integration of projecting Dbx1<sup>+</sup> premotor neurons (Koizumi et al. 2008). In this study, we report that XII motor output declined  $0.9\pm 0.3\%$  per neuron deleted during the entire lesioning procedure and  $6.5\pm 2.4\%$

during the first 10% of lesion tally. These numbers provide new evidence that individual neuron deletions could have a direct effect on the final common path because of synaptic divergence. If one ablated rhythmogenic Dbx1<sup>+</sup> neuron has several postsynaptic partners that are premotor neurons, and each of these premotor neurons project to one XII motoneurons, then the loss of the original rhythmogenic cell by laser ablation could conceivably reduce the respiratory drive to the XII motor nucleus in measurable ways. Each laser ablation will also diminish the synaptic drive to other rhythmogenic Dbx1<sup>+</sup> neurons in the preBötC, which could diminish synaptic drive and XII motor output all the more. But why is the first 10% of lesioned neurons cause the major decline in XII amplitude? It could be due to the diffusion of excitatory residues (e.g. ATP) released during ablation. After a few deletions of the Dbx1<sup>+</sup> neurons, excitatory residues were accumulated and started revealing effect on the remaining inspiratory network. Purinergic excitation might be activated in the preBötC involving neuron-glia interaction, which would in turn influence local network excitation (Lorier et al. 2007; Lorier et al. 2008; Huxtable et al. 2010). The excitation due to glial release of ATP may therefore compensate the lesion effects caused by laser ablation somewhat during the rest of lesioning procedure.

The present results show that destruction of  $85\pm 45$  Dbx1<sup>+</sup> neurons in preBötC stops the spontaneous respiratory rhythm irrevocably *in vitro*. Compared with the prior study (Chapter 2), where we concluded that deleting  $60\pm 23$  glutamatergic neurons would stop the respiratory rhythmogenesis *in vitro*, the current number is a bit higher than predicted. Why do more Dbx1<sup>+</sup> neurons have to be deleted to preclude the motor function? One reason could be that we detected Dbx1<sup>+</sup> premotor neurons in preBötC region. Previous studies have shown that Dbx1<sup>+</sup> neurons can be found in a continuous line from the dorsomedial to ventrolateral region of the transverse section (Bouvier et al., 2010; Gray et al., 2010; Fig. 3.1A),

many Dbx1<sup>+</sup> neurons lie within the intermediate region between the preBötC and the XII nucleus, which is known to contain respiratory premotor neurons (Koizumi et al. 2008; Volgin et al. 2008). Although inspiratory premotor neurons are spatially segregated from preBötC rhythm-generating neurons, there is still a little spatial overlap between these two populations, i.e., approximately 7% of the premotor neurons were found within preBötC (Koizumi et al. 2008). Furthermore, our group found recently that Dbx1<sup>+</sup> neurons in the preBötC could be differentiated into two subtypes in terms of basic membrane properties (Picardo 2012). Type-1 Dbx1<sup>+</sup> neurons were identified as rhythm-generating candidates, whereas non-rhythmogenic type-2 Dbx1<sup>+</sup> neurons were proposed to activate downstream from Dbx1<sup>+</sup> rhythmogenic neurons, and may play a premotor role in respiratory network activity (Picardo 2012). These data from cellular level analyses of Dbx1<sup>+</sup> neurons and their membrane properties provide a reasonable explanation for the difference between the predicted number and the actual number of Dbx1 lesions that were needed to stop rhythmogenesis in the present set of experiments. In that regard we consider the two numbers (60 vs. 85) to be consistent and thus continuing to support our prior conclusion: destroying 18% of the preBötC core stopped the respiratory rhythm *in vitro*.

One distinct difference between the two types of lesion experiments shown respectively in **Chapter 2** and **Chapter 3** is that in present study, respiratory network motor output degraded in a relatively faster rate with the benchmark of rhythm cessation (cycle period > 120 s) occurred during the ablation procedure, whereas in prior study (**Chapter 2**) the delayed benchmark in cycle period typically arose after a ~30-min rundown of the motor output post-lesion. The immediate lesion effects due to the deletion of Dbx1<sup>+</sup> neurons demonstrate that Dbx1-expressing interneurons comprise the respiratory rhythm-generating core and removal of a relatively small



fraction of this glutamatergic core cause direct deleterious effect on network output, and will ultimately result in rhythm cessation *in vitro* on a short-time scale.

Similarly, bolus injection of SP elicited a transient and irregular sequence of XII bursts in lesioned preBötC-surface slices and thereafter the network activity fell irreversibly silent (Fig. 3.4B). The present study shows stronger post-SP effects on both un-lesioned and lesioned preBötC-surface slices (Fig. 3.4A-B) compared with the previous results (Chapter 2, Fig. 2.6), these data suggest different membrane properties of preBötC rhythmogenic interneurons in terms of responding to SP stimuli between different animal models. Furthermore, since the lesioned slices were still able to generate transient respiratory rhythms in response to SP application, interconnections among Dbx1<sup>+</sup> core preBötC interneurons must remain to some extent. Consequently, in general agreement with the numerical conclusions (Chapter 2 Discussion), the present study tested the hypothesis that ataxic breathing, even respiratory failure can be induced by destruction of a small fraction of Dbx1<sup>+</sup> inspiratory neurons in the preBötC. We conclude that cumulative laser ablation of the core population of the respiratory CPG can result in a critical threshold to be crossed during lesioning, after which rhythmogenesis cannot be sustained *in vitro*.

Neurodegenerative diseases often present respiratory pathologies ranging from sleep-disordered breathing to respiratory failure (Maria et al. 2003; Benarroch et al. 2007; Ferguson et al. 1996; Punjabi et al. 2009). The loss of brainstem neurons that express neuroanatomical characteristics consistent with the preBötC have been associated with such pathologies (McKay et al. 2005; Benarroch 2003; Benarroch et al. 2003). We determined that the loss of a critical mass of the preBötC core can stop spontaneous rhythms without completely destroying the underlying network. These results suggest that neurodegenerative disorders may manifest abnormal respiratory

behavior, and potentially respiratory failure, even when relatively small fractions of the respiratory networks that include the preBötC are destroyed during disease progression. The model we present could be used to simulate disease etiology by progressively lesioning a network so that it approaches the tipping point from a nominally functional system to one that can no longer spontaneously function without intervention. The network, thus lesioned *in vitro*, could be used to develop and evaluate prevention and treatment strategies that bolster respiratory function.

### 3.5. References

**Bargmann C, Avery L (1995)** Laser killing of cells in *Caenorhabditis elegans*. In: *Caenorhabditis elegans: modern biological analysis of an organism*, vol. 48 (Epstein, H. and Shakes, D., eds), pp 225-250 Amsterdam: Elsevier.

**Benarroch EE (2003)** Brainstem in multiple system atrophy: clinicopathological correlations. *Cell Mol Neurobiol* 23:519-526.

**Benarroch EE (2007)** Brainstem respiratory control: substrates of respiratory failure of multiple system atrophy. *Mov Disord* 22:155-161.

**Benarroch EE, Schmeichel AM, Low PA, Parisi JE (2003)** Depletion of ventromedullary NK-1 receptor-immunoreactive neurons in multiple system atrophy. *Brain* 126:2183-2190.

**Bouvier J, Thoby-Brisson M, Renier N, Dubreuil V, Ericson J, Champagnat J, Pierani A, Chedotal A, Fortin G (2010)** Hindbrain interneurons and axon guidance signaling critical for breathing. *Nat Neurosci* 13:1066-1074.

**Ferguson KA, Strong MJ, Ahmad D, George CF (1996)** Sleep-disordered breathing in amyotrophic lateral sclerosis. *Chest* 110:664-669.

**Gray PA, Hayes JA, Ling GY, Llona I, Tupal S, Picardo MC, Ross SE, Hirata T, Corbin JG, Eugenin J, Del Negro CA (2010)** Developmental origin of preBötzinger complex respiratory neurons. *J Neurosci* 30:14883-14895.

**Gray PA, Janczewski WA, Mellen N, McCrimmon DR, Feldman JL (2001)** Normal breathing requires preBötzinger complex neurokinin-1 receptor-expressing neurons. *Nat Neurosci* 4:927-930.

**Gray PA, Rekling JC, Bocchiario CM, Feldman JL (1999)** Modulation of respiratory frequency by peptidergic input to rhythmogenic neurons in the preBötzinger complex. *Science* 286:1566-1568.

**Hayes JA, Wang X, Del Negro CA (2012)** Cumulative lesioning of respiratory interneurons disrupts and precludes motor rhythms in vitro. *Proc Natl Acad Sci U S A* 109:8286-8291.

**Huxtable AG, Zwicker JD, Alvares TS, Ruangkittisakul A, Fang X, Hahn LB, Posse de Chaves E, Baker GB, Ballanyi K, Funk GD (2010)** Glia contribute to the purinergic modulation of inspiratory rhythm-generating networks. *J Neurosci* 30:3947-3958.

**Koizumi H, Wilson CG, Wong S, Yamanishi T, Koshiya N, Smith JC (2008)** Functional imaging, spatial reconstruction, and biophysical analysis of a respiratory motor circuit isolated in vitro. *J Neurosci* 28:2353-2365.

**Lorier AR, Huxtable AG, Robinson DM, Lipski J, Housley GD, Funk GD (2007)** P2Y1 receptor modulation of the pre-Bötzinger complex inspiratory rhythm generating network in vitro. *J Neurosci* 27:993-1005.

**Lorier AR, Lipski J, Housley GD, Greer JJ, Funk GD (2008)** ATP sensitivity of preBötzinger complex neurones in neonatal rat in vitro: mechanism underlying a P2 receptor-mediated increase in inspiratory frequency. *J Physiol* 586:1429-1446.

**Maria B, Sophia S, Michalis M, Charalampos L, Andreas P, John ME, Nikolaos SM (2003)** Sleep breathing disorders in patients with idiopathic Parkinson's disease. *Respir Med* 97:1151-1157.

**McKay LC, Janczewski WA, Feldman JL (2005)** Sleep-disordered breathing after targeted ablation of preBötzinger complex neurons. *Nat Neurosci* 8:1142-1144.

**Picardo MC (2012)** Physiological and Morphological Characterization of Genetically Defined Classes of Interneurons in Respiratory Rhythm and Pattern Generation in Neonatal Mice. *Dissertation*.

**Punjabi NM, Caffo BS, Goodwin JL, Gottlieb DJ, Newman AB, O'Connor GT, Rapoport DM, Redline S, Resnick HE, Robbins JA, Shahar E, Unruh ML, Samet JM (2009)** Sleep-disordered breathing and mortality: a prospective cohort study. *PLoS Med* 6:e1000132.

**Rall W, Agon-Snir H (1998)** Cable Theory for Dendritic Neurons. In: *Methods in neuronal modeling : from ions to networks*, 2nd Edition (Koch C, Segev I, eds), pp 27-92. Cambridge, Mass.: MIT Press.

**Tan W, Janczewski WA, Yang P, Shao XM, Callaway EM, Feldman JL (2008)** Silencing preBötzinger complex somatostatin-expressing neurons induces persistent apnea in awake rat. *Nat Neurosci* 11:538-540.

**Volgin DV, Rukhadze I, Kubin L (2008)** Hypoglossal premotor neurons of the intermediate medullary reticular region express cholinergic markers. *J Appl Physiol* 105:1576-1584.

**Wallen-Mackenzie A, Gezelius H, Thoby-Brisson M, Nygard A, Enjin A, Fujiyama F, Fortin G, Kullander K (2006)** Vesicular glutamate transporter 2 is required for central respiratory rhythm generation but not for locomotor central pattern generation. *J Neurosci* 26:12294-12307.

## CONCLUSIONS

The work presented in this dissertation has advanced our understanding of how graded neuronal destruction perturbs the function of the respiratory CPG in the preBötC of the ventral medulla, and how serial ablations in the preBötC may disrupt the robustness of the network activities, and ultimately impede the respiratory rhythmic function *in vitro*.

We developed an automated system for identifying neurons within tissue slices and then individually laser-ablating these neuron targets on the basis of the expression of genotypic fluorescent protein markers or Ca<sup>2+</sup> imaging. We applied this system to the mammalian respiratory CPG to test these predictions: 1) Serial ablation of functionally or genetically defined inspiratory neurons perturbs the frequency of respiratory rhythm and causes periodic irregularity; 2) The preBötC can sustain rudimentary rhythm-generating function even with serial ablations that cause profound cell loss; And 3) extensive ablations abolish respiratory rhythm generation.

In Ca<sup>2+</sup>-imaging experiments, we identified rhythmically active inspiratory neurons in the preBötC based on imaged Ca<sup>2+</sup> fluorescent change. Our data show that selectively and cumulatively deleting rhythmic neurons in the preBötC progressively decreases respiratory frequency and the amplitude of XII motor output. On average, the deletion of 120±45 neurons stopped spontaneous respiratory rhythm, and our data suggest ~82% of the rhythm generating neurons remain unlesioned. Cumulative ablations in other medullary respiratory regions did not affect frequency, but diminished the amplitude of motor output to a lesser degree. These data suggest that cumulative single-cell ablations caused a critical threshold to be

crossed during lesioning, after which rhythm generation in the respiratory network was unsustainable. Moreover, when the lesioning of targets was sufficient for a cessation of coherent rhythmic activity, we also tested whether any rhythmic activity could be revived by applying an agonist of network excitability (SP) shortly after the ablation phase terminated. The stimuli did transiently revive the rhythm but failed to sustain it, which suggest that the lesion procedure did not destroy the network function *per se*, but destroyed enough of the network to preclude sustainable and stable rhythmic function *in vitro*.

A more specific prediction has been discussed in **Chapter 2** where we concluded that deleting  $60 \pm 23$  glutamatergic neurons (mean  $\pm$  SD) stopped respiratory rhythmogenesis *in vitro*. We tested this numerical conclusion by performing laser ablation studies on genetically identified populations with a known transmitter phenotype. We used genetic reporter mice to target known glutamatergic Dbx1-derived neurons in the preBötC (Gray et al. 2010; Bouvier et al. 2010). Here we showed that progressive destruction of Dbx1<sup>+</sup> neurons in preBötC reveals similar deleterious effects on network function as shown previously in **Chapter 2** - decreases in respiratory frequency and the amplitude of motor output. Moreover, our data suggest that the deletion of  $85 \pm 45$  Dbx1<sup>+</sup> neurons in preBötC causes severe and irreversible damage to the rhythm-generating core and leads to ultimate rhythm cessation *in vitro*.

We have discussed in **Chapter 3** for why we empirically think the numerical conclusions from two different types of experiments are correlated in terms of the possibly involved premotor functions in preBötC. Furthermore, we assessed the severely damaged respiratory CPG by injecting SP to rescue the rhythm when a benchmark cessation in rhythm cycle periods occurred during the ablation, the

stimuli effected an immediate and strong restoration in respiratory rhythm, but the recovery was transient, and failed to sustain rhythmic function in the preBötC, as shown before in Ca<sup>2+</sup> imaging experiments (Chapter 2).

The consistency in experimental results between ablation of rhythmically active inspiratory neurons and deletion of Dbx1<sup>+</sup> neurons in the preBötC demonstrates that when cumulative laser ablation destroys a critical mass of the core of respiratory CPG, the lesioning procedure will cause rhythm cessations, and ultimately failures, in respiratory rhythmogenesis *in vitro*. These data could provide an estimate of the number of critical rhythmogenic neurons in the preBötC that are necessary for normal inspiratory activity. However, the highly reduced nature of the slice preparation, and the shifts in slice geometry that are needed to expose the preBötC surface for imaging and ablation, as well as the lack of neuromodulatory inputs in thin slices (Garcia et al. 2011; Doi & Ramirez 2008; Doi & Ramirez 2010; Pena & Ramirez 2002), undoubtedly exert a strong – and as yet incompletely understood – effect on the absolute number of rhythmogenic neurons that are needed to sustain core functionality in the respiratory CPG.

The automated neuronal lesioning tool we developed will potentially help us quantify how many constitute cells are necessary for maintaining behaviors, respiration being the first application. In the preBötC, this still requires further investigations to refine the current numerical conclusions, but we believe this 'seek-and-destroy' cell-specific laser detection and ablation technique may be of great value for studying similar rhythmic behaviors *in vitro*, such as locomotor pattern generators in the spinal cord or masticatory networks of the hindbrain, as well as other CPGs throughout the central nervous system.



## References

**Bouvier J, Thoby-Brisson M, Renier N, Dubreuil V, Ericson J, Champagnat J, Pierani A, Chedotal A, Fortin G (2010)** Hindbrain interneurons and axon guidance signaling critical for breathing. *Nat Neurosci* 13:1066-1074.

**Gray PA, Hayes JA, Ling GY, Llona I, Tupal S, Picardo MC, Ross SE, Hirata T, Corbin JG, Eugenin J, Del Negro CA (2010)** Developmental origin of preBötzinger complex respiratory neurons. *The Journal of Neuroscience* : the official journal of the Society for Neuroscience 30:14883-14895.

**Garcia, A. J., 3rd, Zanella, S., Koch, H., Doi, A. & Ramirez, J. M.** Chapter 3-- networks within networks: the neuronal control of breathing. *Progress in brain research* 188, 31-50 (2011).

**Doi, A. & Ramirez, J. M.** Neuromodulation and the orchestration of the respiratory rhythm. *Respiratory Physiology & Neurobiology* 164, 96-104 (2008).

**Doi, A. & Ramirez, J. M.** State-dependent interactions between excitatory neuromodulators in the neuronal control of breathing. *J Neurosci* 30, 8251-8262 (2010).

**Pena, F. & Ramirez, J. M.** Endogenous activation of serotonin-2A receptors is required for respiratory rhythm generation in vitro. *The Journal of Neuroscience* : the official journal of the Society for Neuroscience 22, 11055-11064 (2002).

# APPENDIX

## **Ablator-0.8.4:**

This appendix describes the main structure of the Ablator package, and gives brief descriptions of major scripts and modules. Underlined text is used to describe the function of each setting, and the corresponding environment variables in the code are described in blue text. Folder names are described in **bold underlined** text.

### l) **ablator**

#### 1. **microscopecontrollers**

##### 1.1 LSMControl.py

This script interacts with the LSM microscopy software. It connects to the LSM core - AIM.exe (located in c: \AIM\AIM.exe) to control the LSM software to automatically carry out the experimental procedures, such as initiating the scan control window, controlling the stage and focus, starting the image acquisition window, turning lasers on, changing laser power, controlling scan speed, controlling the pinhole, creating and opening new image data base, saving acquired images, closing window when acquisition finished, setting image resolution, switching configuration for specific settings of mirrors and filters for the light path, and choosing other imaging options. This script moves the cursor in the LSM software GUI and selects certain tab or function buttons within the LSM interface to implement the lesion protocol.

##### 1.2 LSMController.py

This script stores the default settings and pre-determined values for variables such as scanSpeed, laserConfigurationName, laserConfigurationType, and resolution, for

processes including initializing the microscope, creating a new image database for the experiment, moving the Ti:sapphire laser to target locations, acquiring time-series images, acquiring single images, and saving acquired images to the database.

## 2. stage

### 2.1 LabjackPython.py

LabJack U3 is a USB-based measurement and automation device that provides analog as well as digital inputs and outputs. We use the LabJack U3 as an interface between the master computer and the robotic X-Y translation stage system. LabJackPython is the cross-platform module for communicating with the LabJack U3. It is a python wrapper that implements functions from the LabJack driver.

### 2.2 StageConfiguration.py

It reads the X-Y inputs for setting the X-Y stage positions corresponding to the domain of detection and ablation bilaterally, and saves the coordinates.

### 2.3 XYTranslator\_control.py

This script controls the robotic X-Y microscope stage to locate the preBötC, the nucleus containing putative target neurons in the present context, and then

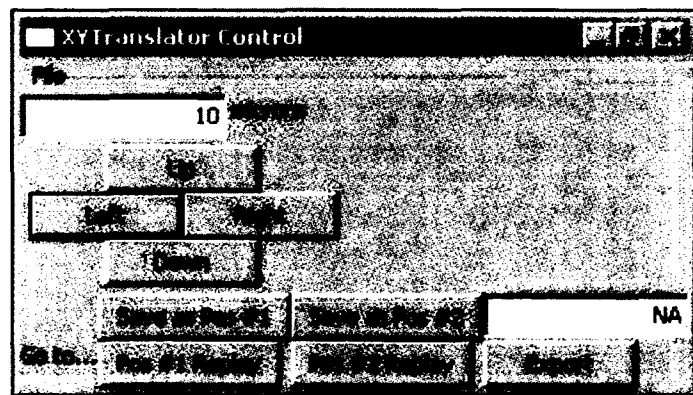


**Figure A.1** Screenshot of the GUI launched by XYTranslator\_Control.py routine.

generates a convenient GUI that is used to specify the preBötC location bilaterally in the transverse plane. Movements are made in unit of  $\mu\text{m}$  (**Fig. A.1**).

- a. Move the specimen such that the preBötC (or other nucleus of interest) is in the center of the field of view. Use GUI to set Position 1.
- b. Move the contralateral preBötC (or other) to center of field of view. Use GUI to set as Position 2.

## 2.4 XYTranslator.py

This script connects to the LabJack driver to control the speed and direction of the actual movements of the X-Y translation stage.

## 3. **targetdetectors**

### 3.1 DynamicTargetDetector\_PrecalculatedTargets.py

It is the standard control program for  $\text{Ca}^{2+}$  imaging. It defines the basic settings for the experiment, such as `generalTrackConfigurationName`, `generalTrackConfigurationType`, `postLesionScanSpeed`, `postLesionTrackConfigurationName`, `lastMovement`, `currentStagePosition`, `zrange` and `stageConfiguration`. It starts the acquisition of time-series images at each focal plane on both sides of the preBötC. Thereafter it calls another program called `DynamicImageAnalyzer.py` (see below) to perform the automatic analyses for all the acquired images, and then it rule out a final list of targets based on the analysis results.

### 3.2 DynamicImageAnalyzer.py

This script is the main program for analyzing the acquired time-series images, as referenced above (see `DynamicTargetDetector_PrecalculatedTargets.py`). There are three steps for getting the final list of the potential targets.

- a. The Frequency domain test evaluates whether a potential target neuron oscillates in the respiratory band 0.15 - 0.5 Hz, see **Chapter 1 Methods** for more details.
- b. The Threshold test evaluates whether the oscillation is of sufficient magnitude using the threshold score (50 by default) to select high score targets. Also see **Chapter 1 Methods** for more information.
- c. The Peak Count Test applies a peak-count threshold of five (i.e., 5/min, set in AblatorConfiguration.py) to count the number of amplitude peaks that cross the pre-determined amplitude threshold in one time-series cycle (1-min in present study). This test is meant to pick targets with sufficient high amplitude oscillations in the appropriate frequency range to arrive at a final array of cell targets. The amplitude threshold is determined by the experimenter beforehand based on a series of tests. This threshold value can be very different among particular experiments resulting from differences of dyes, loading protocols, animal models and imaging settings. The experimenter should perform 'Plot Z-axis Profile' for a number of ROIs in analyzed stack image to assess the signal-to-noise ratio based on the current imaging settings, and then decide a proper threshold to collect the oscillatory peaks while avoiding false positive peaks during the time-series fluorescence oscillatory cycle. Note: If any modification is made to the image processing settings, which are stored in variable thresholdDynamicImage in DynamicImageAnalyzer.py, the experimenter should empirically re-evaluate the amplitude threshold on a case-by-case basis.

### 3.3 StaticTargetDetector\_PrecalculatedTargets.py

This script is the main program for target detection via YFP or td-Tomato fluorescence images. It acquires a static image at the slowest speed (Speed = 1,

Resolution 512 x512) for each focal plane, then calls StaticImageAnalyzer.py to analyze the potential targets.

### 3.4 StaticImageAnalyzer.py

It finds the potential targets based on fluorescence intensity of the cells, wherein local maxima are a primary selection feature. See **Chapter 1 Methods** section for more information.

## 4. targetselectors

### 4.1 BilateralTargetSelector.py

This script implements the default ablation strategy that randomly draws targets from the 3D volume of the detected neurons.

### 4.2 ClosestToCentroidTargetSelector.py

This routine preferentially selects targets for ablation based on proximity to the center of collected targets.

### 4.3 FileLoaderTargetSelector.py

This script loads the target list from a pre-generated file named "potentialTargets.txt" in experiment directory, and then draws targets from the loaded list for random ablation.

### 4.4 StrongestScoreTargetSelector.py

This script preferentially lesions the strongest rhythmically active targets first based on the target scores from the threshold test for the relative peak power in the specified frequency range (described in **Chapter 1 Methods** and DynamicImageAnalyzer.py).

## 5. utils

## 5.1 FileUtils.py

This script creates the main directory and sub directories at start of the experiment. It also collects information pertaining to the lesion protocol from `lesioned_coordinates.txt`, which lists the total number of targets and all the potential target coordinates. This script also saves and the history files that describe the entire experiment, including stage configuration files (`stage.config`, `stage_history.txt`), potential targets file (`potentialTargets.txt`), lesion history file (`lesion_history.txt`), focus history file (`focus.txt`) and experiment log file (`log.txt`).

## 5.2 FrequencyAnalyzer.py

This script is called by `DynamicImageAnalyzer.py` to perform frequency domain analysis. It defines windows and functions for calculating the power spectrum density (PSD) based on Fourier analysis.

## 5.3 RoiDecoder.py

It detects ROIs, decodes the ImageJ ROI binary file format and saves all the ROIs in `.zip` file.

## 5.4 Statistics.py

This script defines all the statistical processes and their application for target detection and image analysis:

5.4.1 `var`: Returns the variance of the values in the passed list using `N` for the denominator (i.e., for estimating population variance).

5.4.2 `cv`: Returns the coefficient of variation on a list of values.

5.4.3 `mean`: Returns the arithmetic mean of the values in the passed list.

5.4.4 `median`: Returns the median of the values in the passed list.

5.4.5 `ss`: Squares each value in the passed list, adds up these squares and returns the result.

5.4.6 `stderr`: Returns the estimated standard error of the mean of the values in the passed list.

## 5.5 TargetUtils.py

This script loads targets from the pre-generated target list file (`lesioned_coordinates.txt` by default); sorts targets based on defined selection protocol (random by default but see above for other strategies); and saves lesioned target in `lesion_history.txt` in experiment directory.

## 6. AblationConfiguration.py

This script establishes initial settings for the experiment. These critical settings for the experiment are described in the narrative below.

6.1 Unilateral vs. bilateral lesions sets environment variable `bilateralLesion = True` for the default, which is a bilateral lesion. This is the default because we assume most applications will be applied in *in vitro* preparations with bilateral symmetry, for example slices in the transverse or frontal planes. However, *in vitro* preparations in the parasagittal plane would probably be lesioned unilaterally.

6.2 Tissue depth for detection and lesion specifies the z-depth of the confocal planes for target selection bilaterally by setting environment variables for both sides: `POSITION_1_ZRANGE = [z1, z2]`, `POSITION_2_ZRANGE = [z3, z4]`, where  $z_i$  indicates confocal plane depth in  $\mu\text{m}$ , as monitored by the scanning microscopy software package, AIM for the LSM 510 system (Zeiss).

6.3 Experiment Identification provides an identification or name that will apply to subdirectories and files created during the experiment by setting the environment



variable `experiment_id = "121210slice1lesion1"`. Here, we use the convention `YYMMDD-slice#lesion#`, in which the name in quotes refers to December 10, 2012, slice 1, lesion set 1.

6.4 Nature of fluorescent labeling specifies whether target detection relies on genetic XFP labeling,  $\text{Ca}^{2+}$  imaging, or another static fluorescent marker. Sets the environment variable `lesionType = "fluo-8" or "YFP" or "tdTomato"` (or a user-generated alternative).

6.5 Target detection method. The environment variable `targetDetectionClass` determines how targets are detected based on different acquisition strategies.

6.5.1 `StaticTargetDetector_PrecalculatedTargets` pertains to `lesionType = YFP` or `tdTomato`.

6.5.2 `DynamicTargetDetector_PrecalculatedTargets` pertains to `lesionType = fluo-8`.

6.6 Ablation strategy. The environment variable `targetSelectionClass` determines how targets are selected for laser ablation.

6.6.1 The default is `"BilateralTargetSelector"` for bilateral random target selection, but the other alternatives (described above) include:

6.6.2 `"ClosestToCentroidTargetSelector"`, which picks targets for ablation based on proximity to center of the volume of detected targets, `"FileLoaderTargetSelector"` where a text file can be used to specify some exact order for lesions, and

6.6.3 `"StrongestScoreTargetSelector"` in which targets can be preferentially selected for ablation based on the magnitude of the fluorescence signal.

6.7 Lesion options. There are several variables for controlling the ablation phase.

6.7.1 `lesionScanSpeed` sets the initial velocity of laser scanning of the zoomed lesion area. The default speed is 5, i.e. 1.95 s/frame.

6.7.2 `lesionZoom` controls the digital zoom to concentrate laser scanning to a very small plane for the purpose of laser lesioning a target. The default is 38, i.e. the lesion area =  $10.58 \times 10.58 \mu\text{m}^2$ .)

6.7.3 `maxLesionTries` specifies the number of attempts for each lesion before moving on to next target. The default is 5. Setting this environment variable prevents the protocol from looping endlessly in attempts to lesion the target.

6.7.4 `switchSidesEveryXLesions` sets number of lesions before switching to alternative side. The default is 100.

6.8 Parameter setting for image processing. These variables specify the values for parameters required in image analysis.

6.8.1 `filterSlowestFrequency` = 0.15. Adjustable by the user, this pertains to the minimum oscillation frequency for dynamic target detection.

6.8.2 `filterFastestFrequency` = 0.5. Adjustable by the user, this pertains to the maximum oscillation frequency for dynamic target detection.

6.8.3 `gaussianBlurRadius` = 0.5. This setting smoothes images to reduce the noise during image processing step in both static and dynamic target detection. It is set to 0.5 by default, which is optimal for neonatal mouse brainstem images, but may be different for different model organisms and/or other regions of the CNS, and could depend on the nature of fluorophores used to visualize cell populations.

6.8.4 `minNeuronSize` = 25 (in  $\mu\text{m}^2$ ). This setting influences the ROI determination in dynamic and static target selection routines.

6.8.5 `maxNeuronSize` = 100 (in  $\mu\text{m}^2$ ). This setting influences the ROI determination in dynamic and static target selection routines.

6.9 Optional management. To manually adjust some variables for a specific single experiment, or try different conditions to re-detect targets:

6.9.1 `skipImageAcquisitions = False`. This is set to false by default, so that the system will acquire, and then analyze images. If it is set to True, the re-running Ablator.py will skip the image acquisition part, and go directly to the analysis phase to re-analyze the pre-acquired images. This latter mode of operation is useful to study the acquisition phase offline after the experiment.

6.9.2 `stopAfterPreprocessing = True`. This is set to True by default, in which case the software is paused after the target acquisition phase, before the start of the ablation phase.

6.9.3 `alwaysRedetectTargets = False`. This is set to False by default. if it is set to True, every time Ablator.py is started, the software looks for previously acquired images in the defined directory and perform the image analysis on the prior data.

6.10 Optional break point. The protocol can be paused after 10 lesions (this number of lesions can be adjusted by user) to allow for modifications of the protocol or the physical instruments by setting `breakAfterTen = True`. Gives the user the prerogative to modify the experiment after 10 lesions without needing to start acquisitions over again.

6.11 Threshold for lesion detection. This setting is not often modified. The value of the environment variable `successfulLesionThreshold` gauges whether a lesion attempt was successful based on brightness of water vapor autofluorescence at the target location. Default is 2000. See **Chapter 1 Methods** for further information about how this operates during lesion confirmation.

## 7. AblatorUtils.py

This routine synchronizes the internal clocks between the master computer and the

electrophysiology monitoring computer. It generates mask images for detected potential targets and converts between pixel and micron coordinates so that the master computer running the LSM software and ImageJ operate in the same coordinates. This script also confirms lesion success; obtains ROI areas, checks ROI “supersets” at each round of iteration, removes redundant ROIs, and then appends the target coordinates list. Finally, this script controls stage alternations, and ensures that targets on both bilateral sides of the target nucleus are fully exhausted. See **Chapter 1 Methods** for further information on how ROIs are determined from the acquired data.

7.1 `synchronizeComputerTimes`: this synchronizes the master computer’s time with the Network Time Protocol (NTP) time server on the electrophysiology recording computer.

7.2 `thresholdAndAnalyzeImageDrift`: this calibrates the analyzed images to get potential target coordinates based on the calibration relationship of micron per pixel.

7.3 `successfullyLesioned`: gets the acquired fluorescent image for a single lesion confirmation, calculates the max gray value of the image and compares it with `successfulLesionThreshold`, which is predetermined in `AblationConfiguration.py`. If the max gray value exceeds the threshold, then the success of the ablation is deemed “True”.

7.4 `removeRedundantRois`: this routine keeps the “supersets” of the ROI and removes previously acquired, smaller ROIs that are contained in the superset ROIs.

7.5 `otherStagePositionHasTargets`: checks if any targets have been left un-lesioned at either bilateral X-Y stage position.

7.6 `switchToAlternateStagePosition`: this switches the stage to alternative positions

during the lesioning based on the value that was preset in switchSidesEveryXLesions in AblationConfiguration.py.

#### 8. ImageJ.py

This script defines all the image processing procedures that are performed in Image J. It sets initial values and appropriate parameters for each of the process as default settings. These settings will be highly user specific depending on animal model, brain or CNS region, cell type of interest, as well as fluorophores employed.

#### 9. Targets.py

This routine defines a class dubbed Target, and then saves a series of information for each single ROI, such as its index number, position number (which side of the preBötC it belongs to), 3D coordinates, and the peak amplitude score assessed by the amplitude threshold test.

#### II) **data**

This directory is the main path for storing all generated data directories.

#### III) **docs**

This fold contains instructions and help documents for Ablator software.

#### IV) **ImageJ**

This is the ImageJ directory that contains all required image processing features and functions for image analyses during the detection and ablation phases. A certain function such as a filter or a statistic measurement is called by other main routines to perform the image transformation in ImageJ environment.

#### V) **tests**

This fold allows the user to save customized testing routines.

VI) **utils**

This is the directory that can store any user defined tools or functions, currently it contains some image analysis programs and statistic tools written by the experimenter for data collation and detailed analyses.

VII) Ablator.py

This is the main control program that calls all required subroutines described above to realize the 3-step experimental protocol (see **Chapter 1 Methods** for more detail).

VIII) lesionSingleTarget.py

This is the control program that allows the software to specifically lesion a single cell based on its 3D coordinate that was entered into the script by user.